

Investigating Faint Light and Diffuse Gas Around Galaxies in Group Environments

by

Tyler James McCabe

A Dissertation Presented in Partial Fulfillment
of the Requirements for the Degree
Doctor of Philosophy

Approved July 2024 by the
Graduate Supervisory Committee:

Sanchayeeta Borthakur, Co-Chair

Rogier Windhorst, Co-Chair

Rolf Jansen

Seth Cohen

Allison Noble

ARIZONA STATE UNIVERSITY

August 2024

©2024 Tyler James McCabe

All Rights Reserved

ABSTRACT

One of the fundamental questions in extragalactic astronomy is understanding how galaxies grow and evolve. The answer to this question is rooted in a galaxy's ability to accrete fresh gas to sustain star formation as well as the environment in which a galaxy is located. In this dissertation, diffuse light in the outskirts of galaxies is investigated using ~ 28 hours of r-band imaging with the Large Binocular Telescope (LBT) of the GOODS-N field. Optimal resolution and optimal depth mosaics were created to investigate the ability for the same dataset to enhance galaxy substructure as well as faint light and tidal tails and interactions. These techniques were applied to ~ 35 hours of U-band LBT imaging of the COSMOS field where an optimal depth mosaic was created and combined with a catalog of galaxy groups to search for intragroup light (IGrL). By using two methods to stack groups and search for IGrL, robust upper limits were measured and compared with other studies providing insight for the origins and buildup of IGrL. Lastly, the intragroup medium (IGrM) was directly traced with the Hubble Space Telescope (HST) using quasar absorption spectroscopy. For a sample of 18 galaxy groups, a patchy, multiphase IGrM was observed with cool and hot ionization states aligned with minimal velocity offsets. While no volume filling component of the IGrM was detected, the impact of the IGrM on group evolution is discussed as well as future ways to study the IGrM.

DEDICATION

To my incredible wife, Tori. You've been my biggest support and I couldn't have done this without you.

ACKNOWLEDGMENTS

I would like to extend my deepest gratitude to everyone who has helped my throughout my time at ASU. To my advisors, Sanchayeeta Borthakur and Rogier Windhorst, thank you for admitting me back in 2018 and taking a chance on my potential. I am extremely appreciative that you both put up with all of my questions, paper drafts, and emails over the past six years. To the remainder of my committee (Allison Noble, Rolf Jansen, and Seth Cohen), thank you for your thoughtful questions and insights during the annual reviews or Friday afternoon meetings. My work would not have taken shape without your thoroughness. Thank you Teresa Ashcraft for teaching me how to use `Source Extractor` and `Swarp`, while also helping me learn how to work with LBT data. This proved integral to the foundation of my dissertation. I would also like to thank my fellow students and the postdocs (Mansi, Brad, AJ, Chris, Rosalia, Ed, Brent, Duho, Bhavin, Tanmay, Darby, Isabel, Caleb, Lillian, Hansung, Jacqueline, Tim, and Patrick) who have helped me with classes, answered astro 101 questions that I should've already known, or helped me with Python or issues with other software. A huge thank you goes out to John Malloy for all of the shared runs, trails, and suffering. Lastly, I would like to thank all of my family members who have supported me each step of the way. Thank you all.

I would also like to emphasize that this work wouldn't have been possible without any of the following co-authors who have helped me along the way either through proposals, data reduction, or manuscript preparation: Sanchayeeta Borthakur, Rogier Windhorst, Rolf Jansen, Seth Cohen, Timothy Heckman, Jason Tumlinson, Rongmon Bordoloi, Romeel Dave, Caleb Redshaw, Lillian Otteson, Timothy Carleton, Teresa Ashcraft, Anton Koekemoer, Russell Ryan, Mario Nonino, Diego Paris, Andrea Grazian, Andriano Fontana, Emanuele Giallongo, Roberto Speziali, Vincenzo Testa,

Konstantina Boutsia, Robert O’Connell, Michael Rutkowski, Claudia Scarlata, Harry Teplitz, Xin Wang, Marc Rafelski, Norman Grogin, Ray Lucas, and Kris Ganzel. Without your help, the work inside this dissertation wouldn’t have been possible.

Most importantly, the Arizona State University authors want to acknowledge the twenty two Native Nations that have inhabited this land for centuries. Arizona State University’s four campuses are located in the Salt River Valley on ancestral territories of Indigenous peoples, including the Akimel O’odham (Pima) and Pee Posh (Maricopa) Indian Communities, whose care and keeping of these lands allows us to be here today. We acknowledge the sovereignty of these nations and seek to foster an environment of success and possibility for Native American students and patrons.

TABLE OF CONTENTS

| | Page |
|--|------|
| LIST OF TABLES | vii |
| LIST OF FIGURES | viii |
| CHAPTER | |
| 1 INTRODUCTION | 1 |
| 2 DIFFUSE LIGHT IN THE OUTSKIRTS OF GALAXIES | 5 |
| 2.1 Introduction | 5 |
| 2.2 Observations | 8 |
| 2.2.1 Sloan <i>r</i> -band Observations of the GOODS-N Field | 8 |
| 2.2.2 Creating <i>r</i> -band Mosaics | 9 |
| 2.2.3 LBC <i>r</i> -band Catalogs | 12 |
| 2.3 Analysis | 14 |
| 2.3.1 Optimal Resolution versus Optimal Depth LBT <i>r</i> -band Mosaics | 15 |
| 2.4 Results | 19 |
| 2.4.1 Surface Brightness Profile Analysis | 19 |
| 2.4.2 Implications for the Extragalactic Background Light | 21 |
| 2.5 Summary and Conclusions | 23 |
| 3 SEARCHING FOR INTRAGROUP LIGHT IN DEEP U-BAND IMAG- ING OF THE COSMOS FIELD | 30 |
| 3.1 Introduction | 30 |
| 3.2 Observations | 35 |
| 3.3 Mosaic and Catalog Creation | 36 |
| 3.3.1 Floating Zero Point Correction | 36 |

| CHAPTER | Page |
|---|------|
| 3.3.2 Seeing Sorted Stacks | 37 |
| 3.3.3 <i>U</i> -band Catalogs | 40 |
| 3.4 Searching for Intragroup <i>U</i> -band Light | 44 |
| 3.5 Discussion and Summary | 49 |
| 4 DETECTION OF A MULTIPHASE INTRAGROUP MEDIUM: RE- | |
| SULTS FROM THE COS-IGRM SURVEY | 57 |
| 4.1 Introduction | 57 |
| 4.2 Sample | 63 |
| 4.3 HST/COS Observations | 65 |
| 4.4 Results | 68 |
| 4.4.1 Ly α Absorption | 69 |
| 4.4.2 Low and intermediate-ionization tracing tracing cool/warm | |
| gas | 71 |
| 4.4.3 Absorption tracing highly ionized gas | 71 |
| 4.4.4 Absorber Kinematics | 74 |
| 4.4.5 Nature of IGrM | 78 |
| 4.4.6 Origin of O VI Absorbers | 84 |
| 4.4.7 Stacked Spectra | 87 |
| 4.5 Discussion | 88 |
| 4.5.1 Future Outlook | 91 |
| 4.6 Conclusions | 93 |
| 5 CONCLUSION AND FUTURE OUTLOOK | 95 |
| REFERENCES | 99 |

| CHAPTER | Page |
|--------------------------------|------|
| APPENDIX | |
| A EXTRA COS-IGRM FIGURES | 113 |

LIST OF TABLES

| Table | Page |
|--|------|
| 1. SWARP Configuration Parameters adopted for the r -band Mosaics. | 12 |
| 2. SExtractor Configuration Parameters utilized for the r -band Mosaics | 13 |
| 3. Zone definitions for non-uniform LBT coverage of COSMOS | 43 |
| 4. Fractional Group Stack Measurements | 55 |
| 5. Physical Group Stack Measurements | 56 |
| 6. COS-IGrM Sample | 62 |
| 7. Results of Ionization Modeling | 80 |

LIST OF FIGURES

| Figure | Page |
|--|------|
| 1. Seeing Histogram of FWHM of all GOODS-N LBT/LBCR Exposures | 9 |
| 2. Relative Atmospheric Transparency of Each Exposure on 01-17-2013 | 11 |
| 3. Examples of LBT/LBC <i>r</i> -band Optimal Resolution/Depth Mosaics | 16 |
| 4. Galaxy Substructure Across Optimal Resolution and Depth Mosaics | 17 |
| 5. Object Detection with LBT/LBC Mosaics vs. <i>HST</i> | 18 |
| 6. Object Magnitude vs. FWHM for the Optimal Resolution/Depth Mosaics . . | 25 |
| 7. Half-light Radii Showing Additional Light in the Optimal Resolution Mosaic | 26 |
| 8. Surface Brightness Profiles for 20 Bright Objects in GOODS-N | 27 |
| 9. Comparison of <i>r</i> -band Magnitudes Showing Excess Flux | 28 |
| 10. Optimal Resolution and Depth Magnitude Difference for Galaxies Brighter than 21.5 mag | 29 |
| 11. LBT/LBC FOV and UVCANDELS Sub-Region of COSMOS Field | 35 |
| 12. Relative U-band Transparency for 01-26-2020 | 38 |
| 13. FWHM Histogram for all 532 Individual LBT/LBC Exposures of the COS- MOS Field | 39 |
| 14. U-band Optimal Resolution vs. Optimal Depth Comparison | 40 |
| 15. Object FWHM vs U-band Magnitude for Optimal Resolution/Depth Mosaics | 41 |
| 16. Integration Time Exposure Maps for the COSMOS Mosaics | 43 |
| 17. Differential Galaxy Number Counts for the COSMOS Mosaics | 44 |
| 18. Group Halo Mass and Radii Distributions | 46 |
| 19. Example Group Stack Searching for IGrL | 48 |
| 20. IGrL Surface Brightness Measurements as a Function of Observed Wavelength | 51 |
| 21. Environment of Galaxy Group J0841+1406 | 61 |

| Figure | Page |
|---|------|
| 22. Example COS Spectra of Sightline J0841+1406..... | 67 |
| 23. Ly α Column Density as a Function of Group Halo Mass | 68 |
| 24. Ly α Column Densities as a Function of QSO Impact Parameter | 69 |
| 25. O VI Column Density as a Function of Group Halo Mass..... | 72 |
| 26. O VI Column Densities as a Function of QSO Impact Parameter | 73 |
| 27. Line of Sight Velocity Offsets Compared to Group Escape Velocity..... | 75 |
| 28. Line of Sight Velocity Offsets Compared to Group Center and Nearest Galaxy | 77 |
| 29. Ratio of O VI to Ly α as a Function of Impact Parameter | 78 |
| 30. O VI as a Function of the Specific Star Formation Rate of the Nearest Member Galaxy..... | 83 |
| 31. BPT Diagram Showing the Locations of the COS-IGrM Sample | 85 |
| 32. Stacked Spectra of Ly α and O VI | 86 |
| 33. Investigating Potential Ionization Mechanisms..... | 89 |
| 34. Minimum Mass of Oxygen in the IGrM | 92 |
| 35. Environment Plots for the Remaining Groups in the COS-IGrM Sample.... | 115 |
| 36. J0841+1406 Spectra..... | 116 |
| 37. J1017+4702 Spectra..... | 117 |
| 38. J1020+1003 Spectra..... | 118 |
| 39. J1126+1204 Spectra..... | 118 |
| 40. J1127+2654 Spectra..... | 119 |
| 41. JJ1216+0712 Spectra..... | 120 |
| 42. J1301+2819 Spectra..... | 121 |
| 43. J1339+5355 Spectra..... | 122 |
| 44. J1343+2538 Spectra..... | 123 |

| Figure | Page |
|-----------------------------|------|
| 45. J1348+4303 Spectra..... | 124 |
| 46. J1424+4214 Spectra..... | 125 |
| 47. J1428+3225 Spectra..... | 126 |

Chapter 1

INTRODUCTION

The current adopted models for the growth of large scale structure in the Universe suggest that small overdensities merge to create larger dark matter halos. Over time, as these halos continue to merge together, the large scale structure in the Universe begins to take shape (White & Rees, 1978; White & Frenk, 1991). As a result, intermediate sized objects, such as galaxy groups, exist as the most common environment for galaxies to exist (Tully, 1987) and are of utmost importance to study in order to understand how galaxies evolve and grow. However, due to their intermediate size, they are not as routinely studied as galaxy clusters or individual galaxies, which leads to a treasure chest of information and insight to be gained.

Galaxy groups also provide the ideal conditions for significant processes to affect how galaxies evolve. One particular aspect is the increased probability of galaxy - galaxy interactions due to an increased densities of galaxies and slower relative speeds, which lead to an increased amount of time for interactions to take place (Hickson et al., 1977; Barnes, 1985; Purcell et al., 2007). Conversely, the density of galaxies is higher in galaxy clusters; however, the higher relative velocities between galaxies limits the interaction time. These galaxy interactions lead to tidal tails, streams or other regions of diffuse light, and enhanced star formation (Barnes, 1992; Bundy et al., 2005; Elmegreen et al., 2007).

Groups provide a large reservoir of gas for galaxies to utilize in order to continue sustained star formation. Typically, galaxies utilize their large halos of gas, termed the circumgalactic medium (CGM), as a source of gas for accretion and feedback

through galactic winds, star formation, and active galactic nuclei (AGN) activity (Tumlinson et al., 2017). In group environments, the formal definition of the CGM doesn't directly translate and therefore it is theorized that the IGrM should play a role in helping to sustain star formation. Studies of the IGrM can be carried out through direct observations via intragroup light (IGrL), absorption lines in background quasars (QSOs), or cosmological simulations. In this dissertation, we focus on searching for signatures of IGrL and a survey of QSO absorption lines probing galaxy groups.

One method of observing the IGrM is via light emitted through IGrL. This component of the IGrM has been observed most frequently in compact groups of galaxies where galaxy interactions have been hypothesized to remove stars from the member galaxies and distributed them throughout the group. As time passes and the galaxies have more interactions, this cycle continues and is thought to build up IGrL (Mihos, 2004; Murante et al., 2004). An alternate hypothesis is that star formation takes place within the IGrM and forms the stars that contribute towards IGrL (Da Rocha et al., 2008). In this theory, the source of gas to form these stars would either come from tidally stripped gas or from in situ star formation within the IGrM. Most studies have only focused on compact groups, where the optimal conditions hold for IGrL detection. Since compact groups do not represent the majority of galaxy groups in the Universe, the need exists for IGrL to be studied across more typical groups to see if the IGrL formation processes remain the same.

Historically, QSO absorption lines have been the most robust means of detecting diffuse gas surrounding galaxies. This method has primarily been used to study the CGM (Tumlinson et al., 2011, 2017) and the intergalactic medium (Rauch, 1998; Shull et al., 2012); however, it can also be applied to study group environments. This technique relies on a UV bright QSO being located behind a galaxy group on the sky.

Using a UV spectrograph, such as COS aboard *HST*, a spectrum of the QSO can be obtained and the gas comprising the IGrM will imprint absorption lines on the spectrum corresponding to the specific elements present, temperature, and the density. QSO absorption lines are especially powerful as the ability to detect the absorption lines is only dependent on the density of the IGrM and the signal to noise ratio of the spectrum and not on the distance of the group from Earth.

Unfortunately, there are a couple of limitations that exist with this technique. Most significant is that it is rare for a sufficiently bright QSO to be located behind a galaxy group, which leads to the issue of low number statistics. To date, the COS-IGrM survey (McCabe et al., 2021) is the largest sample of QSOs probing the IGrM with 18 sightlines. Additionally, this technique relies on the assumption that the single pencil beam sightline through the group is representative of the entire group. While this is clearly not the case, it is assumed that as more and more sightlines are observed, eventually the differences across the IGrM should average out and statistical conclusions can be made.

This dissertation aims to observe and understand the properties of the IGrM. Chapter 2 begins by utilizing the unique capabilities of the Large Binocular Telescope (LBT) to study low surface brightness regions on the outskirts of galaxies. By utilizing different subsets of all the observations obtained for a particular field on the sky, deep images can be created to highlight galactic structures such as star forming clumps or an image can be optimized to unveil low surface brightness regions and faint tidal tails. These mosaics were used to study faint light from older stellar populations in the outskirts of galaxies in the GOODS-N field.

Chapter 3 utilizes the same stacking methods to create deep images of the COSMOS field with U-band data from the LBT. This deep image was then used to try and

observe signatures of IGrL and place constraints on the processes that lead to the creation and buildup of IGrL. Chapter 4 presents the results of the COS-IGrM Survey, where 18 galaxy groups were paired with background QSOs to study the IGrM through absorption. These results help to determine physical properties of the IGrM and how galaxies evolve in group environments. Lastly, Chapter 5 discusses the general results and places this dissertation into context as well as future outlook for group studies.

DIFFUSE LIGHT IN THE OUTSKIRTS OF GALAXIES

2.1 Introduction

¹Galaxy mergers and interactions play a critical role in galaxy evolution and are observed across cosmic time (Barnes, 1992; Bundy et al., 2005; Lotz et al., 2008, 2011). In the nearby Universe, mergers and interactions are able to be observed with high resolution using the *Hubble Space Telescope* (*HST*). These observations have shown that as redshift increases, galaxies appear more irregular, have closer neighbors, exhibit features of recent interactions, or appear to be in the process of merging (Burkey et al., 1994; Duncan et al., 2019, and references therein). Various studies have visually identified and classified these merging systems based upon appearance (Darg et al., 2010) and features such as tidal tails, streams, and other diffuse/extended flux regions (Elmegreen et al., 2007; Mohamed & Reshetnikov, 2011; Elmegreen et al., 2021). However, these features can be missed by high-resolution *HST* imaging due to their intrinsically low surface brightness.

Tidal tails and bridges of matter between galaxies are clear signatures of past or on-going interactions (Toomre & Toomre, 1972). These interactions are known to trigger star formation and play a critical role in galaxy evolution throughout the Universe (Hernquist, 1989; Conselice, 2014, and references therein). A few studies have

¹This chapter is published under Ashcraft, McCabe et al. (2023) as it is an extension of T. Ashcraft’s dissertation. However, new steps were added to the stacking pipeline resulting in improved mosaics, new analysis of surface brightness profiles, and quantified effects on the EBL contribution. These steps justified inclusion in this dissertation as agreed upon by the committee.

looked for interacting systems within various extragalactic deep fields. For example Elmegreen et al. (2007) examined the Galaxy Evolution from Morphologies and SEDs (GEMS) survey (Rix et al., 2004) and the Great Observatories Origins Deep Survey (GOODS) South field (Giavalisco et al., 2004) for mergers and galaxy interactions to $z \simeq 1.4$. They defined a sample of 100 objects, and measured properties of the galaxies and star-forming clumps within the interacting galaxies. Similarly, Wen & Zheng (2016) identified a sample of 461 merging galaxies with long tidal tails in the COSMOS field (Scoville et al., 2007) using *HST*/ACS F814W (I-band). They only included galaxies in $0.2 \lesssim z \lesssim 1$ which corresponds to rest frame optical light sampled by the F814W filter with a surface brightness limit of $\sim 25.1 \text{ mag arcsec}^{-2}$. However, most of their sample have intrinsic surface brightness $\gtrsim 23.1 \text{ mag arcsec}^{-2}$.

Straughn et al. (2006) and Straughn et al. (2015) identified "tadpole" galaxies, based on their asymmetric knot-plus-tail morphologies visible in *HST*/ACS F775W at intermediate redshifts ($0.3 \lesssim z \lesssim 3.2$) in the Hubble Ultra Deep Field (HUDF; Beckwith et al., 2006). Using multi-wavelength data, they studied rest frame UV/optical properties of these galaxies in comparison with other field galaxies. They measured the star formation histories and ages of these galaxies and concluded that "tadpole" galaxies are still actively assembling either through late-stage merging or cold gas accretion.

The Large Binocular Telescope (LBT) is able to obtain imaging for 4 of the 5 CANDELS (Grogin et al., 2011; Koekemoer et al., 2011) fields that are in the northern hemisphere or around the celestial equator (Ashcraft et al., 2018; Otteson et al., 2021; Redshaw et al., 2022; McCabe et al., 2023). Ashcraft et al. (2018) presented ultra deep *U*-band imaging of GOODS-N (Giavalisco et al., 2004) and created optimal resolution and optimal depth mosaics, which represent the best *U*-band imaging that can be

achieved from the ground. Each mirror of the LBT is equipped with a Large Binocular Camera (LBC), which allowed for parallel U -band and Sloan r -band imaging. With the large field of view (FOV) of the LBC, our GOODS-N observations encompass the *HST* footprint, which makes the complementary, very deep r -band data especially useful for larger survey volumes.

Deep imaging of the CANDELS fields also allows for investigations into the amount to which galaxies contribute to the Extragalactic Background Light (EBL) (McVittie & Wyatt, 1959; Driver et al., 2016; Windhorst et al., 2022a; Carleton et al., 2022, and references therein). Currently, a discrepancy exists between EBL predictions from integrated galaxy counts (Driver et al., 2011, 2016; Andrews et al., 2018) and from direct measurements (Puget et al., 1996; Hauser et al., 1998; Matsumoto et al., 2005, 2011, 2018; Lauer et al., 2021, 2022; Korngut et al., 2022). Ultra-Diffuse Galaxies, diffuse intragroup or intracluster light, as well as faint light in the outskirts of galaxies have all been proposed as sources that would be capable of closing the discrepancy between galaxy counts and direct EBL measurements.

Using the capabilities of the LBT/LBC for deep r -band imaging allows the detection of faint flux in galaxy outskirts in the form of star forming clumps, tidal tails/mergers, and diffuse light. This paper builds upon the previous U -band work of Ashcraft et al. (2018); Otteson et al. (2021); Redshaw et al. (2022) and McCabe et al. 2022 (in prep) by utilizing the seeing sorted stacking procedure to create optimal depth and optimal resolution mosaics of GOODS-N for the r -band obtained simultaneously. Using these mosaics, we attempt to address the level to which faint, extended light in the outer regions of galaxies can contribute to the total observed EBL.

This paper is organized as follows. In §2.2, we describe the acquired data and the creation of optimal depth/resolution mosaics and corresponding object catalogs. §2.3

further investigates the mosaics and describes the tradeoffs between the optimal depth and optimal resolution images. §2.4 analyzes surface brightness profiles for 360 of the brightest galaxies and discusses some of the implications of this additional light with regards to Extragalactic Background Light. Lastly, §2.5 summarizes and discusses these results. Unless stated otherwise, all magnitudes presented in this paper are in the AB system (Oke & Gunn, 1983).

2.2 Observations

The LBCs are two wide field, prime focus cameras, one for each of the 8.4 m primary mirrors of the LBT. The LBCs are unique as one camera is red optimized (LBC-Red; LBCR), while the other is blue optimized (LBC-Blue; LBCB). We utilized the LBCR camera along with the Sloan r -band filter, which has a central wavelength of $\lambda_c = 6195 \text{ \AA}$, a bandwidth of 1300 \AA (full width at half maximum; FWHM), and a peak CCD quantum efficiency of $\sim 96\%$ within the r -band filter. The LBC focal planes are composed of 4 EEV42-90 CCD detectors each, which have an average plate scale of $\sim 0.225''$ (Giallongo et al., 2008).

2.2.1 Sloan r -band Observations of the GOODS-N Field

Using binocular imaging mode, LBC observations of the GOODS-N field were carried out in dark time from January 2013 through March 2014. This mode allowed for U -band observations to be collected with the LBCB camera simultaneous with r -band observations with the LBCR camera. The U -band data were presented in Ashcraft et al. (2018), where the seeing sorted stacking technique and the associated trade off

between optimal resolution and optimal depth mosaics were discussed. Utilizing a combination of US and Italian partner institutions, 838 r -band total exposures were collected using the LBCR with a total integration time of ~ 28 hr (100,727 s). The individual exposures in this data set each had an exposure time of 120.2 s.

We utilized a dither pattern around a common center position for all images taken over many nights, which included a minimal shift to fill in the gaps between detectors and for removal of detector defects and cosmic ray rejection. The *HST* GOODS-N field covers an area of ~ 0.021 deg², which was easily contained inside the LBC’s large FOV of ~ 0.16 deg². Calibration data, bias frames, and twilight sky-flats were taken on most nights, and were used with the LBC pipeline for the standard data reduction steps (see Giallongo et al., 2008, for details).

2.2.2 Creating r -band Mosaics

For each of the 838 individual exposures, the Gaussian FWHM was measured for unsaturated stars in the FOV, with the median value corresponding to the seeing of the entire exposure. As described in Ashcraft et al. (2018), Otteson et al. (2021) and Redshaw et al. (2022), this allows for a seeing distribution to be created for the entire dataset as shown in Figure 1. The median FWHM for all images is $\sim 1.07''$, which is marginally larger than the typical seeing conditions on Mt. Graham for r -band of $0.97'' \pm 0.06''$ (Taylor et al., 2004). Following the prescription from Ashcraft et al. (2018), the optimal depth r -band stack was created with all exposures with $\text{FWHM} \lesssim 2.0''$, which excludes only the 33 images with the worst seeing ($\sim 4\%$ of the dataset). The optimal resolution r -band stack was created using all images with $\text{FWHM} \lesssim 0.9''$, which corresponds to the best 150 exposures ($\sim 18\%$ of the data).

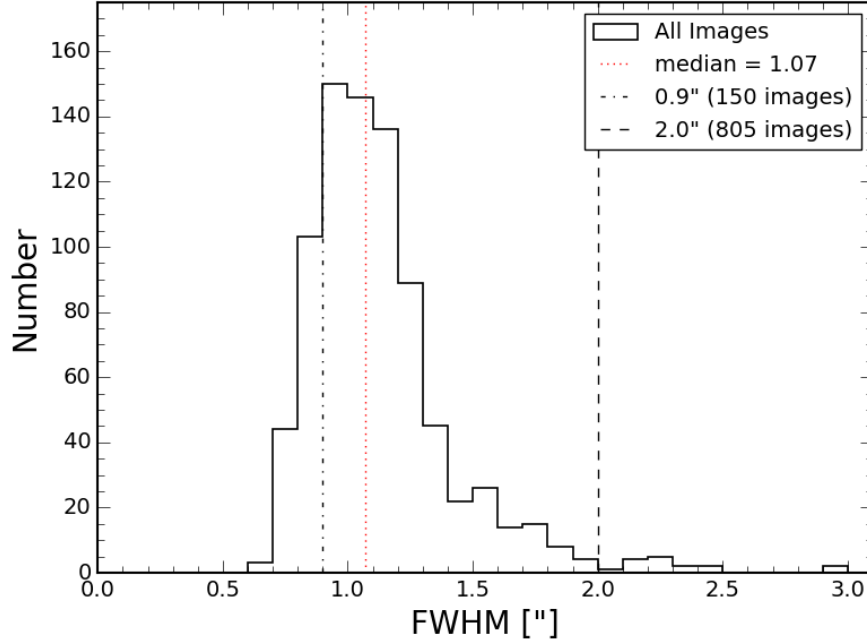


Figure 1. A histogram of the FWHM measured from unsaturated stars for the 838 individual r -band exposures taken in the GOODS-N field with the LBC-Red camera. The dot-dashed line represents the largest FWHM ($0.9''$) included in the optimal resolution mosaic. The vertical dashed line represents the cut-off of FWHM = $2.0''$ used for the optimal depth mosaic, which includes 805 exposures. The median value of the FWHM distribution, FWHM = $1.07''$, is highlighted by the red, dotted line.

Prior to creating the mosaics, the relative transparency was calculated for each of the 838 exposures following the prescription in Otteson et al. (2021); Redshaw et al. (2022) and McCabe et al. (2023). In order to account for the night to night differences in relative atmospheric transparency, the flux ratio between ~ 100 unsaturated stars was taken with respect to the flux values from the Sloan Digital Sky Survey (SDSS) Data Release 16 (Blanton et al., 2017; Ahumada et al., 2020) in the r -band. In this case, a relative transparency value of 1.0 indicates that the median flux from the ~ 100 matched SDSS stars in the r -band is equal to the flux from the same stars in the individual exposure. Relative transparency values less than 1.0 indicate that there is less flux received from these stars than expected based upon SDSS r -band values.

Figure 2 shows the relative transparency for the night of January 17, 2013, where the median transparency varied from ~ 0.94 to ~ 0.98 . We corrected for these night-by-night transparency differences by simply scaling images by the median transparency offset to achieve a transparency of 1.0 in the affected images.

The optimal resolution and optimal depth mosaics were created by combining individual exposures with SWARP (Bertin et al., 2002; Bertin & Amorisco, 2010). Table 1 summarizes some of the key SWARP parameters used for creating these mosaics. The choice of parameters is almost identical to those used previously in Ashcraft et al. (2018), except for using a “BACK_SIZE” parameter of 280 pixels for the mesh size, and a “BACK_FILTERSIZE” of 7. The background parameters were increased to compensate for the increased number of bright saturated stars in individual images compared to the *U*-band data of Ashcraft et al. (2018).

Table 1. SWARP Configuration Parameters adopted for the *r*-band Mosaics.

| Keyword | Value |
|------------------|-------------------------|
| COMBINE_TYPE | CLIPPED |
| WEIGHT_TYPE | MAP_WEIGHT |
| PIXELSCALE_TYPE | Median |
| CENTER (J2000) | 12:36:54.5, +62:15:41.1 |
| IMAGE_SIZE (pix) | 6351, 6751 |
| RESAMPLING_TYPE | LANCZOS3 |
| CLIP_SIGMA | 5.0 |
| CLIP_AMPFRAC | 0.5 |
| BACK_SIZE | 280 |
| BACK_FILTERSIZE | 7 |

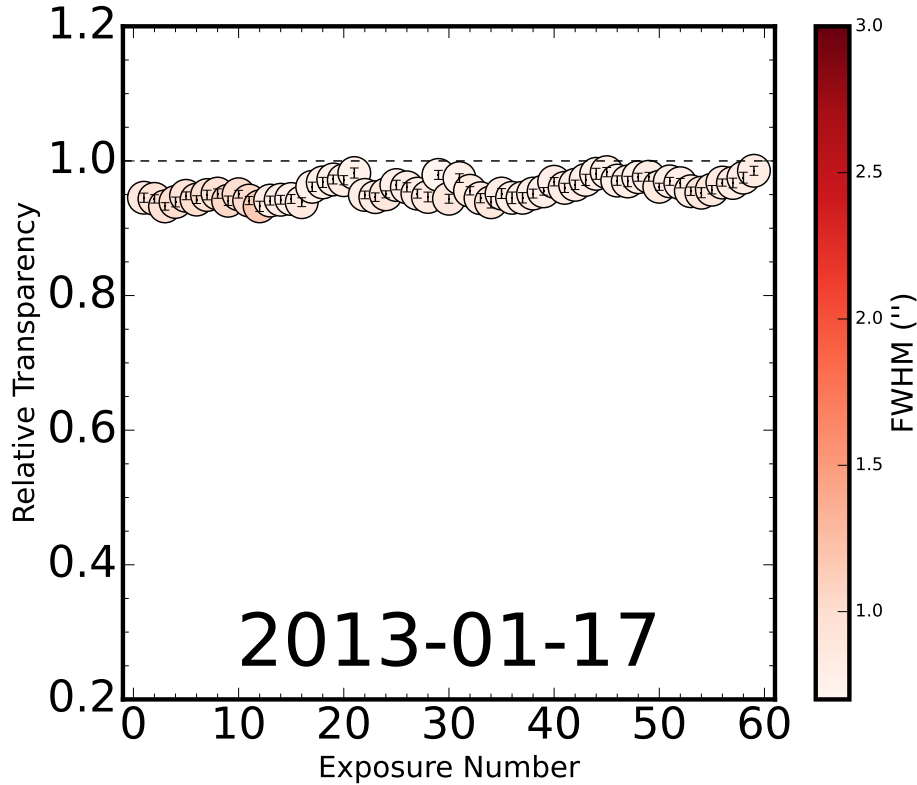


Figure 2. Relative transparency values for the first 59 exposures in the sample from January 17, 2013. The color of each data point represents the median seeing value of ~ 100 unsaturated stars identified in the FOV. The conditions on this particular night allowed for particularly high transparency. On average, across the entire dataset, the relative transparency is $\sim 80\%$ with some nights between 40-60%. The flux across each image was scaled so that the relative transparency values were equal to unity and uniform from image to image and therefore, night to night.

2.2.3 LBC r -band Catalogs

SEXTRACTOR (Bertin & Arnouts, 1996) was used to identify objects and create photometric catalogs. We developed a SEXTRACTOR parameter set which adequately balanced the unique source separation without removing extended, low surface brightness features from their host galaxies. Beginning with the SEXTRACTOR parameters used in the Ashcraft et al. (2018) analysis, various parameters were tweaked to optimize object detection and deblending. For the r -band catalogs, the deblending

parameters “DEBLEND_NTHRESH” and “DEBLEND_MINCONT” were adjusted to more accurately separate objects, especially in the more dense regions of the field. For object detection, a Gaussian filter was used to smooth the image with a convolving kernel (FWHM 2.0 pixels) and a convolution image size of 5×5 pixels. It was found that changing the deblending parameters affected the number of objects detected, but the choice of the smoothing filter did not have a significant impact on the number of extracted objects by SExtractor. However, failure to use a smoothing filter resulted in a large amount of spurious detections. The major SExtractor parameters used to create the final r -band catalogs are listed in Table 2.

Table 2. SExtractor Configuration Parameters utilized for the r -band Mosaics

| Keyword | Opt. Resolution | Opt. Depth |
|-----------------|-----------------|------------|
| DETECT_MINAREA | 6 | 6 |
| DETECT_THRESH | 1.0 | 1.0 |
| ANALYSIS_THRESH | 1.0 | 1.0 |
| DEBLEND_NTHRESH | 64 | 64 |
| DEBLEND_MINCONT | 0.008 | 0.004 |
| WEIGHT_TYPE | MAP_RMS | MAP_RMS |

A mask image was generated to discard any bright stars and their surrounding corrupted areas during the r -band object detection process. The mask was created from the optimal depth image, which had the largest Gaussian wings resulting from the larger FWHM of included exposures. For consistency, the same mask was used for both mosaics. The final object catalogs excluded all objects with the SExtractor FLAGS value larger than 3, and magnitude errors greater than $\sigma m_{AB} > 0.4$ mag. Lastly, photometric zero points were determined by identifying unsaturated stars with AB magnitudes between $r_{AB} \simeq 18$ and $r_{AB} \simeq 22$ mag and matching them to SDSS r -band magnitudes. Approximately 170 stars within this magnitude range were verified in the

LBC images. Stars with nearby neighboring objects were excluded in order to prevent potentially biased flux measurements. We measured photometric zero points of 28.06 and 28.05 mag for the optimal resolution and optimal depth mosaics, respectively.

2.3 Analysis

The trade off between the optimal resolution and optimal depth mosaics is clear when looking at the larger and brighter galaxies in the LBT/LBC mosaics. When lower resolution images (FWHM $\gtrsim 1.0''$) are included, the light from galaxies smooths out and substructures are lost within larger/brighter galaxies (see Fig. 3 and Fig. 4). This phenomena is most apparent when comparing bright face-on spiral galaxies ($r_{AB} \simeq 17.5 - 19.5$ mag) from the r -band optimal resolution ($0.9''$ FWHM) and optimal depth ($2.0''$ FWHM) mosaics and the U -band optimal depth mosaic ($1.8''$ FWHM; Ashcraft et al. (2018)) to HST -ACS V_{606} images of Giavalisco et al. (2004).

Figure 3 clearly illustrates the power of having both ground based optimal resolution and optimal depth images in addition to high resolution HST imaging. In the top panel, a bar is clearly present in the HST image and the r -band optimal resolution mosaic, but is much less discernible in the optimal depth mosaic. This feature is also discernible in the LBT mosaics, especially in the optimal resolution r -band mosaic. Of the detectable features in the LBT mosaics, the smallest scale galaxy features are easier to identify in the optimal resolution mosaic. Most notably, extended low-surface brightness flux in the outer parts of the galaxy is present in the deeper LBT r -band mosaics; however, this flux is not always apparent in the HST images.

Figure 4 shows two additional bright galaxies that fall outside of the HST footprint. However, these galaxies exhibit signatures of star forming clumps within their spiral

arms, which are particularly prominent in the optimal depth images. While clumps are observed to be more prevalent at higher redshifts, these optimal depth and resolution mosaics may be useful in determining the origin and ages of the clumps in addition to serving as analogs for high redshift galaxies (Elmegreen et al., 2009a,b; Overzier et al., 2009; Fisher et al., 2014; Adams et al., 2022, and references therein).

The lower-resolution images also make it more difficult to deblend neighboring objects (see Fig. 5). Example Region 2 in Fig. 5 shows a large region, which is detected as one object by SExtractor in the optimal depth, yet lower-resolution mosaic, indicated by a dashed circle, while SExtractor is able to separate the objects within the dashed circle in the higher-resolution mosaic, indicated by solid circles². All magnitudes presented in Fig. 5 are measured in the optimal depth LBT r -band, except for the objects within the example 2 dashed circle, which come from the optimal resolution r -band catalog. Objects 3, 4, and 6 in Fig. 5 are examples of faint objects detected in the optimal depth LBT image $r_{AB} \gtrsim 28.4$ mag. Only object 6 was detected in the optimal resolution catalog, which is near its limit for reliable detections, and all three regions show almost no measurable flux above the background levels in the *HST* F606W filter.

Figure 5 shows a low-surface brightness region in the example of circle 1, which is barely detectable in the *HST* F606W mosaic. In contrast, the compact object in the example of circle 5 is fainter ($m_{AB} \simeq 27.7$ mag) than the low-surface brightness region of example 1 ($m_{AB} \simeq 26.3$ mag), yet its small size and higher-surface brightness makes it easy to detect in the high-resolution *HST* images.

²Note that within region 2, the galaxy farthest to the right does not appear in the LBT U -band image, as it has been redshifted beyond detection ($z_{spec} = 3.52$)

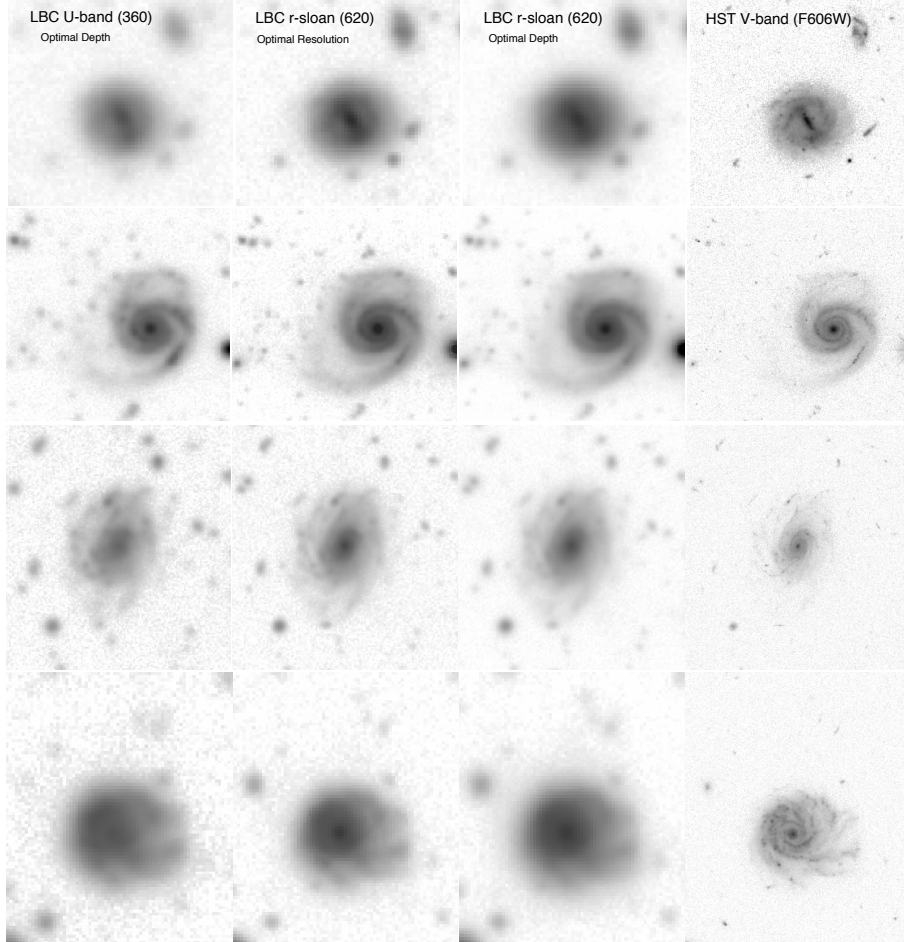


Figure 3. Four bright face-on spiral galaxies in the GOODS-N field, which are also observed in *HST* CANDELS. The top galaxy has $U_{AB} = 20.8$ mag and $r_{AB} = 19.5$ mag, the second galaxy has $U_{AB} = 18.0$ mag and $r_{AB} = 17.5$ mag, the third galaxy has $U_{AB} = 19.9$ mag and $r_{AB} = 18.5$ mag, and the bottom galaxy has $U_{AB} = 19.5$ mag and $r_{AB} = 18.5$ mag. The LBC optimal depth *U*-band image, LBT *r*-band optimal resolution image, LBT *r*-band optimal depth image, and the *HST* ACS *V*-band (F606W; Giavalisco et al. (2004)) image are shown from the left columns to the right columns, respectively.

2.3.1 Optimal Resolution versus Optimal Depth LBT *r*-band Mosaics

In order to compare the optimal resolution and optimal depth mosaics, the catalogs described in §2.2.3 were used to look at object magnitude as a function of FWHM (Figure 6). The solid lines represent the FWHM limits of $\sim 0.65''$ and $\sim 0.90''$ for the

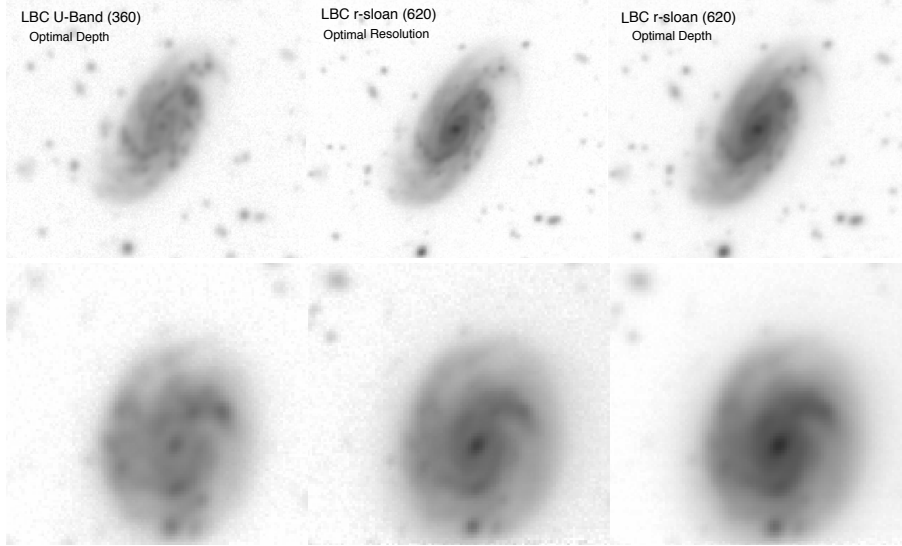


Figure 4. Two of the brightest galaxies in the LBC FOV, but outside the *HST* CANDELS area. The top galaxy has $U_{AB} = 18.3$ mag and $r_{AB} = 16.7$ mag, and the bottom galaxy has $U_{AB} = 19.2$ mag and $r_{AB} = 18.3$ mag. From left to right, the columns show the optimal depth *U*-band image, the optimal resolution *r*-band image, and the optimal depth *r*-band image, respectively. Both of these face-on spirals are sufficiently well-resolved spatially that several sub-structure features including clumps and spiral arms. Most of these features can be seen in both the optimal resolution and optimal depth mosaics. However, the features are sharper and easier to distinguish in the optimal resolution mosaic, while some features blur together in the optimal depth mosaic.

optimal resolution and optimal depth mosaics, respectively. Objects with $m_{AB} \gtrsim 29$ mag generally have sizes “smaller” than the FWHM limit of the Point Spread Function (PSF), and therefore are not reliable detections. The black dashed and dot-dashed lines represent the effective surface brightness limits for the optimal resolution and optimal depth mosaics, respectively, while the red dashed line denotes the star/galaxy separation.

The SEXTRACTOR half-light radii were compared to the equivalent *HST* *V*-band catalog of the GOODS-N field from Giavalisco et al. (2004). For this analysis, only galaxies with magnitudes between $18 \leq m_{AB} \leq 27$ mag as measured in the *HST* *V*-band were selected. Figure 7 shows that the half-light radii measured in the

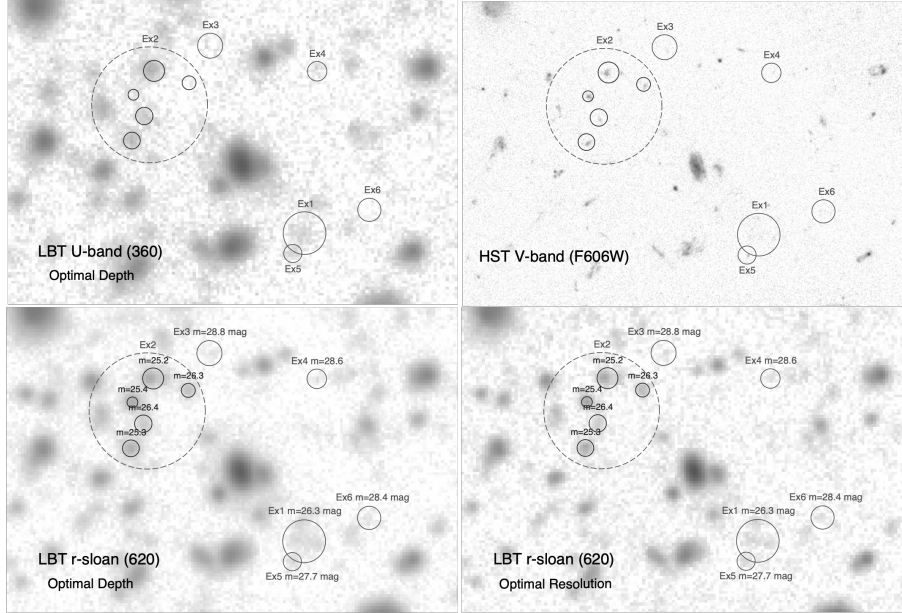


Figure 5. The LBC optimal depth U -band (top left), HST ACS V -band F606W (top right), LBC r -band optimal depth (bottom left), and LBC r -band optimal resolution (bottom right) images are shown for the same region of the GOODS-N field. In this region, the faintest flux detected in the LBT r -band mosaics ($r_{AB} \simeq 28.5$ mag for the optimal depth image) is not always discernible in the HST images (see example regions 3, 4 and 6). The smallest objects in the HST V -band (F606W; $\text{FWHM} \lesssim 0.68''$) are not always detected as single objects in the LBC mosaic catalogs, especially for the lower-resolution optimal depth LBT mosaics. The dashed circle region of example 2 demonstrates an area where SETRACTOR detected a few separate objects as one in the LBT optimal depth r -band mosaic. However, SETRACTOR was able to deblend objects in the LBT optimal resolution r -band mosaic shown by the solid circles within the example region 2 dashed circle. The circle of example 1 shows a low-surface brightness region, which is hard to detect in the HST V -band. In contrast, the compact object in the example 5 circle is fainter than the low-surface brightness region of example 1, yet its small size makes it easy to detect in the high-resolution HST images. All magnitudes are measured in the optimal depth LBT r -band except for the objects within the example 2 dashed circle, which come from the optimal resolution r -band catalog.

optimal resolution image are in better agreement with the HST size measurements with less scatter than those in the lower resolution image. This comparison is represented by a median offset of $0.127'' \pm 0.095''$ for the optimal resolution radii while the optimal depth radii are offset from the HST values by $0.181'' \pm 0.131''$. In order to accurately represent intrinsic object sizes, we subtracted the PSF FWHM-

values of 0.74'' and, 1.00'' in quadrature from the optimal resolution and depth measurements, respectively ($r_{corr} = \sqrt{r^2 - (\text{FWHM}/2)^2}$). For consistency, the PSF-size was subtracted in quadrature for the *V*-band *HST* images as well, but since the *HST*/ACS PSF is so narrow (0.08'' FWHM; see Fig. 10a of Windhorst et al. (2011)), this correction had almost no effect except for the very smallest and most faint objects. Additionally, the right panel of Figure 7 shows that the half-light radii measured from the optimal resolution mosaic are systematically smaller than those measured from the optimal depth mosaic.

2.4 Results

2.4.1 Surface Brightness Profile Analysis

The powerful ability of the optimal depth mosaics to highlight extended, low SB features in the outskirts of galaxies can be utilized to investigate the contribution of diffuse galaxy light to the EBL. For galaxies brighter than $m_{AB} \simeq 21.5$ mag, the azimuthally averaged radial surface brightness (SB) profiles were measured using the custom IDL program `galprof`³ for both the optimal resolution and optimal depth *r*-band mosaics. This left a sample of 360 galaxies suitable for the surface brightness analysis after eliminating galaxies in close proximity to bright stars or the edge of the FOV. The 360 galaxy profiles were analyzed and the excess light in the optimal depth profile was ranked as “confident”, “potential”, or “identical”. Surface brightness profiles ranked as “confident” exhibited a ~ 1.0 mag arcsec⁻² difference in the two profiles

³<http://www.public.asu.edu/~rjansen/idl/galprof1.0/galprof.pro>

over multiple radial points or had multiple data points between the two profiles that were separated by more than the 1σ uncertainty ranges plotted. Profiles ranked as “potential” were classified by a ~ 0.5 mag arcsec $^{-2}$ difference between the two profiles. However, typically the uncertainty ranges in the optimal depth and resolution data points encompassed the corresponding data point, which did not allow for as confident of a classification. The majority of the surface brightness profiles were identified as “identical”, where there was no apparent difference between the optimal depth and optimal resolution profiles.

Prior to analyzing the surface brightness profiles, we measured the surface brightness sky limits at which the two mosaics began to significantly differ. In order to accomplish this, model galaxies with pure exponential disk profiles matching the size of actual galaxies with $m_{AB} \simeq 19\text{--}21.5$ mag were created. Approximately 250 non-saturated stars were used to create a model PSF-star for both the optimal resolution and optimal depth mosaics. The model galaxies were then convolved with the corresponding PSF and random background pixels were sampled to create a background map. Then, `galprof` was run to create surface brightness profiles of the model galaxies. In this analysis, we find the optimal resolution and depth profiles deviated at surface brightness levels of $\mu_r^{AB} \sim 31$ mag arcsec $^{-2}$.

Figure 8 shows a representative selection of 20 out of 360 surface brightness profiles for galaxies in the optimal resolution (blue) and optimal depth (red) mosaics. 16/20 do not exhibit any distinguishable difference between the two profiles to $\mu_r^{AB} \lesssim 31$ mag arcsec $^{-2}$ between the profiles and were categorized as “identical”. Galaxies A, B, C, and D are four examples of galaxies that were ranked as “confident” or “potential” candidates for having significant additional light in the optimal depth surface brightness profiles. Galaxies A and D were categorized as “potential” since

they exhibited ~ 0.5 mag arcsec $^{-2}$ differences in surface brightness with both profiles being within the uncertainty ranges of the other. However, galaxies B and C show larger, more robust differences between the optimal depth and resolution profiles⁴.

2.4.2 Implications for the Extragalactic Background Light

Driver et al. (2016, Fig. 2) showed that the number density of galaxies in the r -band peaks at $m_{AB} \simeq 19$ – 24 mag. Thus, this subset of galaxies constitutes a representative sample of galaxies which significantly contributes to the EBL to surface brightness levels of $\mu_r^{AB} \lesssim 31$ mag arcsec $^{-2}$, where the background levels of the optimal depth and optimal resolution mosaics begin to differ. Of the 360 galaxies with surface brightness profiles, only 19 were labeled as “confident” and 32 galaxies were labeled as “potential”. Therefore, 5-14% of galaxies in this sample have excess flux in their outskirts out to surface brightness levels of $\mu_r^{AB} \lesssim 31$ mag arcsec $^{-2}$, which could contribute to missing, diffuse EBL light as summarized by Driver & Robotham (2010); Driver et al. (2016) and Windhorst et al. (2018). However, the possibility of more uniform, missing flux from all galaxies cannot be ruled out as it would be diffuse enough across the LBT FOV where it would be removed during the SWARP background subtraction process. This excess r -band light could be the result of an older population of stars in the galaxy outskirts, star formation being traced by H α out to redshifts of $z \lesssim 0.2$, or tidal tails from galaxy interactions.

Additional light in the outskirts of galaxies is also observed though a slight offset in the magnitude difference between the optimal resolution and depth catalogs. This

⁴The bottom right profiles in Figure 8 were not labeled as “potential” or “confident” as the optimal depth profile was not consistently brighter than the optimal depth.

is shown in Figure 9, where for all galaxies between 18 and 28 mag, the median magnitude difference is 0.023 ± 0.143 mag. This positive magnitude offset indicates that on average, there exists additional light in the outskirts of the optimal depth galaxies. With regards to galaxies brighter than 21.5 mag, which correspond to the magnitude range for the 360 galaxies with surface brightness profiles, Figure 10 shows that additional flux exists in the optimal depth images. The magnitude difference between the optimal resolution and optimal depth sources exhibit a positive offset (0.024 ± 0.014 mag) from zero, which indicates that the same galaxies are brighter in the optimal depth mosaic. On average, median offset between the optimal resolution and optimal depth magnitudes for the full sample of galaxies between 18 and 28 mag is not robust given the uncertainties. However, when looking at the subset of galaxies brighter than 21.5 mag, there is clear evidence that additional flux exists. This additional flux is attributed to diffuse light in the galaxy outskirts that is visible through long periods of integration from the ground.

In addition to the surface brightness profile analysis, the total contribution of light in galaxy outskirts to the EBL was calculated by integrating the normalized galaxy counts up to the optimal resolution and optimal depth completion limits of ~ 27 mag following the methods in Driver et al. (2016); Carleton et al. (2022) and Windhorst et al. (2022a). Beginning with the differential number counts from the optimal resolution and optimal depth mosaics, the number counts began to become incomplete after ~ 27 mag. As stated in Driver et al. (2016); Carleton et al. (2022) and Windhorst et al. (2022a), the majority of the EBL is comprised of light from galaxies between 18-24 mag. As a result, by integrating the galaxy counts up to the completeness limit of 27 mag provides an accurate measure of the integrated EBL. Therefore, the contribution to the EBL which is from any additional light in the

outskirts of galaxies in the optimal depth mosaic would be represented by the difference between the total energy (EBL) from the integrated galaxy counts for each of the two mosaics. This analysis showed that the EBL contribution from the optimal depth and optimal resolution mosaics are 3.52 and $3.33 \text{ nW m}^{-2} \text{ sr}^{-1}$, respectively. Therefore, the difference between these values represents the expected EBL contribution from the diffuse flux in the outskirts of galaxies in the optimal depth mosaic. This corresponds to $0.19 \text{ nW m}^{-2} \text{ sr}^{-1}$, which amounts to $\sim 5\%$ of the total EBL in the Sloan r -band (see Fig. 1 in Windhorst et al. (2022a)). Since these independent methods of searching for additional light in the outskirts of galaxies provide similar results, it can confidently be stated that only a small fraction ($\sim 5\text{-}14\%$) of extra light in galaxy outskirts is available to contribute towards missing EBL light.

2.5 Summary and Conclusions

838 r -band exposures (~ 28 hours) were obtained between December 2012 and January 2014 of GOODS-N in order to examine the trade-off between optimal image resolution and depth. Following the seeing sorted stacking method detailed in Ashcraft et al. (2018), the best seeing images were stacked to create optimal depth and optimal resolution mosaics. The optimal depth mosaic was found to be necessary for the study of low surface brightness regions presented in this work. The sacrifice in resolution was complemented by increased surface brightness sensitivity down to $\mu_r^{AB} \leq 31 \text{ mag arcsec}^{-2}$.

The main challenge for photometric measurements was to overcome the natural

confusion limit for separating objects, which occurs once faint objects are closer than $\sim 1.0''$ in ground based images (Windhorst et al., 2011). In order to accurately deblend sources in the mosaics, SExtractor in dual image mode was utilized in order to deblend and detect objects using the optimal resolution mosaic. Within the optimal depth and optimal resolution mosaics, objects can be detected to $m_{AB} \sim 29$ and $m_{AB} \sim 28.5$ magnitudes, respectively.

Surface brightness profiles were measured for the 360 brightest galaxies with $r_{AB} \lesssim 21.5$ mag in both the optimal resolution and optimal depth mosaics. Galaxies with magnitudes $m_{AB} \lesssim 21.5$ provide a representative sample of galaxies that could contribute significantly to the Extragalactic Background Light in the r -band (Driver et al., 2016). These surface brightness profiles show marginal differences between the optimal resolution and optimal depth mosaics to surface brightnesses of $\mu_r^{AB} \sim 31$ mag arcsec $^{-2}$. Only 19/360 galaxies confidently exhibited excess flux in the optimal depth radial profiles, while another 32/360 galaxies were categorized as “potentially” having excess flux in the outskirts.

As a result, on average, we conclude that only ~ 5 - 14% of extra light in the outskirts of galaxies are likely to contribute to the Extragalactic Background Light out to surface brightness levels of ~ 31 mag arcsec $^{-2}$. The EBL contribution from the outskirts of galaxies was found to be $\sim 5\%$ of the EBL determined from the integrated galaxy counts. We find that while there is some contribution to the EBL from diffuse light in galaxy outskirts, there is not enough of a contribution in the r -band to close the discrepancy between direct EBL measurements (Puget et al., 1996; Hauser et al., 1998; Matsumoto et al., 2005, 2018; Lauer et al., 2021; Korngut et al., 2022) and predicted values (Driver et al., 2011, 2016; Andrews et al., 2018).

In the era of JWST, the detection of interacting galaxies and tidal tails out to

$z \sim 1$ in addition to diffuse light in the outskirts of galaxies is of particular significance. As shown in early JWST results from Finkelstein et al. (2022), Windhorst et al. (2022b) and references therein, tidal tails and diffuse light is commonly observed. This observed diffuse light is evidence that the $\sim 5\text{-}14\%$ additional light discovered in this paper and Ashcraft et al. (2018) in the U-band appears to be commonplace, especially at $z > 1$. As a result, future studies may be able to refine the limits for the contribution from tidal tails and diffuse light towards the EBL that are presented in this paper.

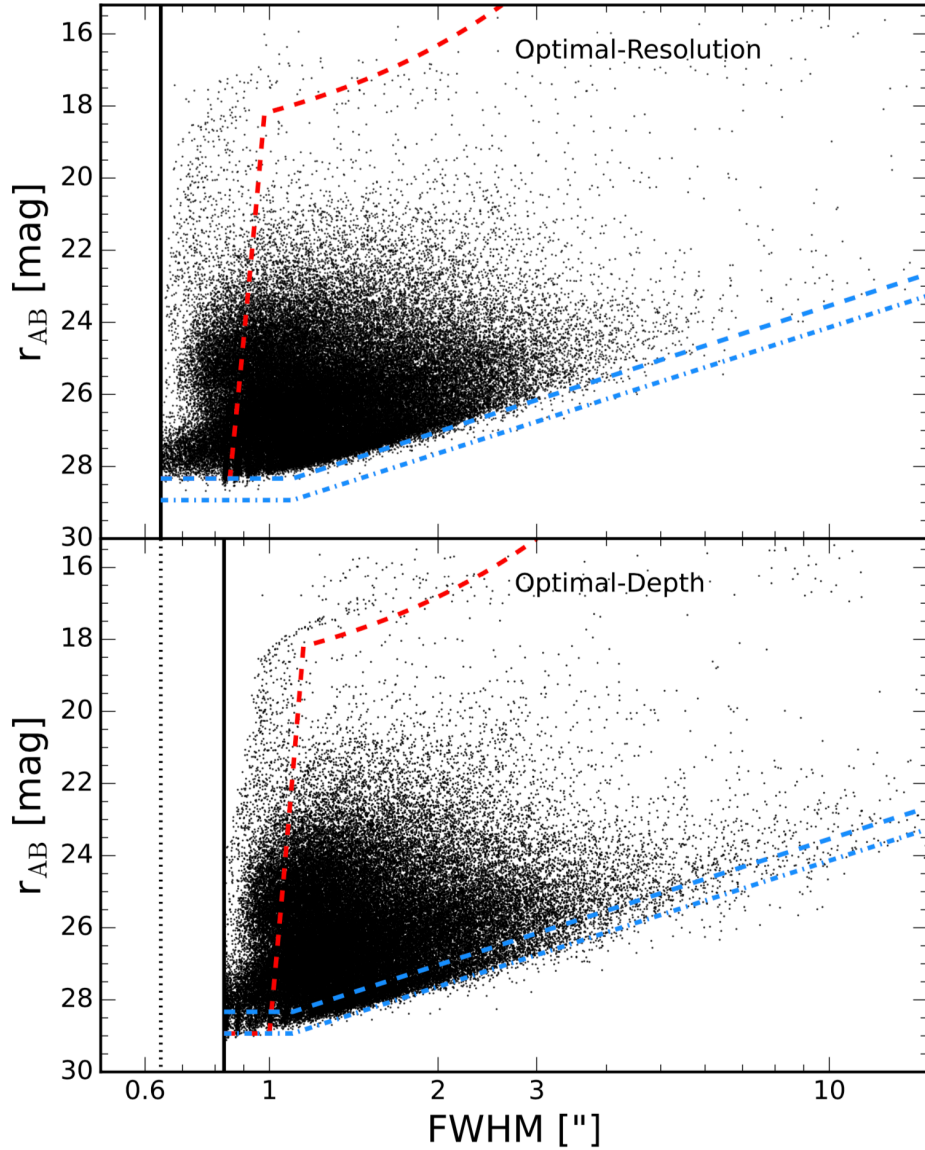


Figure 6. Total r -band object magnitude vs. FWHM as measured with SExtractor for the optimal resolution (top) and optimal depth (bottom) mosaics. The solid, vertical lines represent the lower FWHM limit used in each image, while the dotted, vertical line in the optimal depth panel extends down from the optimal resolution FWHM limit for comparison. The blue, dashed and dot-dashed boundaries, which are identical in both panels, represent the effective surface brightness limits of the optimal resolution and optimal depth mosaics, respectively. Last, the red, dashed curves show the demarcation between stars and galaxies.

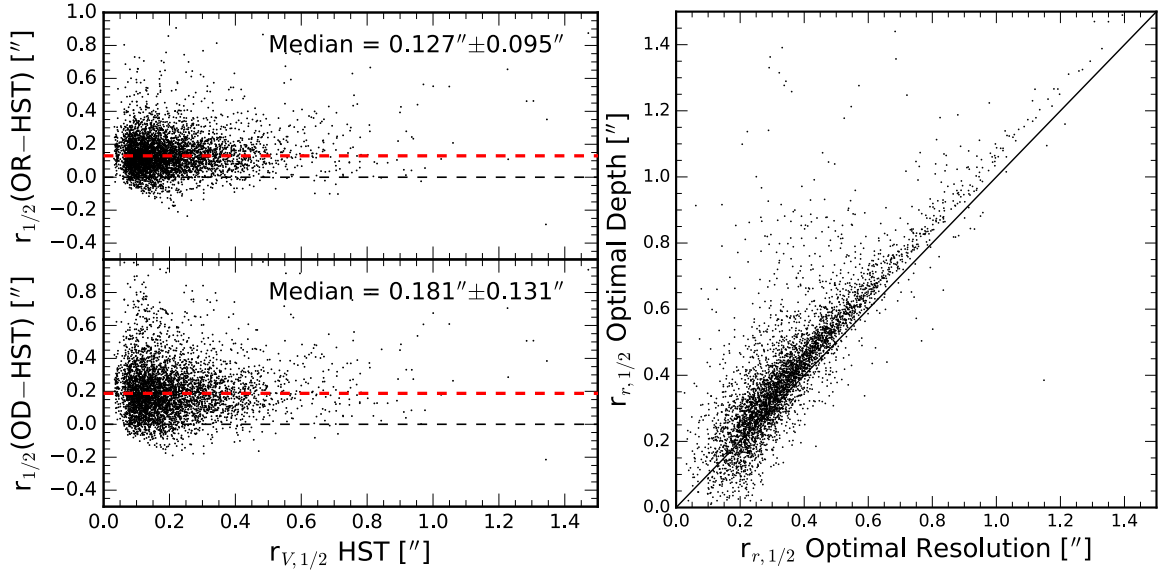


Figure 7. Comparison plots of half-light radii measured with SExtractor for the two LBT mosaics and the *HST* *V*-band (Giavalisco et al., 2004). The galaxies were selected to have $18 \leq m_{AB} \leq 27$ mag as measured in the *HST* *V*-band, and the half-light radii are corrected for the PSF FWHM by the factor $r_{corr} = \sqrt{r^2 - (FWHM/2)^2}$. The left panels show the optimal resolution (OR; top) and optimal depth (OD; bottom) apparent offsets from the HST *V*-band half-light radii. The left two panels clearly illustrate that there is better agreement between the HST half-light radii and the optimal resolution mosaic. The right panel compares the half-light radii between the optimal depth and optimal resolution LBT mosaics, where the measurements are tightly correlated, but with half-light radii measured in the OD mosaic systematically larger than those measured in the OR mosaic.

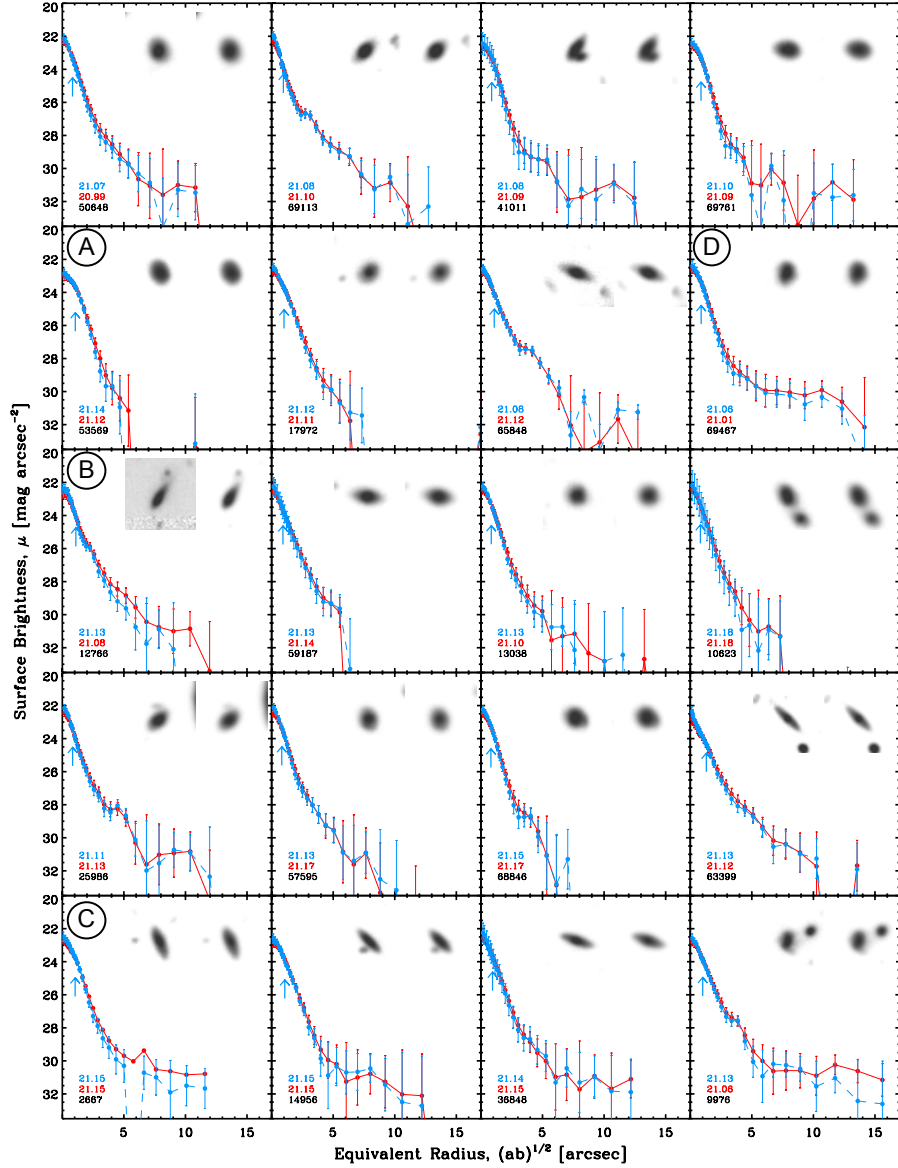


Figure 8. Radial surface brightness profiles for 20 of the 360 brightest objects with $r_{AB} \lesssim 21.5$ mag. The blue data points show the surface brightness profile for the optimal resolution image, while the red points show the corresponding profile for the optimal depth image. The total integrated r_{AB} magnitudes from the profiles are listed in the lower left corner. The blue arrow represents the half-light radius measured with SExtractor. The galaxy inset images show the optimal resolution (left) and optimal depth (right) images. Galaxies A, B, C, and D clearly show excess flux in the outskirts of the optimal depth surface brightness profiles at levels brighter than $r_{AB} \lesssim 31$ mag.

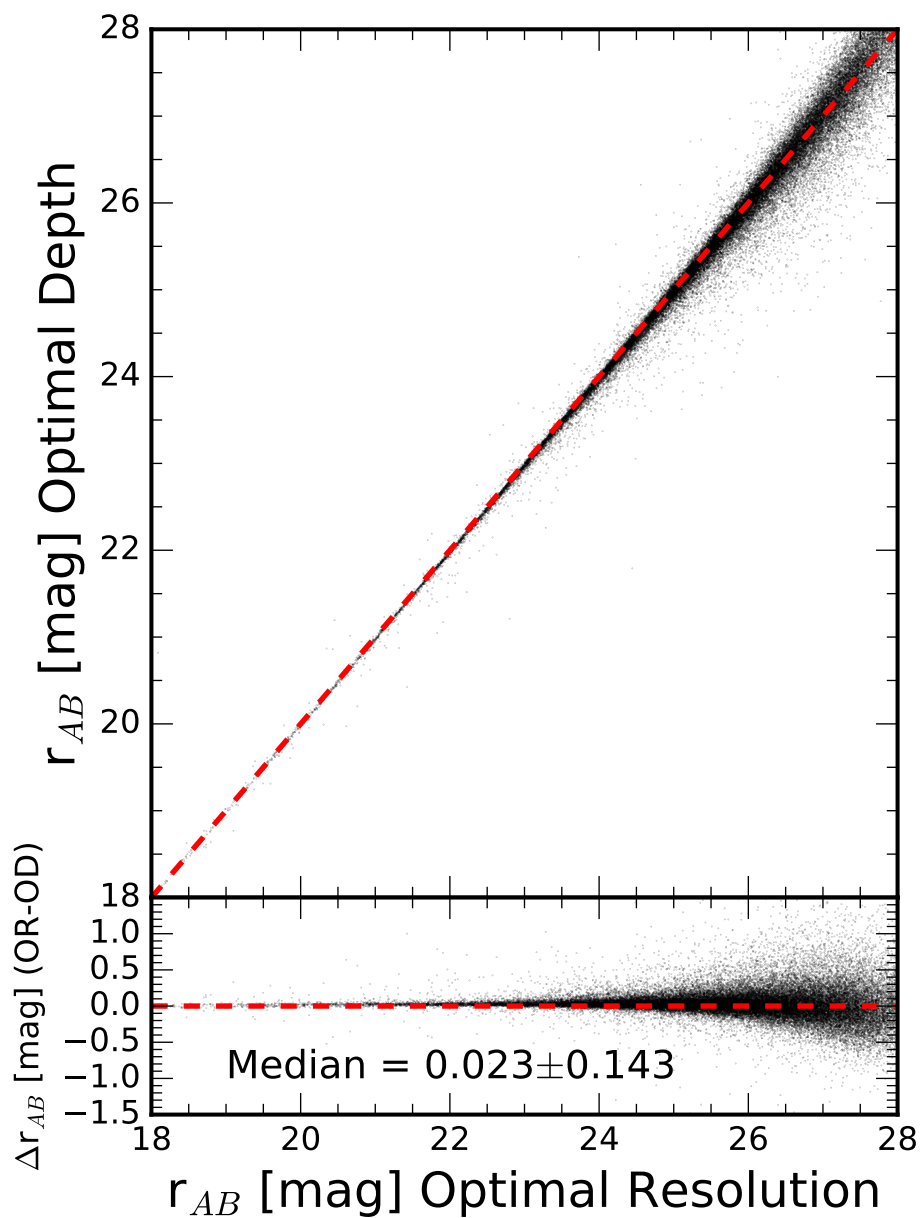


Figure 9. Comparison of total r -band magnitudes measured by SExtractor, using dual image mode, in the optimal resolution (OR) and the optimal depth (OD) mosaics. The bottom panel shows the OR - OD magnitude difference objects in the two catalogs. On average, there is little excess light in the optimal depth images than observed in the corresponding optimal resolution image. This aligns with what is observed in the surface brightness profile analysis where 10–14% of galaxies are observed to have excess r -band flux in their outskirts.

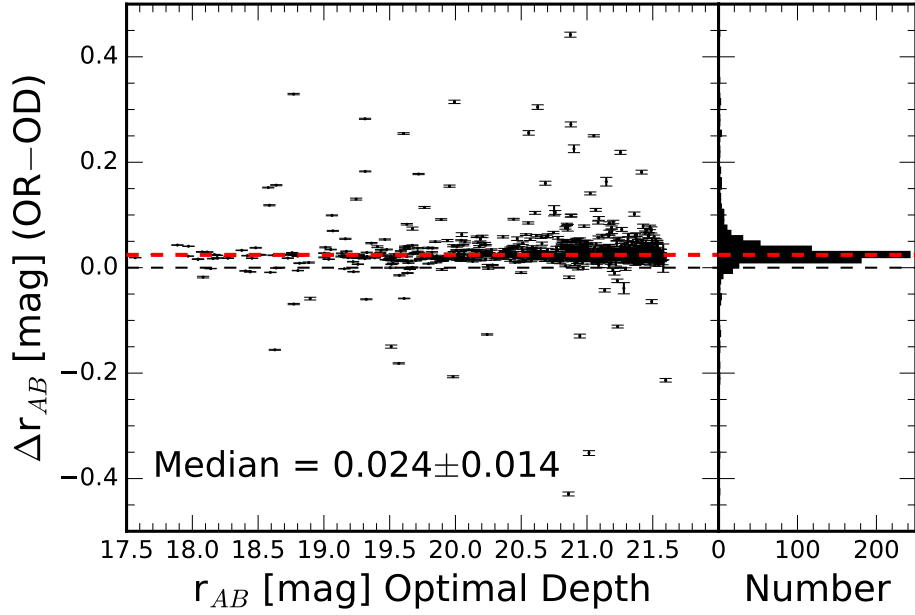


Figure 10. The difference in object magnitude between the optimal resolution and optimal depth mosaics for all galaxies brighter than 21.5 mag, the same magnitude range as for the surface brightness profile analysis. A systematic offset exists between the optimal resolution and optimal depth magnitudes (0.024 mag), which indicates the presence of additional light in the optimal depth mosaic. This small offset aligns with the surface brightness profile analysis which found, on average, a faint amount of additional light due to the low surface brightness outskirts of galaxies that is recovered in the r -band optimal depth mosaic.

SEARCHING FOR INTRAGROUP LIGHT IN DEEP U-BAND IMAGING OF THE COSMOS FIELD

3.1 Introduction

⁵The hierarchical structure of galaxy formation predicts that large structures in the Universe form through the merging of smaller halos which began as small overdensities (White & Rees, 1978; White & Frenk, 1991; Springel et al., 2005; De Lucia et al., 2006). As a result, the majority of galaxies today are observed to be located in group environments which reside in dark matter halos with masses between 10^{12} – $10^{14} M_{\odot}$ (Tully, 1987; Karachentsev et al., 2004). Groups have therefore been of particular interest in hopes of understanding how group environments impact galaxy evolution. In order to fully characterize group environments, the gas gravitationally bound to the dark matter halo, termed the intragroup medium (IGrM), must be observed and understood.

For higher mass halos, the IGrM has been observed through X-ray emission (Mulchaey et al., 1996a; Helsdon & Ponman, 2000a; Mulchaey, 2000); however, the majority of groups do not have gravitational potentials sufficient for X-ray emission from gas at their virial temperature. Quasar (QSO) absorption lines provide an alternative means of observing the IGrM. Despite being limited by chance alignment, QSO absorption lines allow for diffuse gas to be observed independent of redshift and only limited by spectral signal to noise and gas column density. Mulchaey et al.

⁵This chapter is published as McCabe et al. (2023)

(1996b) predicted that gas at the virial temperature of typical groups could be traced by broad, shallow O VI absorption with the absence of cooler transitions such as C II, Si II, and N V. Early studies by Tripp et al. (2000), Tripp & Savage (2000) and Stocke et al. (2006) observed O VI in IGrM sightlines, but the data were insufficient to correlate O VI with the IGrM. Additional IGrM surveys by Stocke et al. (2019) and McCabe et al. (2021) concluded that the dominant, volume filling component of the IGrM should be traced by higher ionization transitions and that O VI can be evidence of multiphase gas within the group halos. While QSO absorption lines have provided the easiest means of observing the IGrM, they are severely limited by both the number of QSO sightlines aligned behind groups and the absence of any transverse spatial information which direct imaging provides.

Another component of the IGrM, intragroup light (IGrL), has been observed in compact groups of galaxies, where the IGrM is expected to be heavily influenced by galaxy interactions and increased dynamical friction resulting from the lower velocity dispersion of the group members (Hickson et al., 1977; Barnes, 1985; Purcell et al., 2007, and references therein). Combinations of tidal processes and interactions are thought to remove stars from galaxies and strand them within the larger group halo. Since these stars remain bound to the group, IGrL begins to build up slowly (Mihos, 2004; Murante et al., 2004; Purcell et al., 2007). As a result, Hickson Compact Groups (HCG; Hickson, 1982; Hickson et al., 1992) provided an ideal environment to observe IGrL due to the combination of high density and low velocity dispersions. Early studies by Nishiura et al. (2000) and White et al. (2003) found evidence of diffuse IGrL in HCGs 79 and 90, which corresponds to 13% and 45% of the total group light, respectively. Similarly, Da Rocha & Mendes de Oliveira (2005) acquired deep B- and R- band images of HCGs 79, 88 and 95 and found a significantly higher fraction of

the total group light in the IGrL of HCG 79 of 33% in the R-band and 46% in the B-band. However, for HCG 95, the IGrL was much less prominent as it was only 11% and 12% in the B and R bands respectively. No IGrL was detected in HCG 88 down to surface brightness levels of $29.1 \text{ mag arcsec}^{-2}$ in the B-band and $27.9 \text{ mag arcsec}^{-2}$ in the R-band. As a result, Da Rocha & Mendes de Oliveira (2005) concluded that the IGrL becomes more prominent as the groups become more dynamically evolved.

Da Rocha et al. (2008) extended this analysis to three more Hickson Compact Groups and found similar results. For HCGs 15, 35 and 51, the fraction of IGrL ranged between 15-31% in the B-band and 11-28% in the R-band and the same correlation between IGrL fraction and indications of dynamical evolution appeared to exist. The B-R colors of the IGrL in HCGs 35 and 51 were determined to be bluer than the colors of the member galaxies, which may indicate that star forming regions, either in-situ or from tidal stripping, have a strong contribution to the IGrL. Other studies of HCGs by Aguerri et al. (2006) and Poliakov et al. (2021) found similar fractions of IGrL down to surface brightness levels of $\sim 28 \text{ mag arcsec}^{-2}$ in the r -band and an upper limit of 4.7% of the group light for HCG 44 to $30.04 \text{ mag arcsec}^{-2}$ in the B-band. In each of these studies, the process in which interactions and tidal stripping lead to a build up of IGrL has been supported by observed correlations between the amount of IGrL and the fraction of early type galaxies in compact groups (Aguerri et al., 2006; Da Rocha et al., 2008; Poliakov et al., 2021).

Expanding the search for IGrL to looser groups, Watkins et al. (2014) searched for IGrL in the M96/Leo I group. Using a combination of B- and V-band images from the Burrell Schmidt Telescope on Kitt Peak, no diffuse IGrL was observed down to surface brightness levels of $\mu_B = 30.1 \text{ mag arcsec}^{-2}$. As a result, the authors suggest that frequent interactions are necessary to produce IGrL and that the M96 group is

either not in an evolved enough state, too low in mass, or lacking a sufficient density of galaxies required for frequent/strong interactions.

Spavone et al. (2018) and Raj et al. (2020) used the Fornax Deep Survey to study the IGrL of the loose groups NGC 5018 and Fornax A, respectively. The NGC 5018 group was found to have significant amounts of IGrL that constitute 41% of the total group light in the g -band. The $g - r$ color of the detected IGrL is consistent with the member galaxies, suggesting that tidal interactions are primarily responsible for its formation. Raj et al. (2020) observed significantly smaller fractions of IGrL as only 16% of the total group's g -band light was in the form of IGrL. Similarly to Spavone et al. (2018) and studies of compact groups by Aguerri et al. (2006); Da Rocha et al. (2008) and Poliakov et al. (2021), the authors believe that the IGrL observed was a result of tidal interactions from the disruption of dwarf galaxies in the group.

Cattapan et al. (2019) studied the dynamically young, un-virialized Dorado group and observed IGrL out to surface brightness limits of $30.11 \text{ mag arcsec}^{-2}$ in the g -band and $28.87 \text{ mag arcsec}^{-2}$ in the r -band. It was determined that tidal interactions were the cause for the build up of IGrL in this group. At higher redshifts, Martínez-Lombilla et al. (2023) detected IGrL to limiting surface brightnesses of $30.76 \text{ mag arcsec}^{-2}$ and $29.82 \text{ mag arcsec}^{-2}$ in the g and r -bands, respectively, which corresponds to IGrL fractions between 2 and 36%. This group was found to be dominated by early-type galaxies, which indicates that the group is dynamically evolved.

To date, there has not been any statistical survey of IGrL across more typical groups across a single field. While compact groups represent the optimal case for IGrL detection and analysis, they do not represent the majority of groups in the universe due to the inherent population, isolation, and density requirements (Hickson, 1982). Therefore, a combination of deep imaging combined with a robust galaxy

group catalog is necessary for a statistical study of IGrL without bias towards bright, dense, and rich groups. Suitable deep, ground based imaging was secured in support of UVCANDELS (PI H. Teplitz), which aimed to provide UV coverage of the Cosmic Assembly Near-Infrared Deep Extragalactic Legacy Survey (CANDELS; Grogin et al., 2011; Koekemoer et al., 2011) fields: Great Observatories Origins Deep Survey (GOODS; Giavalisco et al., 2004) North and South, the Extended Groth Strip (EGS; Davis et al., 2007), and the Cosmic Evolution Survey (COSMOS; Koekemoer et al., 2007; Scoville et al., 2007).

As part of the GOODS-N UVCANDELS observations, Ashcraft et al. (2018) used the capabilities of the Large Binocular Camera (LBC) on the Large Binocular Telescope (LBT) to complement the *Hubble Space Telescope* (HST) parallel WFC3/UVIS F275W and ACS/WFC F435W observations with ground based U -band ($\lambda_c \simeq 359$ nm; $\Delta\lambda \simeq 54$ nm) imaging. Ashcraft et al. (2018) pioneered the seeing sorted stacking method, which was used by Otteson et al. (2021), Redshaw et al. (2022) and Ashcraft et al. (2023) to stack individual exposures (starting with the best seeing) incrementally to create “optimal depth” and “optimal resolution” mosaics. The optimal resolution and optimal depth stack FWHM cutoffs were dependent upon the seeing distributions for each individual exposure, but only the best $\sim 10\%$ of the exposures were used for the optimal resolution mosaic and only the worst $\sim 5 - 10\%$ were excluded from the optimal depth mosaic. This method allows the brightest galaxies to be studied through the optimal resolution mosaics, where large features appear to be resolved. Additionally, faint regions with low surface brightness (i.e. faint outskirts, tidal tails, plumes, clumps, etc.) are more easily studied in the slightly deeper, optimal depth mosaics, where an increased number of photons outweighs the need for higher resolution. Furthermore, since adaptive optics are not possible in the U -band, this

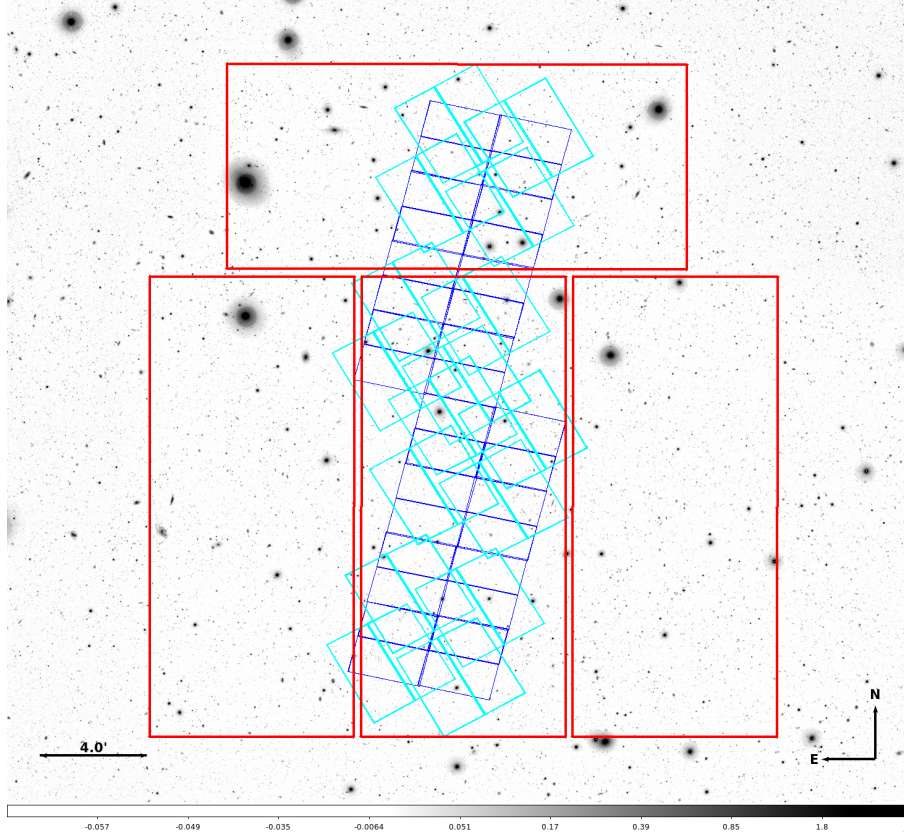


Figure 11. A subsection of the full LBT/LBC U -band optimal depth COSMOS mosaic showing the UVCANDELS sub-region. The cyan and blue outlines represent the HST/ACS and $HST/WFC3$ footprints, respectively. These regions fit within a single LBC pointing, which is outlined in red.

method is necessary to mitigate the variable atmospheric effects that are present, even at an excellent observing site (Taylor et al., 2004).

In order to search for IGrL, we will use the LBT/COSMOS U -band optimal depth mosaic in conjunction with the zCOSMOS 20k galaxy group catalog (Knobel et al., 2012) to identify and stack group backgrounds. While COSMOS is a large, ~ 2 square degree field centered at R.A.=10:00:28.6 and Dec=+02:12:21, we limit our analysis to the central area of the field, which contains the UVCANDELS footprint (see Figure 11).

This paper is organized as follows: in §3.2, we describe the LBT observations, and in §3.3 we discuss the stacking procedure along with the creation of the object catalogs. §3.4 describes the search for diffuse, intragroup light in the UV through galaxy group stacks. Lastly, in §3.5, we summarize our results and provide future outlook towards the search for IGrL. Unless stated otherwise, all magnitudes listed in this paper are in the AB system (Oke & Gunn, 1983) and Planck 2018 cosmology is adopted (Planck Collaboration et al., 2020).

3.2 Observations

We used the Large Binocular Cameras (LBCs; Giallongo et al., 2008) to obtain 532 observations of the COSMOS field. The twin, wide-field instruments at the prime foci of the LBT each have a $\sim 23.6' \times 25.3'$ field of view (FoV) and are able to simultaneously observe the same target with red and blue optimized CCDs. The LBC-red camera is optimized for the V – Y bands (500 – 1000 nm), while the LBC-blue camera is optimized for the UV – R bands (350 – 650 nm) which are the focus of this paper. The two cameras contain four $4\text{ K} \times 2\text{ K}$, E2V 42-90 CCDs, which are characterized by: a gain of $\sim 1.75\text{ e}^-/\text{ADU}$, read-noise of $\sim 9\text{ ADU}$, and a plate scale of $\sim 0.2254''\text{ pix}^{-1}$. For all LBC observations discussed in this paper, the SDT U_{spec} filter was used. The bandpass of this filter when combined with the detector quantum efficiency and the telescope/instrument optics is characterized by a central wavelength of $\lambda_c = 3590\text{ \AA}$, a band width of 540 \AA , and a peak throughput of $\sim 38\%$ (Figure 2 of Giallongo et al., 2008).

The majority of these LBC observations were obtained between 2007 and 2014, while an additional set of observations were carried out in December 2019 and January

2020 in support of UVCANDELS. In total, 532 individual exposures were obtained of the entire COSMOS field, with the newest 94 focusing on the UVCANDELS region. Each observation was uniquely dithered, so that the detector gaps were adequately covered and cosmic rays could be robustly rejected. All images were processed by the Italian LBT partners, involving bias subtraction, flat-fielding, and astrometric calibration onto GAIA/DR3, through the LBC reduction pipeline as detailed in Giallongo et al. (2008).

3.3 Mosaic and Catalog Creation

3.3.1 Floating Zero Point Correction

The GOODS-N optimal seeing and optimal depth mosaics created in Ashcraft et al. (2018) were found to have slight differences in their photometric zero points. While these differences were small, ~ 0.2 mag, an additional step was added to the seeing sorted stacking method in order to correct for this offset, which was speculated to be a result of varying transparency and sky brightness atop Mt. Graham (Taylor et al., 2004; Ashcraft et al., 2018). In order to address this slight offset, we investigated the relative transparency of each of the 532 exposures and corrected for any offset in the zero points following the procedures described in Otteson et al. (2021), Redshaw et al. (2022) and Ashcraft et al. (2023). For each individual exposure, a subset of ~ 150 unsaturated stars was selected from a Sloan Digital Sky Survey (SDSS) Data Release 16 (Blanton et al., 2017; Ahumada et al., 2020) based catalog of stars with U -band magnitudes, $18 \leq u \leq 22$ mag. The flux of these unsaturated stars was calculated and compared to the flux from the same sources in a single LBT exposure. The 3σ

clipped median value of the flux ratios for all ~ 150 stars was adopted as the relative atmospheric transparency value for a single exposure.

Figure 12 shows the relative transparency values for each exposure taken on January 26, 2020. This distribution shows a median atmospheric transparency of $\sim 96\%$. While this night's atmospheric transparency differed from the SDSS catalog by only a few percent, this difference in atmospheric throughput is compounded when stacking hundreds of individual exposures. Therefore, a correction was applied to each exposure so that the atmospheric transparency, and thus the photometric zero point, was equal to that of SDSS. After this correction, the transparency for each exposure will be at unity in Figure 12. This process was repeated for each of the 532 exposures in our dataset.

3.3.2 Seeing Sorted Stacks

For all 532 exposures, the individual LBC tiles were combined using SWARP (Bertin et al., 2002; Bertin & Amorisco, 2010), so that SExtractor (Bertin & Arnouts, 1996) could be used to measure the Gaussian FWHM of ~ 100 unsaturated stars in the image. The median of the FWHM distribution for the subset of unsaturated stars was used as the seeing of the entire exposure. The seeing was compared to the tabulated value from the data reduction pipeline, and since they were in agreement, the pipeline FWHM was used for each image. Once the seeing of each image was determined, the 532 observations were sorted as a function of seeing as shown in Figure 13. The median seeing value was determined to be $\sim 1.2''$ FWHM, which is slightly higher than the value of $\sim 1.1''$ FWHM, reported by Ashcraft et al. (2018) for

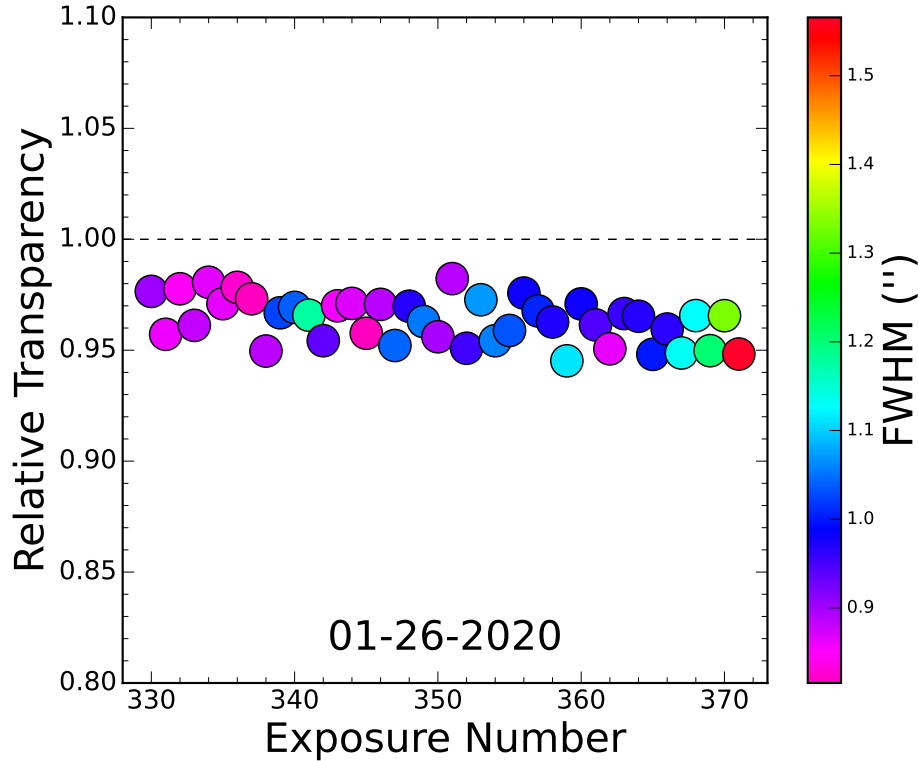


Figure 12. Relative transparency distributions for one night of data in January 2020. The color bar represents the median seeing for each observation and the black, dashed line represents an atmospheric transparency equal to that of SDSS.

the GOODS-N field. However, this still warranted creating separate optimal depth and optimal resolution stacks.

The COSMOS data were combined into two stacks with seeing less than $0.9''$ FWHM (optimal resolution) and seeing less than $1.9''$ FWHM (optimal depth). SWARP was used to perform the image stacking using 5σ clipping and LANCZOS3 resampling on datasets of 67 and 482 images for the optimal resolution and depth mosaics respectively. An example of the two stacks is shown in Figure 14, where the left panel is the optimal resolution and the middle panel is the optimal depth mosaic. In the best depth stack, the low surface brightness tidal tail of the central galaxy is more prominent, while the individual spiral arms and star forming regions can be best

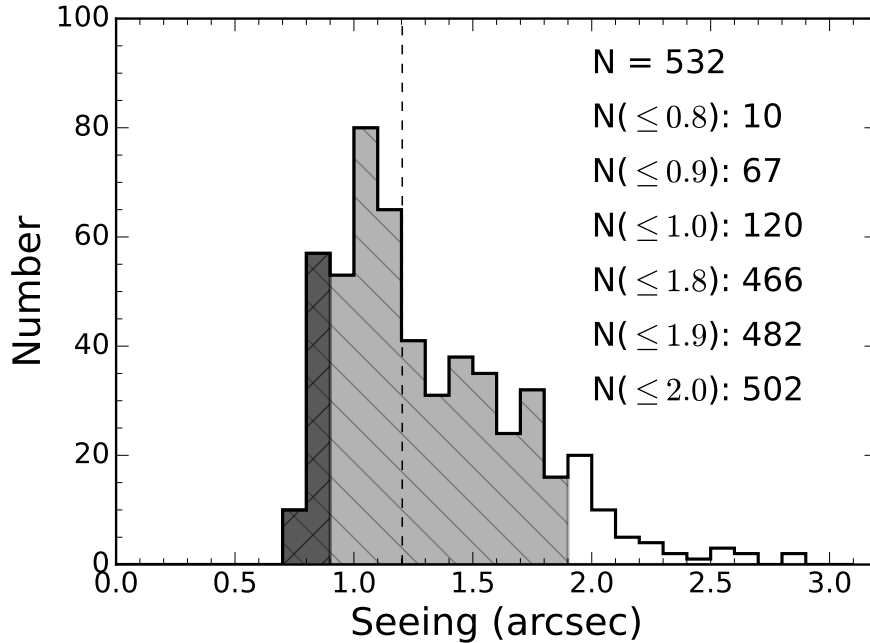


Figure 13. Histogram of the FWHM measurements for each of the 532 usable, individual exposures in the COSMOS field. The vertical, dotted line represents the median seeing (1.2" FWHM) of the dataset. The dark and light shaded regions represent the subset of exposures used for the optimal resolution and optimal depth mosaics, respectively.

discerned in the optimal resolution stack. The necessity of both stacks is highlighted through smoothing the optimal resolution stack to the seeing of the optimal depth stack, where the faint tidal tail is not detected to the level of the optimal depth mosaic.

3.3.3 *U*-band Catalogs

Once the optimal depth and optimal resolution mosaics were created, catalogs were constructed for all of the sources in the mosaics. The catalogs were created using SExtractor and configuration parameters similar to those used in (Ashcraft et al.,

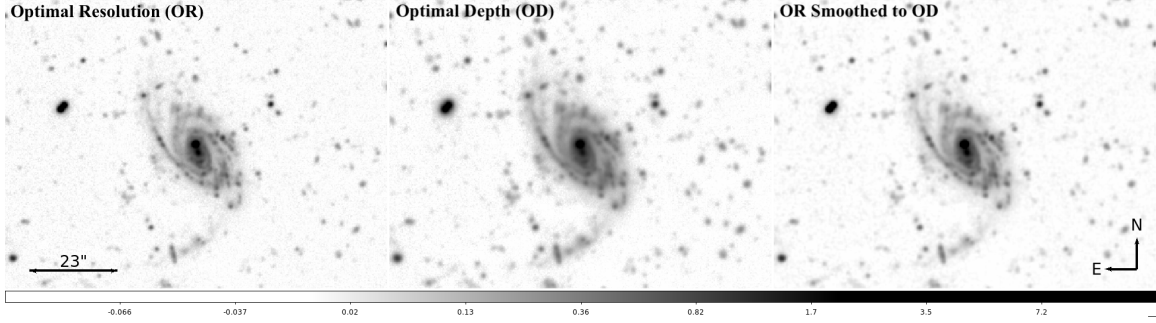


Figure 14. Comparison of a $\sim 100'' \times 75''$ subsection of the optimal resolution (left) and optimal depth (middle) mosaics for the LBT/LBC data. The best seeing stack is composed of 67 individual exposures with $\text{FWHM} \leq 0.9''$, while the optimal depth mosaic is created from a stack of 482 image with $\text{FWHM} \leq 1.9''$. The right panel shows the optimal resolution mosaic smoothed to the seeing of the optimal depth mosaic. Despite being smoothed, this cutout does not capture the low surface brightness flux that is observed with the optimal depth mosaic, which reinforces the need for both optimal resolution and depth stacks.

2018). The sky background was determined through the use of a 6×6 pixel median filter and a 256×256 pixel and 128×128 pixel mesh for the optimal resolution and depth mosaics, respectively. The sources were detected using a Gaussian filter and a 5×5 pixel convolution kernel with a FWHM of 3 pixels.

The photometric zero point was verified to be 26.50 ± 0.11 mag and 26.45 ± 0.11 mag for the optimal resolution and optimal depth mosaics, respectively, by comparing with the photometry of stars between $U_{AB} = 18$ mag and $U_{AB} = 22$ mag within the SDSS catalog. The consistency of these zero points reflects the improvement that was made through the use of the atmospheric transparency corrections.

In order to identify the stars in the source catalog, all sources were placed on a magnitude vs. FWHM diagram, shown in Figure 15, where the non-saturated stars occupy a vertical strip at $\text{FWHM} \sim 1.2''$, the U -band median seeing of the dataset. Saturated stars are also easily identified through the “curled” tip of the vertical strip of stars. To the right of $1.4''$ FWHM, one finds the galaxies identified in the optimal depth

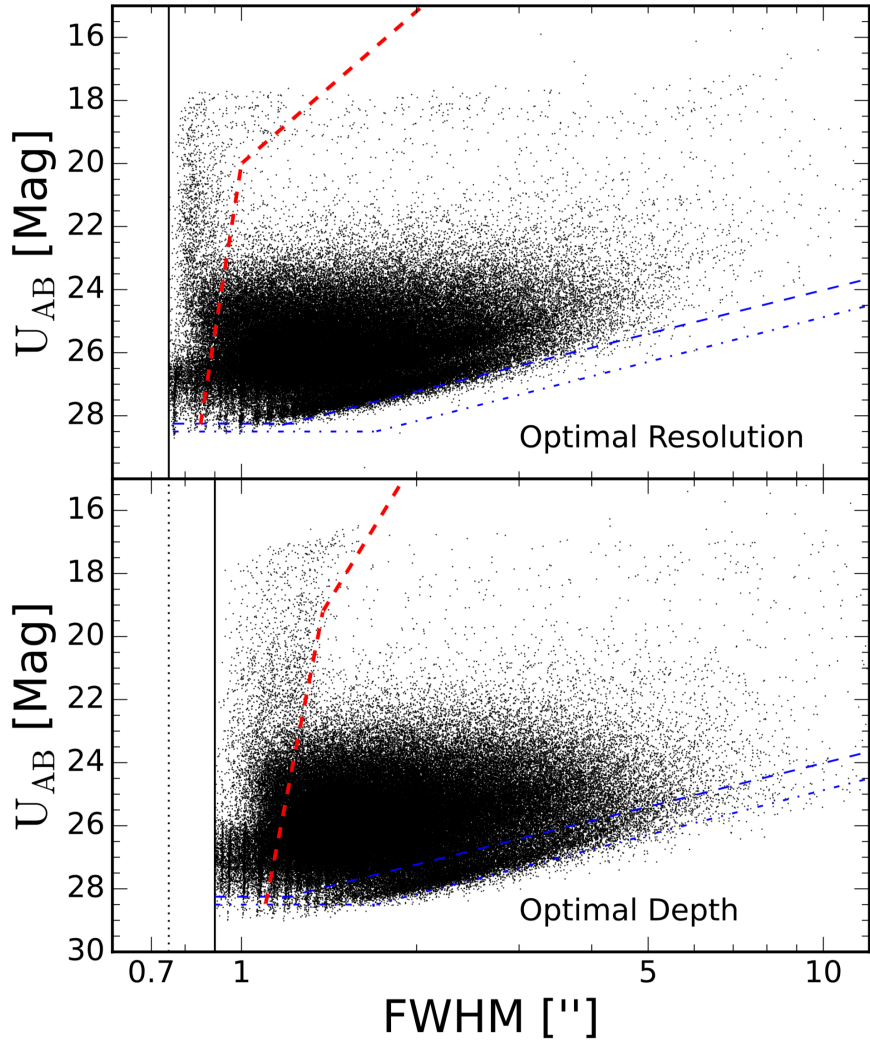


Figure 15. Object FWHM as a function of U-band magnitude for the optimal resolution and optimal depth mosaics. The red, dashed lines show the star/galaxy separation and the solid, black lines illustrate the lower FWHM limits. The blue, dashed and dot-dashed lines represent the surface brightness limits for the optimal resolution and depth mosaics, respectively.

stack. Knowing how stars and galaxies populate different regions of the magnitude vs. FWHM-size diagram allows one to construct separate differential number counts for stars and galaxies.

Typically, the magnitude vs. seeing distribution for a single LBT/LBC pointing

should show a much narrower vertical strip of unsaturated stars along with the same “curled” region for saturated stars. However, due to the large area of the COSMOS field on the sky, it takes four LBC pointings to cover the entire field. Prior to UVCANDELS, there was no high priority region within the field for deep HST observations (see Figure 11), and early LBT observations were spread over the entire two square degree field and on nights with different seeing conditions.

The non-uniform coverage causes the depth to vary as a function of position within the COSMOS field. Figure 16 shows the non-uniform coverage of the LBT COSMOS dataset for the optimal resolution (left) and the best depth (right) mosaics. We achieved a total exposure time of ~ 5 hours and ~ 37 hours for the optimal resolution and depth mosaics, respectively. For comparison, Ashcraft et al. (2018) achieved total exposure times of 3.2 hours and 30.7 hours for their $0.8''$ and $1.8''$ FWHM stacks in the GOODS-N field.

As a result of the uneven coverage across the COSMOS field, we divided the two mosaics into three regions (shallow, medium, and deep) based on total exposure time per pixel. These regions were selected to maximize coverage of each region, while also maintaining connected areas for each region. Table 3 details the three analysis regions for each mosaic and defines the exposure time cutoffs for each as well as the total area. These sub-catalogs allowed for number counts to be created for areas of the full field with approximate equal depth.

Differential galaxy counts were created after separating the stars and galaxies following the prescriptions of Windhorst et al. (2011). These galaxy counts, shown in Figure 17, show that the optimal resolution and optimal depth stacks reach U-band magnitudes of $U \sim 26$ and $U \sim 26.5$ mag respectively. The depths reached in these

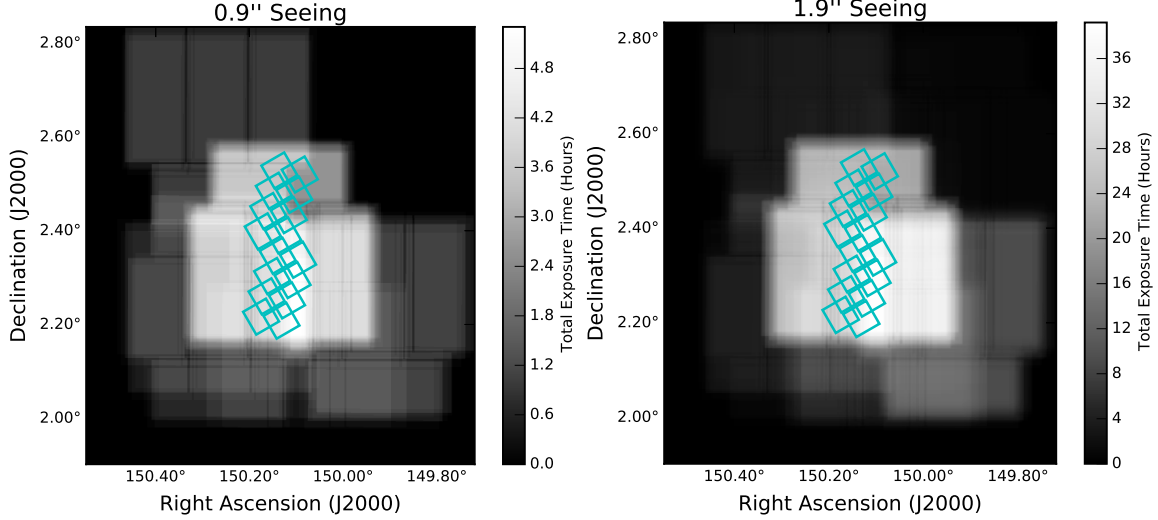


Figure 16. LBC exposure maps showing the total integration time per area on the COSMOS field. The left panel shows the optimal resolution mosaic and the right shows the optimal depth mosaic. The UVCANDELS *HST*/ACS footprint is represented by the cyan boxes. Note that the greyscale represents different exposure times in each panel.

Table 3. Zone definitions for non-uniform LBT coverage of COSMOS

| Regions | Exposure Time (hr) | Area (sq. deg) |
|--------------------|--------------------|----------------|
| Optimal Resolution | | |
| Shallow | 1-2 | 0.206 |
| Medium | 2-4.2 | 0.101 |
| Deep | >4.2 | 0.020 |
| Optimal Depth | | |
| Shallow | 10-24 | 0.205 |
| Medium | 24-32 | 0.050 |
| Deep | >32 | 0.010 |

mosaics are comparable to Ashcraft et al. (2018) (26 mag across GOODS-N) as well as the CFHT Large Area *U*-band Survey (CLAUDS; Sawicki et al., 2019), which reached a depth of 26.3 mag over an area of ~ 4 square degrees in the COSMOS field.

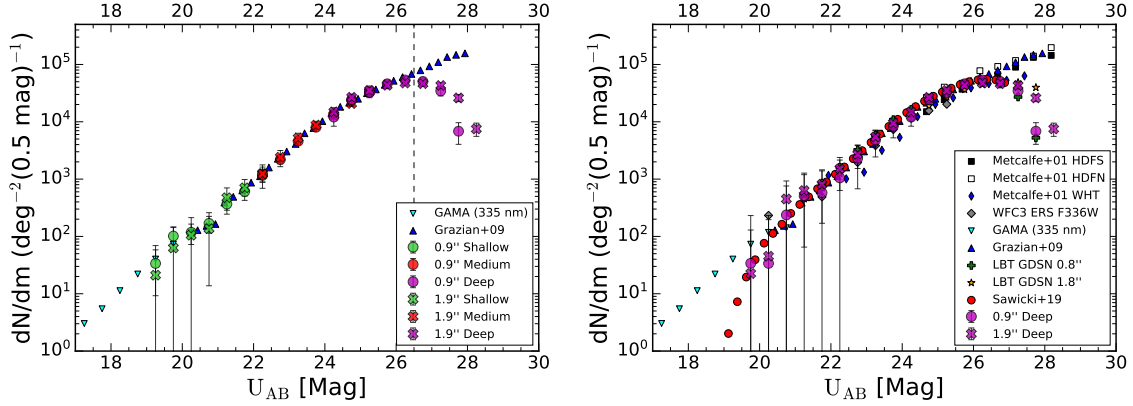


Figure 17. *Left:* Differential galaxy counts for the optimal resolution and optimal depth mosaics. The green, red, and magenta colors represent the shallow, medium, and deep regions, respectively. The vertical, dashed line represents the completeness limit of ~ 26.5 mag as the COSMOS counts begin to significantly deviate from the power law determined by the completeness corrected data from Grazian et al. (2009). *Right:* The optimal depth and resolution galaxy counts in COSMOS compared to the counts in GOODS-N from Ashcraft et al. (2018) as well as various studies in other fields by Metcalfe et al. (2001), Driver et al. (2009), Grazian et al. (2009), Windhorst et al. (2011), and Sawicki et al. (2019). The bright end of the COSMOS number counts deviate from the larger GAMA fields due to the selection against bright stars/galaxies in the definition of the Deep COSMOS field (Koekemoer et al., 2007; Scoville et al., 2007).

3.4 Searching for Intragroup U-band Light

In order to search for diffuse light from the IGrM, we used the optimal depth mosaic in conjunction with the zCOSMOS 20k galaxy group catalog (Knobel et al., 2012). As such light is expected to be too faint to detect in individual groups, we aim to search for IGrL in a composite of multiple groups using image stacking. Three redshift ranges were selected for group stacking, each with increasing redshift and sample size: $0.1 < z \leq 0.2$ ($N=17$), $0.15 < z \leq 0.25$ ($N=27$) and $0.25 < z \leq 0.35$ ($N=33$). We use all groups that are fully contained within the LBC mosaic, excluding groups in regions of the mosaic where the exposure map has a strong gradient which resulted in a

varying background. Furthermore, only groups with $N > 3$ spectroscopically confirmed group members were included to minimize the probability that an included group is only a chance superposition and not a physical group. These redshift slices were specifically selected to increase the number of groups per stack while also retaining enough area per group to perform the rescaling and stacking processes.

As a sample, these groups do not have any bias towards those which are evolved or have experienced recent interactions. Upon visual inspection, these groups do not appear to be dominated by galaxy mergers or interactions. Figure 18 shows the halo mass (left) and group radii (right) distributions for each of the three redshift subsets of our group sample. On average, these groups are more representative of loose groups compared to the more commonly studied compact groups. The halo mass range of this sample of groups is typically between 0.5–1 dex from the loose groups used by Coenda et al. (2012) to study the different galaxy populations in loose and compact groups. Conversely, the group radii in this sample are typically 3–4 times as large as the radii for HCGs studied in (Poliakov et al., 2021).

Within each redshift range, four different stacks were constructed with two stacks corresponding to observed groups from the Knobel et al. (2012) catalog and the other two being random areas for a control sample. The random stack was created to mimic the observed group distributions as closely as possible, while existing at random positions within the optimal depth U-band mosaic. The random “group” redshifts and radii were randomly selected (without replacement) from the true group sample in order to preserve their inherent distributions.

For each of the observed and random groups, each pixel area was rescaled by one of two methods: fractional or physical. The fractional stack was created by rescaling each group so that every group was the same number of pixels across. This allowed for

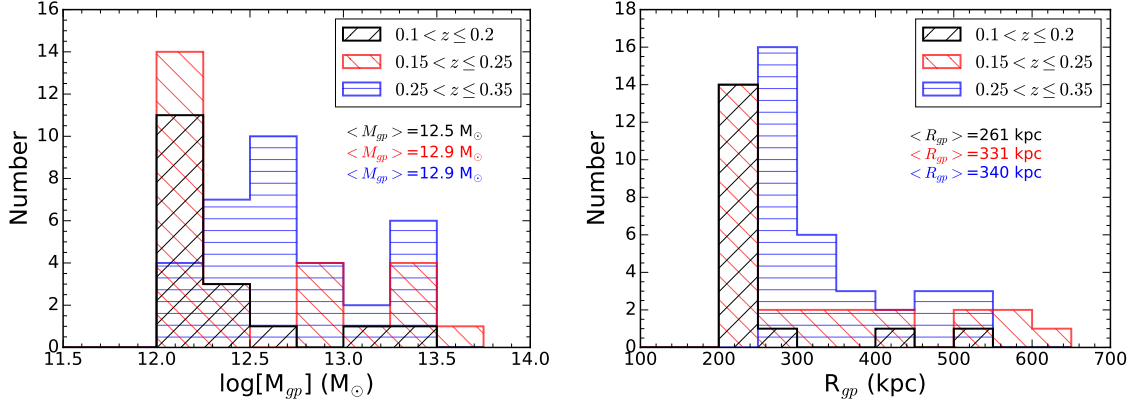


Figure 18. Halo mass (left) and radii (right) distributions for each of the three subsets of groups in the sample. For reference, the average group radius for the lowest redshift bin has an average halo mass and radius which is in line with estimates for the Leo group (Watkins et al., 2014) and the average group radii are 3–4 times as large as typical HCGs (Poliakov et al., 2021). This indicates that this sample probes loose groups, which are expected to be more common compared to more dense compact groups (Coenda et al., 2012, and references therein).

each group’s radius to be aligned such that corresponding fractional radii are stacked together. The physical stack was created by rescaling each group so that each group had the same physical size per pixel given their angular size distance, which allowed the same physical distance in each pixel to be stacked. In both cases, each group was rescaled using Lanczos resampling, such that resolution was always decreased and existing pixels were not split to increase resolution. Care was taken to ensure that flux was conserved between the original and rescaled group cutouts.

For each of the 12 stacks, the stacking process is described as follows:

1. Group cutouts four group radii ($4R_{gp}$) in size on each side were created from the optimal depth mosaic.
2. Each group was rescaled via the fractional or physical methods to match the lowest resolution group in the sample.

3. Source Extractor was run on each cutout to generate segmentation maps, which were used to remove all sources to a level of 0.5σ above the background.
4. Due to slight gradients in the cutout backgrounds, the Source Extractor background map was fit with a plane and then subtracted from the group cutout. These gradients were measured over areas larger than the group sizes, which ensures that faint flux contributing to the IGrL was not subtracted from each group.
5. Each group was then tested for overlap with other groups in the sample. Any overlap was masked out (given zero weight) and not included in the stack.
6. Lastly, the remaining group background was coadded together for each group in the sample with equal weight.

The group stacking results are summarized in Tables 4 and 5 and an example stack is shown in Figure 19 for the medium redshift stack. Across each stack, there was no IGrL detection as each appeared as random noise. For each of the observed group stacks, the rms of the stack was used to calculate a 3σ IGrL upper limit to average surface brightness levels of $\sim 29.1 - 29.6 \text{ mag arcsec}^{-2}$. A bootstrap analysis with replacement was used to determine the uncertainties in each IGrL upper limit. No significant difference was found between the observed and random group stacks, further reinforcing these IGrL non-detections in the observed U-band. There was also no significant difference found between stacking algorithms as the fractional and physical stacks resulted in similar surface brightness limits on the IGrL.

Placing this amount of light into a different context, we can determine approximately how many O and B type stars are required to account for this UV light. By using the median redshift of the stack, the fraction of the blackbody flux from

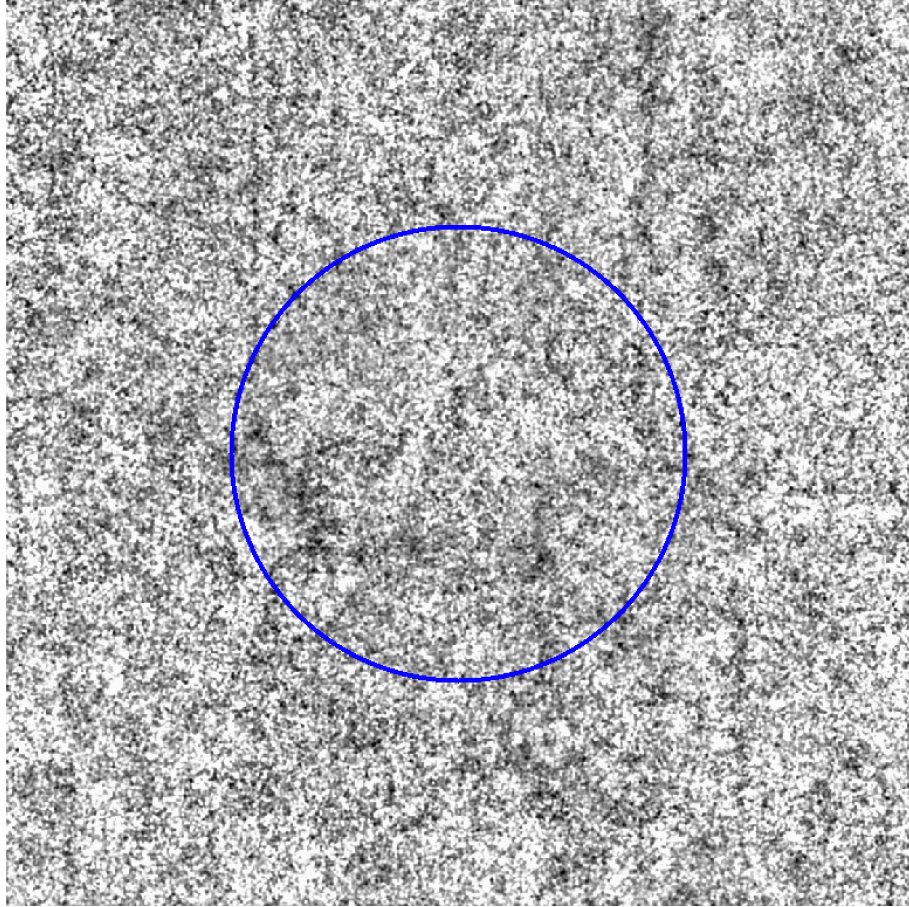


Figure 19. Example of a group stack with 27 groups between redshifts $0.15 < z \leq 0.25$. This stack was rescaled via the fractional method, where the blue circle represents the group radius for each group in the stack. There is no IGrL detected in this stack, which corresponds to a 3σ upper limit of $29.17_{+0.49}^{-0.33} \text{ mag arcsec}^{-2}$.

O/B stars ($> 3 M_{\odot}$) observed by the LBT U_{spec} filter was determined. Then, by calculating the total IGrL luminosity, the number of O/B stars able to contribute towards the group light can be calculated assuming a Salpeter initial mass function (Salpeter, 1955). We find that at most, $\lesssim 3,100$ O/B type stars (or ~ 0.02 O/B stars per kpc^2 across the group’s projected area) are sufficient to account for the IGrL upper limits for the low redshift group stack, which indicates that minimal star formation is occurring outside of member galaxies in groups.

The physical stacking method allows for the amount of IGrL to be determined within the central 50 and 100 kpc of each group. We find no significant difference between the IGrL upper limit within the inner 50 kpc vs the inner 100 kpc. This either indicates that there is no additional IGrL outside of the central 50 kpc of groups on average, or that an IGrL profile may exist but at levels too faint to be detected with these stacks.

3.5 Discussion and Summary

Here, we summarize and discuss the main results of this study:

1. We used 25 partial nights with the LBT/LBC between 2007 and 2020 to observe the COSMOS field in the U -band and create optimal resolution and optimal depth mosaics totaling up to ~ 37 hours. Following the seeing sorted stacking process detailed in Ashcraft et al. (2018), Otteson et al. (2021), Redshaw et al. (2022) and Ashcraft et al. (2023), the seeing of each individual exposure was calculated through the median FWHM of ~ 100 unsaturated stars. Prior to creating the optimal resolution (FWHM $\leq 0.9''$) and optimal depth (FWHM $\leq 1.9''$) mosaics, the relative atmospheric transparency was corrected for each

exposure. Ashcraft et al. (2018) noted a ~ 0.2 mag difference in photometric zero point between the GOODS-N optimal resolution and depth mosaics, which was attributed to variable atmospheric conditions on Mt. Graham (Taylor et al., 2004). However, by correcting for the relative atmospheric transparency differences from exposure to exposure, the difference in photometric zero point was reduced to ~ 0.05 mag. The optimal resolution and optimal depth mosaics reached 3σ depths of ~ 26 and ~ 26.5 mag, respectively, which are comparable to other U-band surveys (Ashcraft et al., 2018; Sawicki et al., 2019; Otteson et al., 2021; Redshaw et al., 2022)

2. Using the optimal depth mosaic in addition to the Knobel et al. (2012) zCOSMOS 20k group catalog, we searched for signatures of IGrL by masking out known sources and only stacking the group backgrounds. We created stacks over three redshift ranges ($0.1 < z \leq 0.2$ (N=17), $0.15 < z \leq 0.25$ (N=27) and $0.25 < z \leq 0.35$ (N=33)) in an effort to trace diffuse UV light in the group environment using two different stacking methods. The fractional stacking method rescaled each group such that each group’s radius extended across the same number of pixels, which allowed the IGrL to be probed as a function of group radius. On the other hand, the physical stacking method rescaled each group such that each pixel represented the same size (kpc/pix) across each group.

3. We find 3σ upper limits for the amount of UV IGrL down to ~ 29.1 – 29.6 mag arcsec $^{-2}$ for each group stack, which corresponds to $\lesssim 1\%$ of the total group light. Figure 20 shows the IGrL upper limits measured in this study compared to published values of HCGs (Da Rocha & Mendes de Oliveira, 2005; Aguerri et al., 2006; Da Rocha et al., 2008; Poliakov et al., 2021) and

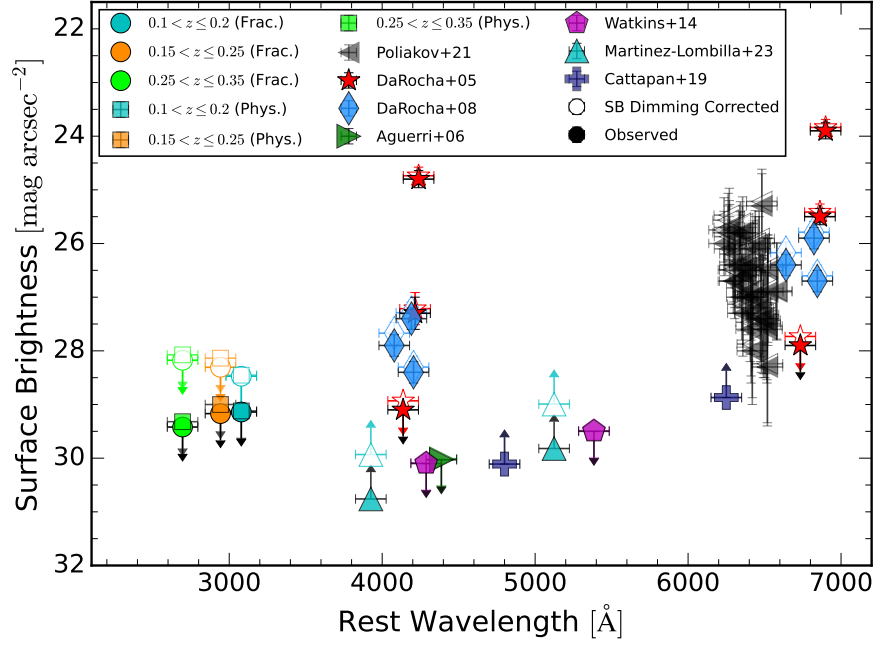


Figure 20. IGrL surface brightness measurements as a function of rest frame wavelength for the stacks presented in this work as well as other studies of HCGs (Da Rocha & Mendes de Oliveira, 2005; Aguerri et al., 2006; Da Rocha et al., 2008; Poliakov et al., 2021), the Leo group (Watkins et al., 2014), and other loose groups (Cattapan et al., 2019; Martínez-Lombilla et al., 2023). The points corresponding to Cattapan et al. (2019) and Martínez-Lombilla et al. (2023) were drawn as lower limits to denote that their measurements represented the limiting surface brightness of the outer regions of their IGrL detections. The filled in data points represent the observed IGrL surface brightness, while the outlined points are corrected for the effects of surface brightness dimming. On average, the IGrL detection rate appears to decline as rest frame wavelength shifts bluer, which indicates that the IGrL may not exhibit a strong contribution from young stars.

from the Leo group (Watkins et al., 2014). In particular, each of our upper limits are relatively consistent with the IGrL upper limits in HGCs 44 (Aguerri et al., 2006), 88 (Da Rocha & Mendes de Oliveira, 2005), and the Leo group (Watkins et al., 2014), albeit at higher redshift and in the rest frame UV. On average, the IGrL appears brighter at longer wavelengths, which may indicate that young stars do not contribute significantly to the IGrL and that minimal in-situ star formation occurs in the IGrL. This would favor tidal stripping and galaxy interactions as the primary method for the formation and buildup of IGrL as proposed by Da Rocha & Mendes de Oliveira (2005); Aguerri et al. (2006) and Poliakov et al. (2021) for compact groups and Spavone et al. (2018); Cattapan et al. (2019); Raj et al. (2020) and Martínez-Lombilla et al. (2023) for loose groups.

4. Despite past observations of the presence of significant amounts of atomic gas in the IGrM (Verdes-Montenegro et al., 2001; Borthakur et al., 2010a; Pisano et al., 2011; Borthakur et al., 2015a; Cluver et al., 2016; Borthakur et al., 2019a; Džudžar et al., 2019; McCabe et al., 2021; Roychowdhury et al., 2022), we do not observe strong signatures of recent star formation. The lack of UV IGrL detected in this study suggests that the atomic gas structures in the IGrM are likely not dense enough to trigger large scale star formation.

Lastly, we discuss our main findings in context of other published works. Previous studies of IGrL in HCGs by Da Rocha & Mendes de Oliveira (2005), Aguerri et al. (2006) and Poliakov et al. (2021) constructed a picture where galaxy interactions and tidal stripping remove stars and gas from group members, which eventually settle towards the dominant gravitational potential. In this model, only the most dynamically evolved groups have experienced enough crossing times and interactions

necessary for the build up of IGrL. This hypothesis is reinforced by studies of loose groups where IGrL detections were observed to be a direct result of gravitational interactions between group members (Spavone et al., 2018; Cattapan et al., 2019; Raj et al., 2020; Martínez-Lombilla et al., 2023).

In addition, new models and observations by Kolcu et al. (2022) show that, while not as common as in cluster environments, ram pressure stripping is still prevalent in groups. This process was determined to be most consistent with recent infalling galaxies, which may remove cold gas from the infalling member. If this stripped gas is able to fuel star formation, there may be a pathway for IGrL to have a strong contribution from young stars. However, the lack of a UV IGrL detection in our analysis favors tidal interactions over ram pressure stripping as the dominant means for the build up of IGrL.

The role of active galactic nuclei (AGN) in group environments could also drastically influence the amount of IGrL. Cui et al. (2014) used simulated galaxy clusters and found evidence that AGN activity is able to alter the fraction of diffuse, stellar light by up to a factor of 2. AGN feedback may prevent star formation in the central regions of galaxy groups due to the sheer amount of energy returned to the IGrM (McNamara & Nulsen, 2007; Gitti et al., 2012; Heckman & Best, 2014; Gaspari et al., 2020; Eckert et al., 2021, and references therein). If this is the case, it might explain the lack of star formation in the IGrM and the corresponding faint limits to the U-band IGrL in this study.

Comparing these IGrL properties to intracluster light (ICL), we find similarities in terms of possible formation processes. The main theories for the buildup of ICL are any of the following (or a combination thereof): tidal stripping (Rudick et al., 2009), the ejection of stars from galaxy mergers (Willman et al., 2004; Murante et al.,

2007), and the accretion of galaxy groups (Mihos, 2004; Rudick et al., 2006). However, Montes (2022, and references therein) note that studying the ICL through stellar populations may only unveil the dominant formation process of a particular cluster and not a combination of mechanisms which may vary from cluster to cluster. For the Virgo and Coma clusters, Williams et al. (2007) and Coccato et al. (2010, and references therein) find that the ICL is primarily composed of older stars, which align with our conclusions of minimal star formation in groups that could contribute to IGrL. However, Jiménez-Teja & Dupke (2016) find an increased amount of ICL in the rest frame B-band for Abell 2744, which is indicative of a younger population of stars that may have formed during merging events. Given the large amounts of atomic gas known to exist in groups (Verdes-Montenegro et al., 2001; Borthakur et al., 2010a; Pisano et al., 2011; Borthakur et al., 2015a; Cluver et al., 2016; Borthakur et al., 2019a; Džudžar et al., 2019; McCabe et al., 2021; Roychowdhury et al., 2022), merging groups may be a potential environment to search for star formation in the IGrM traced by U-band IGrL.

Future studies may be able to determine the dependence of IGrL on both wavelength and dynamical evolution. The majority of the studies shown in Figure 20 represent studies of HCGs, which are ideal environments for galaxy interactions. Observations of a wider range of group environments could provide insight into the build up of IGrL through galaxy interactions and/or tidal stripping. In Ashcraft et al. (2023), evidence of additional diffuse light in the outskirts of galaxies was detected in the r -band resulting from tidal tails and galaxy interactions. These signs of interactions have also been abundantly observed with JWST (Finkelstein et al., 2022; Windhorst et al., 2023, and references therein). Additionally, filling in the wavelength gaps in Figure 20 may help place constraints on the stellar populations contributing to IGrL.

Finally, increasing the number of publicly available galaxy group catalogs in popular survey fields would be beneficial to the study of IGrL. Similar group stacks could be created in other survey fields where deep, multi-wavelength data already exists. Moreover, more group catalogs would aid in other studies using QSO absorption lines to probe diffuse gas in group environments. The combination of IGrM studies in absorption and emission via IGrL are necessary in order to fully understand the impact that group environments have on galaxy evolution.

Table 4. Fractional Group Stack Measurements

| Stack Type | Redshift Range | z_{med} | Number Groups | Mag | $N_*(> 3M_{\odot})$ | $\Sigma_*(> 3M_{\odot})$ | $\mu_U^{A,B}$ | Excess over Random |
|------------|----------------------|------------------|---------------|-----------|----------------------|---------------------------|---------------------------|--------------------|
| (1) | (2) | (3) | (4) | (5) | (6) | (7) | (8) | (9) |
| Observed | $0.1 < z \leq 0.2$ | 0.166 | 17 | > 32.39 | $< 3,100$ | < 0.02 | $> 29.14_{-0.24}^{+0.32}$ | -25.5% |
| Observed | $0.15 < z \leq 0.25$ | 0.220 | 27 | > 32.42 | $< 5,500$ | < 0.03 | $> 29.17_{-0.33}^{+0.49}$ | 18.0% |
| Observed | $0.25 < z \leq 0.35$ | 0.332 | 33 | > 32.67 | $< 11,000$ | < 0.03 | $> 29.42_{-0.22}^{+0.28}$ | 18.0% |
| Random | $0.1 < z \leq 0.2$ | 0.166 | 17 | > 32.07 | $< 4,100$ | < 0.02 | $> 28.82_{-0.21}^{+0.26}$ | - |
| Random | $0.15 < z \leq 0.25$ | 0.220 | 27 | > 32.60 | $< 4,600$ | < 0.02 | $> 29.35_{-0.24}^{+0.30}$ | - |
| Random | $0.25 < z \leq 0.35$ | 0.332 | 33 | > 32.85 | $< 9,300$ | < 0.03 | $> 29.60_{-0.25}^{+0.33}$ | - |

NOTE—Column (5) is the total magnitude corresponding to all of the light within the group. Column (6) represents the equivalent number of stars greater than 3 solar masses (O and B type stars) which would primarily contribute to the UV IGrL (if detected) at the surface brightness limit. Column (7) represents the number of O/B stars per square kpc - assuming the median R_{gp} of the groups in the stack. Column (8) is in units of mag arcsec^{-2} . We utilize a bootstrap analysis with replacement for the uncertainty in the SB upper limit.

Table 5. Physical Group Stack Measurements

| Stack Type | Redshift Range | z_{med} | Number Groups | Mag _{50kpc} | Mag _{100kpc} | μ_U^{AB} | Excess over Random |
|------------|----------------------|------------------|---------------|----------------------|-----------------------|---------------------------|--------------------|
| (1) | (2) | (3) | (4) | (5) | (6) | (7) | (8) |
| Observed | $0.1 < z \leq 0.2$ | 0.166 | 17 | > 32.37 | > 32.39 | $> 29.12_{-0.28}^{+0.37}$ | -28.2% |
| Observed | $0.15 < z \leq 0.25$ | 0.220 | 27 | > 32.26 | > 32.27 | $> 29.00_{-0.29}^{+0.39}$ | 27.1% |
| Observed | $0.25 < z \leq 0.35$ | 0.332 | 33 | > 32.57 | > 32.58 | $> 29.32_{-0.21}^{+0.26}$ | 25.9% |
| Random | $0.1 < z \leq 0.2$ | 0.166 | 17 | > 32.01 | > 32.00 | $> 28.76_{-0.39}^{+0.63}$ | - |
| Random | $0.15 < z \leq 0.25$ | 0.220 | 27 | > 32.50 | > 32.47 | $> 29.26_{-0.29}^{+0.40}$ | - |
| Random | $0.25 < z \leq 0.35$ | 0.332 | 33 | > 32.82 | > 32.79 | $> 29.57_{-0.24}^{+0.31}$ | - |

NOTE—Columns (5) and (6) are the total magnitudes corresponding to all of the light within the central 50 or 100 kpc. Column (7) is in units of mag arcsec^{-2} . We utilize a bootstrap analysis with replacement for the uncertainty in the SB upper limit.

DETECTION OF A MULTIPHASE INTRAGROUP MEDIUM: RESULTS FROM
THE COS-IGRM SURVEY

4.1 Introduction

⁶The majority of galaxies in the Universe exist in groups, where the dark matter halos cover mass ranges of $10^{12} \lesssim M_{halo} \lesssim 10^{14.5} M_{\odot}$ (Tully, 1987). The diffuse, hot gas gravitationally bound to the group is commonly referred to as the intragroup medium (IGrM) and may constitute a significant entry into the missing baryon problem (Persic & Salucci, 1992; Fukugita & Peebles, 2006; Spergel et al., 2007). The effect on galaxy evolution of the IGrM and the halos of groups remains uncertain. The gas in galaxy group halos can be characterized through X-rays, the Sunyaev-Zel’dovich (SZ) effect, and through UV absorption lines from background quasars (QSOs).

Early IGrM detections were based on *ROSAT* observations of high mass, elliptical rich groups (Mulchaey et al., 1996a; Helsdon & Ponman, 2000b; Mulchaey, 2000). These groups were believed to be more massive than spiral rich groups and hence more luminous in X-rays. From these observations, initial scaling relations (Helsdon & Ponman, 2000b) were derived and the mass of the hot gas was determined to be comparable to the stellar mass of the galaxies (Mulchaey et al., 1996a). More recently, Bregman & Lloyd-Davies (2007) studied O VII absorption to distinguish its origin as from the Milky Way’s galactic halo or from the Local Group’s IGrM. In searching for the IGrM, they found that the Milky Way halo models were preferred, but a

⁶This chapter is published as McCabe et al. (2021)

contribution to the O VII absorption from the IGrM could not be conclusively ruled out.

The thermal SZ effect, where cosmic microwave background (CMB) photons are scattered as a result of energetic, free electrons, provides an alternative means of observing the diffuse gas bound to dark matter halos. While the SZ effect is typically used to analyze galaxy clusters, recent studies using large stacks have led to detections around galaxy groups and individual galaxies (Greco et al., 2015; Vikram et al., 2017; Bregman et al., 2018; Pratt & Bregman, 2020; Tanimura et al., 2020, and references therein). As noted in Le Brun et al. (2015); Tumlinson et al. (2017) and Tanimura et al. (2020), the gas content of galaxy halos down to $10^{11}M_{\odot}$ comes into tension with existing X-ray observations as the self-similar scaling relations appear to fail.

However, Le Brun et al. (2015) proposes that the discrepancy may result from the low resolution of the Planck SZ map and therefore might not be as robust at low radii ($r \lesssim r_{500}$) when compared to X-ray observations. This effect was reproduced using X-ray simulations were convolved with the Planck beam (Le Brun et al., 2015). Cosmological “zoom in” simulations by van de Voort et al. (2016) find that hot gas near the virial temperature causes more consistent X-ray luminosity scaling relations for halos with $M_{halo} \gtrsim 10^{13} M_{\odot}$, while less massive halos show X-ray luminosities that are more strongly affected by star formation feedback.

Ultraviolet (UV) absorption lines observed in the spectra of background QSOs remain one of the most robust methods to probe gas at intermediate temperatures, where the gas is not hot enough for X-ray emission. QSO absorption lines (QALs) have shown that a significant amount of baryons lie in the diffuse gas that makes up the intergalactic medium (IGM) (Rauch, 1998; Shull et al., 2012). This provides means of probing the composition of the IGrM since the large majority of galaxy

groups are lower in mass and do not have the temperature and density necessary for X-ray emission. At the virial temperature of typical galaxy groups, Mulchaey et al. (1996b) predicted the existence of broad, shallow O VI absorption with Lyman series transitions without lower ions such as C IV and N V based upon collisional ionization equilibrium (CIE) models. In this scenario, C IV and N V are present at levels not currently detectable with current instruments such as the Cosmic Origins Spectrograph (COS; Green et al. (2012)) aboard the *Hubble Space Telescope*.

With this background, studies by Tripp et al. (2000); Tripp & Savage (2000) and Stocke et al. (2006) used background quasars to search for O VI, but the data were inconclusive in correlating O VI absorption with the IGrM. Stocke et al. (2014) conducted redshift surveys around 14 previously detected broad Ly α and O VI detections, which were indicative of gas above 10^5 K. They found galaxy groups around these QSO sightlines and concluded with 2σ confidence that these absorbers were due to the group environment and not the nearest galaxy to the sightline. The possibility that the O VI detections were tracing cooler clouds rather than the hot component of the IGrM was still a hypothesis and it lacked any direct observational confirmation. Other O VI studies by Pointon et al. (2017) and Stocke et al. (2017) compared the detections in group environments to the circumgalactic medium (CGM) of isolated galaxies. These studies found that group environments contained O VI absorption that could be modeled with broader components than isolated systems and concluded that O VI was characteristic of the boundary between cooler CGM gas and the hotter IGrM.

Studies by Tripp et al. (2008); Savage et al. (2010, 2012, 2014) and Rosenwasser et al. (2018) detected O VI absorption features that are consistent with multiphase gas at both cooler and hotter temperatures that could be produced by photoionization

or collisional ionization, respectively. However, from these studies, it is difficult to distinguish the origin of O VI as being due to the boundary of multiphase gas in the IGrM or resulting from the CGM of member galaxies. The COS-Halos Survey (Tumlinson et al., 2011, 2013; Peeples et al., 2014; Werk et al., 2014, 2016) analyzed spectra of 44 QSO-galaxy pairs and found O VI in addition to a significant amount of metals in the halos of isolated galaxies. The COS-Halos Survey found a strong correlation of O VI detections in the inner CGM of star forming galaxies leading to the idea that it may originate from large streams of cooling gas or from the hotter component of the CGM if a temperature gradient is assumed as opposed to a uniform halo at the virial temperature (Werk et al., 2014; McQuinn & Werk, 2018).

Heckman et al. (2002) and Bordoloi et al. (2017) (and references therein) show that O VI observed in the intergalactic medium, CGM of galaxies, and the Milky Way halo can be explained by radiative cooling models. These models agree with observations and simulations showing complex, multiphase structures at the interfaces between hot and cold gas (Oppenheimer & Davé, 2009; Churchill et al., 2012; Pachat et al., 2016; Narayanan et al., 2018; Ahoranta et al., 2020).

Recently, Stocke et al. (2019) carried out a survey of 12 galaxy groups paired with background QSOs to look for O VI associated with galaxy groups. They find that O VI was not uniformly detected within the sample, leading to the idea that CGM-like clouds can escape individual galaxies and can be observed within the group. They do not find evidence that these clouds can easily escape the group, which means that galaxy groups might be “closed-boxes” for galaxy evolution. Lastly, they conclude that the gas traced through O VI is not volume filling and that a hotter component is necessary for a complete baryon census in the group environment.

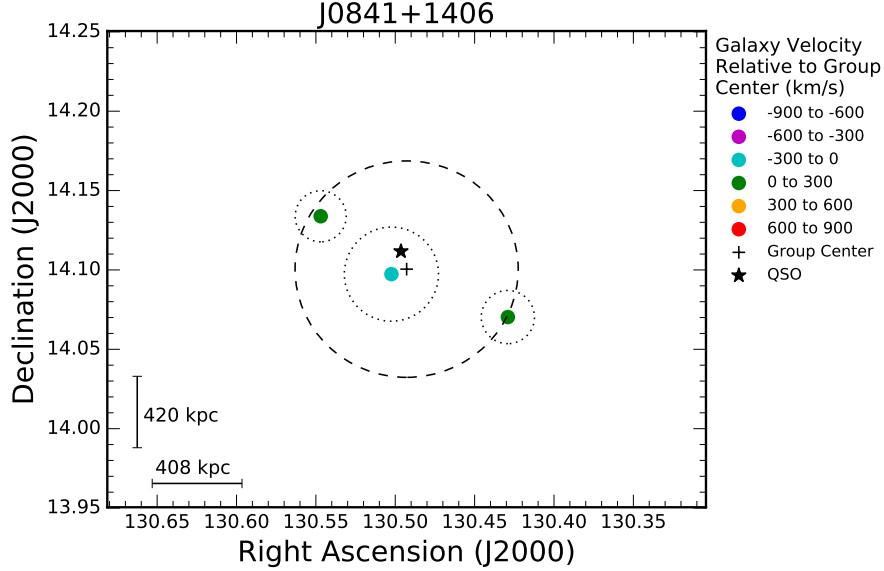


Figure 21. Environment of galaxy group J0841+1406. The color of the points represent the velocity of the member galaxies relative to the center of the group. The thick, dashed line represents the virial radius of the group and the thin, dotted lines represent the virial radii of the member galaxies. The remaining 17 group environments are listed in Appendix A.1

Here we present the COS-IGrM survey, designed to probe the IGrM of lower mass groups than those probed by Stocke et al. (2019), where O VI could be a better tracer of the IGrM due to lower virial temperatures. The COS-IGrM sample consists of 18 galaxy groups paired with background UV bright quasars (QSOs) and was selected without bias towards predefined sightlines with O VI detections. This is the largest sample of low redshift ($z_{gp} \leq 0.2$) galaxy groups ever probed for O VI associated with the IGrM.

This paper is organized as follows: in §4.2 we describe the COS-IGrM sample, §4.3 details the HST/COS observations along with the data reduction and analysis, §4.4

presents the results of the survey, §4.5 discusses the overall significance of our results and §4.6 presents the conclusions of our survey.

4.2 Sample

The COS-IGrM sample is composed of 18 galaxy groups⁷ each with a background QSO with a GALEX far ultraviolet (FUV) magnitude brighter than 19. The sample was created by cross referencing the Tago et al. (2010) galaxy group catalog with the catalog of unique GALEX Data Release 5 QSOs (Bianchi et al., 2011). Four additional criteria were implemented to create a robust sample from the Tago et al. (2010) group catalog:

1. The groups must have at least three spectroscopically confirmed members;
2. The group redshifts must be between $0.075 \leq z_{gp} \leq 0.2$ for O VI to be within the COS bandpass;
3. The QSO redshift, $z_{QSO} > z_{gp} + 0.1$ to eliminate confusion between absorption features from the group and from the QSO;
4. The QSO impact parameter must be less than 1.5 times the group's virial radius ($1.5R_{vir}$).

In order to ensure that the groups in the COS-IGrM sample are physical groups, the Yang et al. (2007) galaxy group catalog was used to look for confirmed groups in the same location and with similar halo mass as provided by the Tago et al. (2010) catalog. This additional check aided in confidently identifying galaxy groups with as little as three spectroscopically confirmed members. The environment of one group in

⁷In the HST proposal, there were 19 sightlines; however, one sightline had an insufficient signal to noise to use for this analysis.

Table 6. COS-IGrM Sample

| Sightline | Group | RA _{gp} | DEC _{gp} | z _{gp} | RA _{qso} | DEC _{qso} | z _{qso} | N _{gp} | σ _{T,sgo} | R _{vir,T,sgo} | ρ _{QSO} | log[M _{halo}] | R _{vir} | σ _{gp} | RA _{cg} | DEC _{cg} | Subset |
|-----------|------------|------------------|-------------------|-----------------|-------------------|--------------------|------------------|-----------------|--------------------|------------------------|------------------|-------------------------|------------------|-----------------|------------------|-------------------|------------|
| (1) | (2) | (3) | (4) | (5) | (6) | (7) | (8) | (9) | (10) | (11) | (12) | (13) | (14) | (15) | (16) | (17) | (18) |
| 1 | J0841+1406 | 130.493 | 14.100 | 0.1250 | 130.496 | 14.112 | 1.2514 | 3 | 81.3 | 638 | 95 | 13.32 | 567 | 229 | 130.502 | 14.097 | CGM + IGrM |
| 2 | J1017+4702 | 154.246 | 47.049 | 0.1637 | 154.379 | 47.040 | 0.3350 | 3 | 91.9 | 710 | 926 | 13.33 | 573 | 232 | 154.302 | 47.025 | IGrM |
| 3 | J1020+1003 | 155.222 | 10.137 | 0.1229 | 155.235 | 10.059 | 0.6074 | 3 | 223.0 | 466 | 632 | 13.19 | 516 | 209 | 155.200 | 10.092 | IGrM |
| 4 | J1025+4808 | 156.286 | 48.110 | 0.1333 | 156.304 | 48.148 | 0.3317 | 4 | 135.7 | 315 | 340 | 13.31 | 564 | 228 | 156.293 | 48.164 | CGM + IGrM |
| 5 | J1102+0521 | 165.676 | 5.296 | 0.1314 | 165.653 | 5.355 | 0.4987 | 4 | 210.1 | 528 | 536 | 13.23 | 532 | 215 | 165.695 | 5.355 | IGrM |
| 6 | J1126+1204 | 171.691 | 12.122 | 0.1640 | 171.637 | 12.077 | 0.9759 | 5 | 76.0 | 686 | 707 | 13.61 | 709 | 287 | 171.641 | 12.094 | CGM + IGrM |
| 7 | J1127+2654 | 171.875 | 26.900 | 0.1521 | 171.902 | 26.914 | 0.3790 | 3 | 89.6 | 492 | 267 | 13.40 | 606 | 245 | 171.904 | 26.904 | CGM + IGrM |
| 8 | J1216+0712 | 184.140 | 7.148 | 0.1360 | 184.169 | 7.207 | 0.5864 | 3 | 242.7 | 404 | 572 | 13.35 | 579 | 234 | 184.161 | 7.174 | IGrM |
| 9 | J1301+2819 | 195.206 | 28.410 | 0.1439 | 195.254 | 28.329 | 1.3597 | 3 | 141.2 | 613 | 836 | 13.33 | 574 | 232 | 195.243 | 28.361 | IGrM |
| 10 | J1339+5355 | 204.814 | 53.990 | 0.1590 | 204.802 | 53.924 | 0.2933 | 4 | 85.1 | 523 | 653 | 13.43 | 620 | 251 | 204.852 | 53.969 | IGrM |
| 11 | J1343+2538 | 206.031 | 25.700 | 0.0749 | 205.986 | 25.647 | 0.0866 | 3 | 43.0 | 291 | 346 | 12.85 | 396 | 160 | 205.975 | 25.675 | IGrM |
| 12 | J1344+5546 | 206.195 | 55.802 | 0.1546 | 206.198 | 55.782 | 0.9369 | 3 | 177.2 | 570 | 194 | 13.44 | 625 | 253 | 206.210 | 55.795 | CGM + IGrM |
| 13 | J1348+4303 | 207.343 | 43.017 | 0.0947 | 207.228 | 43.053 | 0.2748 | 7 | 207.7 | 574 | 580 | 13.60 | 705 | 285 | 207.276 | 43.047 | IGrM |
| 14 | J1408+5657 | 212.222 | 56.911 | 0.1302 | 212.226 | 56.962 | 0.3363 | 3 | 43.2 | 403 | 427 | 13.46 | 632 | 256 | 212.257 | 56.980 | IGrM |
| 15 | J1424+4214 | 216.247 | 42.261 | 0.0995 | 216.231 | 42.235 | 0.3162 | 3 | 46.3 | 459 | 189 | 13.17 | 506 | 205 | 216.219 | 42.251 | CGM + IGrM |
| 16 | J1426+1955 | 216.465 | 19.914 | 0.1091 | 216.555 | 19.924 | 0.2133 | 3 | 111.1 | 594 | 616 | 12.89 | 407 | 165 | 216.504 | 19.867 | IGrM |
| 17 | J1428+3225 | 217.304 | 32.404 | 0.1308 | 217.246 | 32.419 | 0.6270 | 4 | 123.6 | 777 | 433 | 13.32 | 567 | 229 | 217.320 | 32.431 | IGrM |
| 18 | J1617+0854 | 244.430 | 8.913 | 0.0993 | 244.349 | 8.904 | 0.2064 | 6 | 69.3 | 392 | 533 | 13.36 | 585 | 237 | 244.395 | 8.884 | IGrM |

NOTE—Columns (10) and (15) have units of km s⁻¹; Columns (11), (12), and (14) have units of kpc; Column (13) has units of M_⊙. RA_{cg} and DEC_{cg} are the coordinates of the closest member galaxy to the QSO sightline.

our sample is shown in Figure 21 along with the location of the background QSO. The remaining 17 group environments are listed in Appendix A.1. Since galaxy groups were identified from Sloan Digital Sky Survey (SDSS) spectroscopic group catalogs, our sample is biased towards groups with luminous galaxies, $L \gtrsim L_*$.

We also include sightlines from Stocke et al. (2019) in our analysis to extend the sample to larger halo masses. In order to make sample parameters consistent with those from Stocke et al. (2019), we re-defined the group parameters such as the group halo mass, virial radius, and velocity dispersion through the following relations from their paper:

$$M_{gp} = 310 \times \left(\frac{L_{gp}}{L_*} \right) \times 10^{10} M_\odot \quad (4.1)$$

Where L_{gp} is total the r-band luminosity of the group members calculated via the r-band magnitudes from the Tago et al. (2010) catalog.

$$R_{vir} = 957 \times \left(\frac{M_{gp}}{10^{14}} \right)^{1/3} kpc \quad (4.2)$$

and

$$\sigma_{gp} = 387 \times \left(\frac{M_{gp}}{10^{14} M_\odot} \right)^{1/3} kms^{-1} \quad (4.3)$$

In Equation 2, the virial radius is defined as the limit where the overdensity of the medium is equal to $200\rho_{crit}$ as described in Shull et al. (2012) and Stocke et al. (2019). The full properties of our galaxy group sample and each corresponding background QSO are listed in Table 6 along with the adopted values for the halo mass, virial radius, and velocity dispersion.

While each sightline probes the IGrM, some also pass through within the CGM of member galaxies. Therefore, we divide our sample into two sub-samples - one with sightlines passing through the CGM of member galaxies and the other where the

sightline is at impact parameters larger than the viral radius of the member galaxies (assuming an isolated halo). This assumption may over-estimate the size of the CGM of group members; however, it remains the most reliable radius estimate without requiring extensive cosmological simulations. The first group contains six sightlines and are referred to as the CGM + IGrM. The remaining 12 sightlines fall in the latter category. In the absence of a deeper spectroscopic survey, our limiting magnitude allows us to claim that the “pure” IGrM sightlines do not go through the CGM of any $\sim L_*$ galaxies. While it is possible that occasionally a much smaller galaxy could be close to the QSO sightline, care was taken to identify any possible galaxy candidates at the same redshift near the QSO sightline. Statistically, we do not find a significant number of possible member galaxies. This was followed up by recent multi object spectroscopy of two of the fields with the MMT and the Gemini Observatory, which confirmed this result, i.e., very few new galaxies were detected to be part of the groups and none very close to the QSO. These results will be discussed further in a future paper (McCabe et al. in prep). In Table 6, we refer to the sub-grouping for each sightline/group as either IGrM or CGM + IGrM depending on the location of the QSO sightline.

4.3 HST/COS Observations

The 18 QSOs in our sample were observed with the G130M grating of COS aboard the *Hubble Space Telescope*. Data for 16 of the QSO sightlines were obtained under program 13314, while the remaining were obtained through archival data. The observations were designed to achieved a signal to noise (S/N) greater than 10 per resolution element for each sightline. This resolution is necessary in order to observe

broad and shallow absorption lines that are expected to be associated with hot media. The spectra covered a observed frame wavelength from 1070–1465 Å corresponding to a rest-frame wavelength range of 946–1295 Å for the median redshift of the sample of $z=0.1311$.

The QSO spectra were created by coadding the individual exposures. The spectra were binned by three pixels, corresponding to half the resolution element, to enhance the S/N before any analysis was performed. As the first step, we identified the absorption lines associated with the groups. To do so, absorption lines in the entire spectra were identified. This is critical to ensure that the absorption lines associated with the target system are not blended with intervening or Milky Way absorbers. Special care has been given to the identification of metal-line species, in particular to O VI. Fortunately, the redshift range of our sample resulted in the observed wavelength of O VI shortward of 1215 Å, thus eliminating the possibility of any contamination from weak Ly α absorbers in the IGM.

Continua were fit through an automated pipeline created and described by Tumlinson et al. (2011) and Werk et al. (2012). A few sightlines exhibited complicated continua where the automated system failed and, as a result, those data were reduced individually by the authors following the prescriptions in Sembach & Savage (1992) and Sembach et al. (2004). The continuum fitting was done in a way consistent with the automated system.

Our data covered absorption lines from species such as Ly α λ 1215, Ly β λ 1025, C II λ 1036, N V λ , Si II λ 1190 λ 1193 λ 1260, Si III λ 1206 and O VI λ λ 1031 λ λ 1037, which trace gas from 10^{2-6} K. Absorption features were searched within ± 800 km s $^{-1}$ of the group’s systematic redshift. Features beyond this range were not considered to be physically related to the group. Figure 22 shows one example of our COS spectra

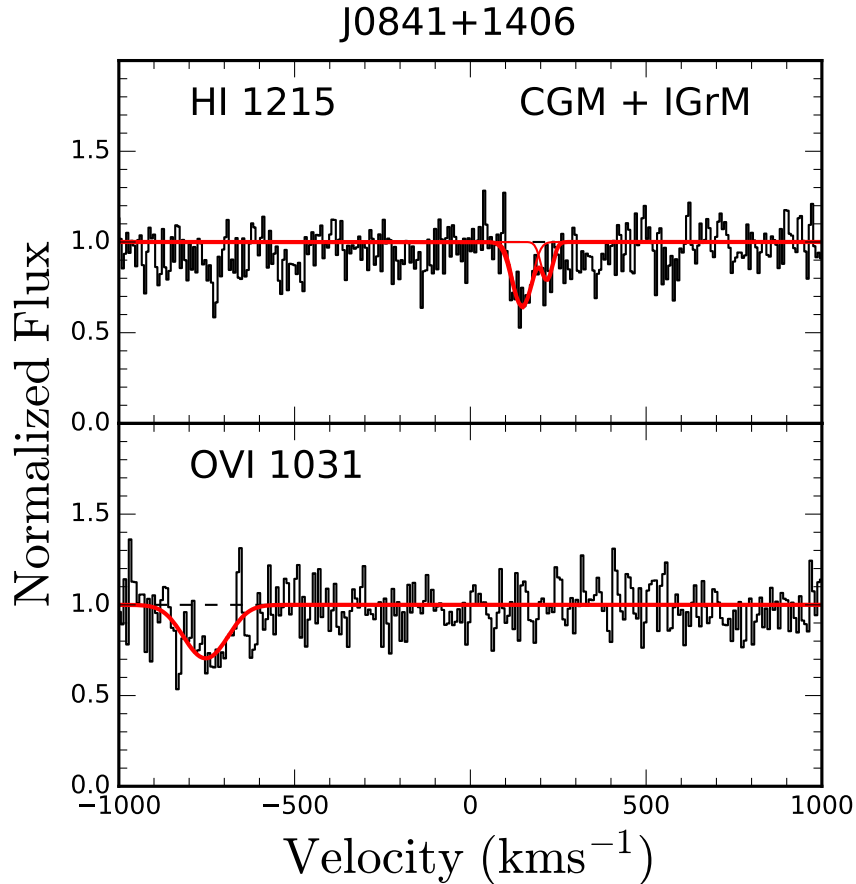


Figure 22. The observed spectra of sightline J0841+1406 showing HI and O VI detections. The Voigt profile fits are shown in red. The remainder of the spectra are presented in Appendix A.2.

with $\text{Ly}\alpha$ and O VI detections for the group J0814+1406. The rest of the spectra can be found in the complete figure set, which is available in the online journal.

Features with an equivalent width greater than 3σ were considered detections; otherwise, a 3σ upper limit was estimated. The uncertainty corresponding to each equivalent width measurement was determined through the RMS noise of the data within the measurement window. Each feature was fit with a Voigt profile in order to determine the column density, doppler ‘ b ’ parameter, and velocity centroid. For

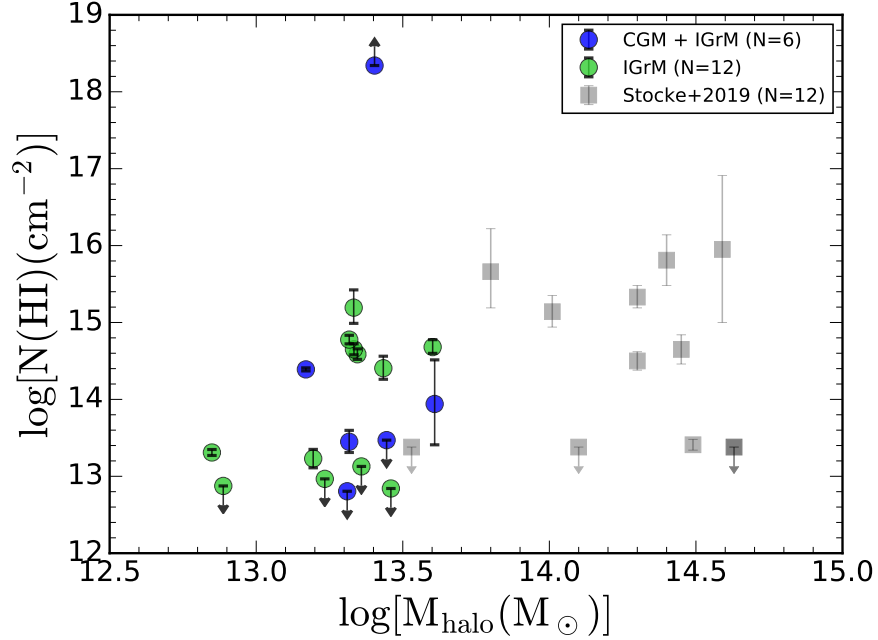


Figure 23. Ly α column density as a function of group halo mass. The COS-IGrM sightlines are shown as filled circles and the data from Stocke et al. (2019) are grey squares. The COS-IGrM sample is further split into sightlines that are expected to probe the CGM and the IGrM of galaxy groups (blue data points) and those that probe just the IGrM of the group (green data points).

sightlines with multiple absorption systems, we determined the total column density by linearly adding up the components. Unless stated otherwise, the column density represented in the figures refers to the total column density along the line of sight.

4.4 Results

We detected Ly α , Ly β , C II, N V, Si II, Si III and O VI throughout the 18 sightlines. The detection rate of Ly α is the highest at $67\pm 5\%$ (12/18) followed by O VI at $44\pm 5\%$ (8/18). We also detected low ionization species such as Si II and C II at detection

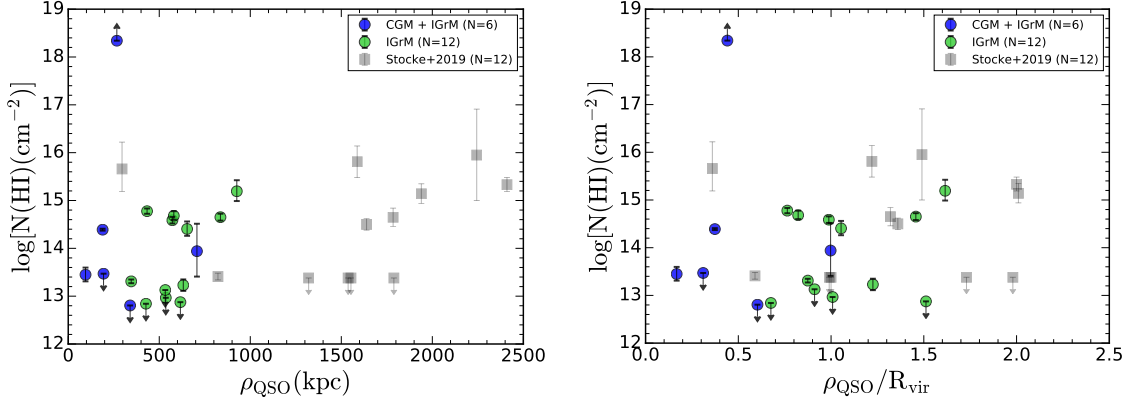


Figure 24. Ly α column densities as a function of projected QSO impact parameter (left) and the QSO impact parameter normalized by the group’s virial radius (right). The colors are the same as for Figure 23.

rates of $6\pm 5\%$ (1/18) and $28\pm 5\%$ (5/18) respectively; the intermediate species Si III at $28\pm 5\%$ (5/18); and and high ionization N V at $11\pm 5\%$ (2/18).

In the following subsections, we discuss and analyze the properties and distribution of each species. In our analysis, we also include data from the Stocke et al. (2019) IGrM survey, which covered higher mass groups. This allows us to search for trends over a larger range of halo masses and group sizes. One significant difference to note between the two surveys is that unlike the Stocke et al. sample, we do not eliminate QSO sightlines that fall within $0.25 R_{gp}$ in our sample selection.

4.4.1 Ly α Absorption

We detected Ly α absorption features in 12 of our 18 galaxy groups, with four groups having accompanying Ly β . Figure 23 presents our HI column density measurements as a function of the halo mass of the group. We found that lower mass halos exhibit a slightly narrower range of Ly α column densities compared to higher mass halos. We see no evidence of varying column densities of Ly α absorption between CGM + IGrM and

IGrM sightlines. We find that there appears to be two main populations of data points: one with moderate column densities, $\log[N(\text{H I})] \sim 14.5\text{--}15$, and another set clustered around $\log[N(\text{H I})] \sim 13$. These groupings may indicate that the QSO sightlines are passing through patchy, non-uniform H I clouds as opposed to a continuous distribution with a decreasing density gradient.

One sightline, J1127+2654, was seen to have saturated Ly α and Ly β absorption. The column density of this absorption feature should be treated as a lower limit due to the absorption line occupying the flat regime of the curve of growth. This sightline probes the IGrM as well as the CGM of the closest galaxy to the sightline, which is at $\sim 70 \text{ km s}^{-1}$ from the group’s systematic velocity and an impact parameter of $\sim 119 \text{ kpc}$. This saturated H I feature is composed of three components centered at -59 , 32 , and 116 km s^{-1} , respectively from the systemic velocity of the group, with the middle component being the strongest. The low impact parameter of $\sim 119 \text{ kpc}$ from the closest galaxy to the sightline suggests that we are likely probing the CGM of this galaxy. The location of the QSO with respect to the group member in the full environment plot in Appendix A.1.

Figure 24 shows the distribution of Ly α column density as a function of impact parameter (ρ_{QSO}) in the left panel and as a function of normalized impact parameter in the right panel (ρ_{QSO}/R_{vir}). We overplot the Stocke et al. (2019) sample as grey squares in Figure 24. We find no statistically significant correlation between the column density of Ly α absorbers and the QSO impact parameter using the Kendall’s Tau correlation test provided in the ASTRONOMY SURVIVAL ANALYSIS (ASURV) package (Feigelson & Nelson, 1985; Isobe et al., 1986; Isobe & Feigelson, 1990). Using the ASURV Kendall’s Tau test, we observed no correlation between the column density of Ly α absorption and IGrM or CGM + IGrM sightlines. Most of the stronger Ly α

absorbers ($\log[N(\text{H I})] \sim 14.5\text{-}15$) are seen in sightlines that pass through only the IGrM.

The origins of cooler, partially neutral gas are not well understood. Possible scenarios include remnants of tidally stripped structures (Davis et al., 1997; Bekki, 2009; Borthakur et al., 2010b; Nestor et al., 2011; Gauthier, 2013; Fossati et al., 2019; Péroux et al., 2019), in-situ condensation (Voit, 2019), outflowing material from star forming galaxies (Veilleux et al., 2005; Tripp et al., 2011; Nielsen et al., 2018; Frye et al., 2019) and/or cold gas accretion from the intergalactic medium (Kereš et al., 2005; Vogt et al., 2015; Bielby et al., 2017; Borthakur et al., 2019b). These processes are all capable of producing strong Ly α absorption. On the other hand, lower column density absorbers and non-detections are seen in sightlines irrespective of whether they probe the CGM or just the IGrM. The presence of weak Ly α absorbers ($\leq 10^{14} \text{ cm}^2$), including several non-detections, indicates that the sightlines pass through an ionized medium. In those sightlines, we do not find O VI or N V, indicating that the medium must be at temperatures greater than 10^6 K, assuming collisional ionization equilibrium. This phenomena might be related to the inability for galaxies in groups to continue the gas accretion necessary to fuel star formation. This has been observed in galaxy clusters (Yoon & Putman, 2013; Gim et al., 2021), and when scaled to the group environment, could indicate the beginning of the preprocessing and quenching processes (Zabludoff & Mulchaey, 1998; McGee et al., 2009; Wetzel et al., 2013; Schawinski et al., 2014; Crossett et al., 2017; Kacprzak et al., 2021).

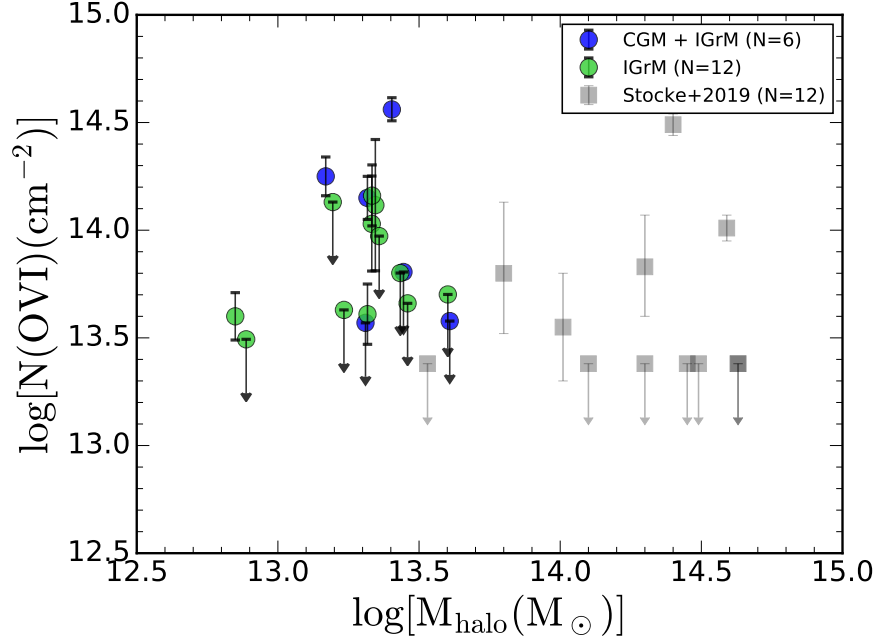


Figure 25. O VI column density detections and 3σ upper limits as a function of group halo mass for the COS-IGrM sample. The blue points indicate QSO sightlines that pass within the virial radius of individual group members, while the green points show sightlines that we expect to only probe IGrM. The gray points are from Stocke et al. (2019), which systematically selects higher mass groups.

4.4.2 Low and intermediate-ionization tracing tracing cool/warm gas

Apart from $\text{Ly}\alpha$, we also observe other transitions like Si II C II and Si III tracing gas up to the ionization potentials of 33.5 eV. C II and Si III are the most commonly detected low and intermediate-ionization species that are seen in five of the eighteen sightlines. This is consistent with other studies of the CGM and IGM (Collins et al., 2009; Shull et al., 2009; Lehner et al., 2012, 2015; Richter et al., 2016; Borthakur et al., 2016). All of these absorbers are associated with strong, most likely saturated $\text{Ly}\alpha$ absorbers.

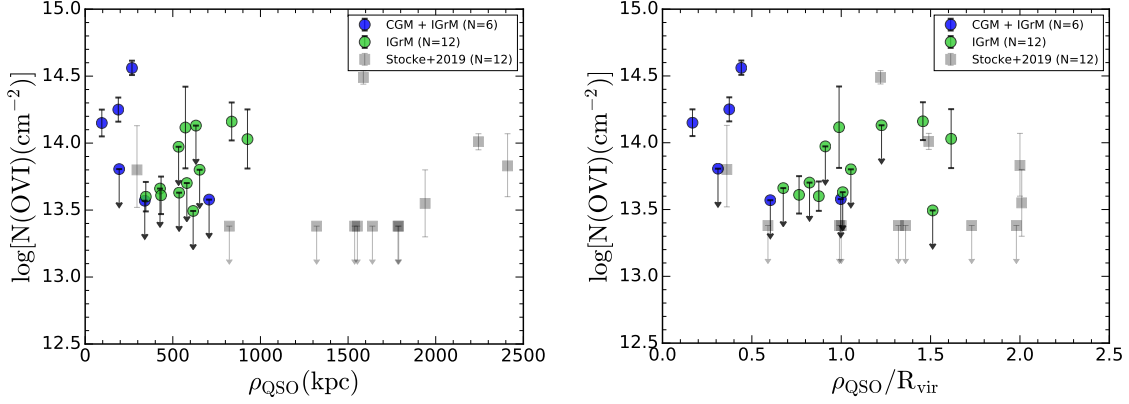


Figure 26. O VI column density detections and 3σ upper limits as a function of projected QSO impact parameter (left) and the QSO impact parameter normalized by the group’s virial radius (right). The colors are the same as in Figure 25.

4.4.3 Absorption tracing highly ionized gas

We detect O VI absorbers in 8 and N V absorbers in 2 out of our 18 sightlines. Each N V absorption feature was also present with O VI absorption. Of the eight detections, five of the sightlines were “pure” IGrM sightlines, while three sightlines were CGM + IGrM. We detected both the transitions of the O VI doublet for two sightlines. Five sightlines showed the stronger of the two transition at O VI $\lambda 1031 \text{ \AA}$, while one sightline showed absorption at O VI $\lambda 1037 \text{ \AA}$ with an intervening absorption line at the expected position of O VI $\lambda 1031 \text{ \AA}$. As noted earlier, the redshift range places the O VI doublet at observed wavelengths lower than 1215 \AA and hence we do not expect any misidentification of lower redshift Ly α absorbers as O VI. Figure 25 shows the column density of O VI absorbers from the COS-IGrM survey as well the survey by Stocke et al. (2019). Over the entire halo mass range, the O VI and N V detection rates are $44\pm 5\%$ and $11\pm 5\%$, respectively.

Figure 26 shows the O VI detections as a function of QSO impact parameter from the center of the group. We observe a flat distribution of detections from $0.1 - 1.5 R_{vir}$, which suggests that the sightlines may be probing gas that is not at the virial temperature. Since X-ray studies (Helsdon & Ponman, 2000a; Mulchaey, 2000; Robson & Davé, 2020) show temperature gradients in galaxy groups, the observed flat distribution of O VI detections provides evidence that O VI is not tracing the bulk component of the IGrM.

Another indication that the OVI absorbers in our sample is tracing a mix of hot and cool gas is the fact that while all the systems that show O VI also show Ly α , but the kinematics can be quite different. For example, six of the eight sightlines with O VI detections show Ly α absorption with the same (or slightly offset) velocity centroid, while the remaining two sightlines have Ly α at a much larger ($\gtrsim 200 \text{ km s}^{-1}$). A single ionization process could not produce both Ly α and O VI at the levels detected in some cases. Therefore, for these two different species to be observed within a close velocity offset, multiple clouds must be present, which indicates hot and cool gas in close proximity.

4.4.4 Absorber Kinematics

In this section, we use the kinematics of the absorbers to explore further the nature and distribution of gas as traced by absorption. First, we use the velocity spread of the absorbers to ascertain if the absorbing gas is bound to the group. Figure 27 (left) shows the absorption lines detected in the COS spectra at velocity relative to the

systemic velocity of the group⁸, which is depicted by the dashed line at $v - v_{sys} = 0$. Each species is color coded with the dominant absorption feature indicated by a larger halo around the data point. In total, there are 70 absorbers depicted in the plot. 29 and 12 of those are Ly α and O VI, respectively, while the remaining represent the other species discussed above. The solid lines show the escape velocity as a function of halo mass and virial radius. The right panel of Figure 27 includes the data from Stocke et al. (2019), which extends the dynamic range of halo masses.

The vast majority of the absorption features are bound to the gravitational potential of the groups. There are 9 out of 70 absorbers from five sightlines (J0841+1406, J1017+4702, J1020+1003, J1216+0712, and J1339+5355) that have sufficient velocities, relative to the group, to escape the gravitational potential. These are composed of 5 Ly α , 2 O VI, 1 C II, and 1 Si III absorbers. The same trend is observed with the data from Stocke et al. (2019) as only two absorption features (1 Ly α and 1 O VI) are observed at high enough velocity offsets to escape the group.

Among the 12 O VI absorbers detected in 8 sightlines, 83% (10/12) are gravitationally bound to their group halo and only two absorbers show velocities greater than the escape velocity. One of the unbound O VI absorbers is seen in the sightline towards J0841+1406 passes through the CGM of a 4.4 L $_*$ galaxy at 145 kpc. The velocity offset between the O VI absorber and this is $\sim 650 \text{ kms}^{-1}$. Interestingly, the O VI absorber does not have a corresponding Ly α absorber. The Ly α absorber is seen in this group is more than 600 kms^{-1} offset from the O VI absorption feature and is offset by $\sim 150 \text{ kms}^{-1}$ to the closest member galaxy. Hence, the O VI absorber could be tracing infalling or outflowing gas. The large doppler width of the O VI absorber

⁸This velocity offset is only from the line of sight velocity. As a result, if the other two velocity components were known, then the fraction of unbound absorbers could increase.

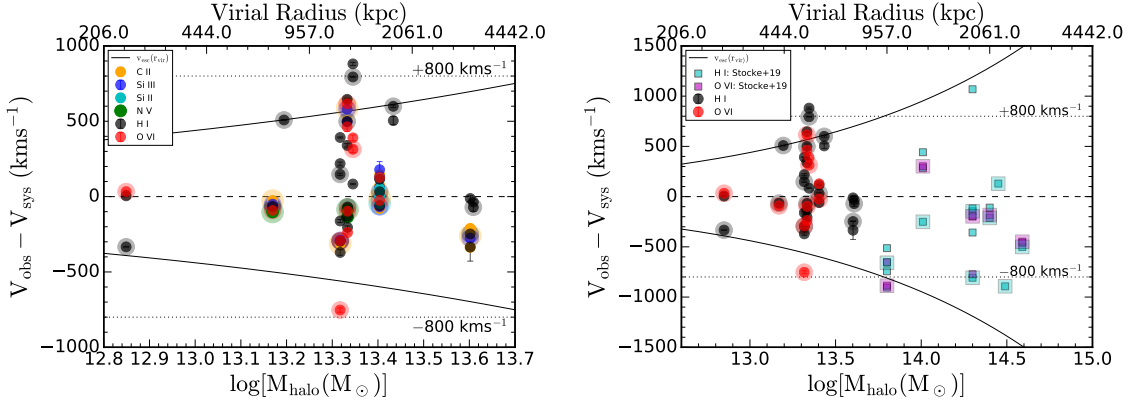


Figure 27. *Left:* Observed line of sight velocity relative to the group center for all detections compared to the halo mass of each group. The solid line represents the escape velocity of the group’s gravitational potential. The absorption features with the largest column density are marked by a lighter halo over the data point to indicate the dominant component of the transition. *Right:* Same as the left panel, but only for Ly α and O VI including the data from Stocke et al. (2019).

of $b = 81.6 \text{ km s}^{-1}$ suggests that this absorber is tracing WHIM-like material (Cen & Ostriker, 1999; Davé et al., 2001). While this doppler width is consistent with WHIM-like material, we cannot conclusively rule out the possibility that this absorber is not related to the overall gas phase. As stated in (Oppenheimer & Davé, 2009, and references therein), O VI with these doppler widths cannot be only a result of thermal broadening, but also requires a kinematic origin. This leaves some uncertainty as to the exact gas phase due to the lack of other metal-line transitions.

The second O VI absorber with a large velocity offset relative to the group is in the sightline towards J1017+4702 (Figure 37). The velocity offset of this O VI absorber is sufficient to escape the gravitational potential of the group. This sightline also exhibits a saturated Ly α profile with a column density, $\log N(\text{HI}) > 15.2$. Since Ly β is blended with an intervening absorber, we cannot utilize it to help constrain the column density. Interestingly, in this case, the sightline does not pass within the virial

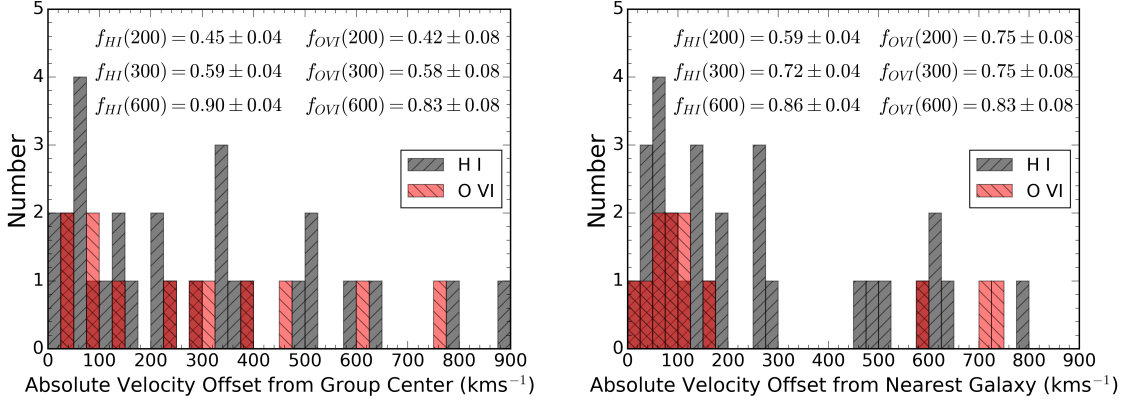


Figure 28. *Left:* Absolute velocity offset of H I (black) and O VI (red) absorbers from the center the group. The fraction of absorbers within 200, 300, and 600 kms^{-1} for both ions are displayed for all 29 Ly α and 12 O VI absorbers. *Right:* Absolute velocity offset of H I (black) and O VI (red) absorbers from the nearest galaxy to the sightline. The fraction of absorbers within 200, 300, and 600 kms^{-1} for both ions are displayed. For both ions, more than 50% are within 200 kms^{-1} of the closest galaxy to the sightline, which suggests that some of these absorbers may originate from galactic outflows.

radius of any spectroscopically confirmed L $_*$ galaxy and is at 926 kpc ($\equiv 1.6 R_{vir}$) from the group center. However, there is one galaxy with matching photometric redshift at 90 kpc from the sightline, which might be the host of this saturated absorption system. It also has a neighbor with similar photometric redshift at an impact parameter from the QSO sightline of 212 kpc. Future spectroscopic redshift measurements are needed to confirmation the association between this neighboring galaxy and the absorption features present in this sightline. If the photometric redshifts are confined, then these galaxies would most likely be part of the group.

Figure 28 (left) shows a histogram of all of the H I and O VI absorbers as a function of absolute velocity offset from the group center. This histogram quantitatively shows that the majority of both H I and O VI absorbers are gravitationally bound to the group, while $\sim 10\%$ are observed to have velocities high enough to escape the group

potential. These could either indicate infalling clouds or outflows. Therefore, we conclude that the large majority of the absorbers are tracing the cooler, gravitationally bound gas, which is centered well within the group’s escape velocity. A similar conclusion was made by the Stocke et al. (2019) study, which concluded that galaxy groups primarily act as “closed boxes” for galactic evolution at low redshifts. However, the IGrM should still experience “outside-in” enrichment from the IGM (Tegmark et al., 1993; Scannapieco et al., 2002; Oppenheimer et al., 2012). While the source of the initial IGM enrichment at early epochs is model dependent, each model of “outside-in” enrichment predicts that structures can regain metals that were expelled at earlier times.

We also investigate the velocity of the absorbers with respect to the nearest, spectroscopically confirmed member galaxy in projection. This is illustrated in the right panel of Figure 28 where H I and O VI absorption features are shown by a histogram as a function of absolute velocity from the nearest galaxy, which could range between 0 and 1600 km s^{-1} . For both H I and O VI absorbers, we see that more than 50% are within 200 km s^{-1} of the closest galaxy to the QSO sightline. The fraction increases to 70% within 300 km s^{-1} , which is less than the escape velocity of an L_* galaxy. This indicates that these absorption features may originate from gas in the CGM of member galaxies in the group. On the other hand, the absorbers at higher velocity offsets are most likely tracing patchy components of the IGrM, or inflows/outflows from individual group members.

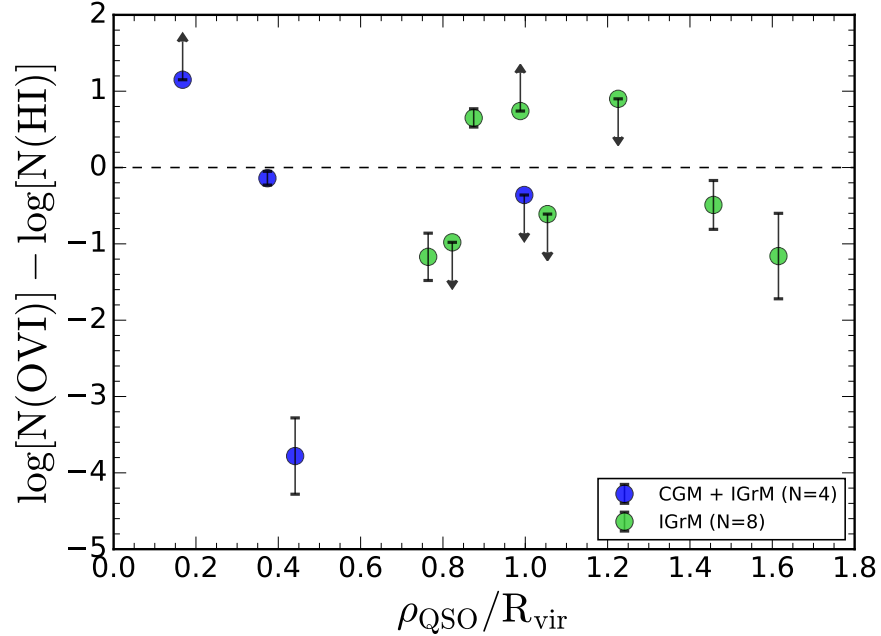


Figure 29. Ratio of O VI to H I column density as a function of normalized impact parameter for each of the 18 sightlines in the COS-IGrM sample.

4.4.5 Nature of IGrM

In order to look at the overall ionization state of the IGrM, the ratio of O VI to H I was examined for each of the 18 sightlines in the COS-IGrM sample (Figure 29). For these ratios, only the components of H I found at the same velocity as O VI were used. If there were no O VI or H I detections, then an upper limit was used. Sightlines with no Ly α or O VI absorption were not included in this analysis. The sightlines with O VI column densities greater than the H I columns shows that there is highly ionized gas throughout the IGrM, while the lack of a correlation between the ratio of column densities and impact parameter shows that there is no significant dependence of ionization state on normalized impact parameter.

Out of the 12 sightlines that show Ly α absorption, 9 of those sightlines show evidence of multiple metal-line species detected in absorption that allows us to model the ionization state of the gas. Of these 9 sightlines, 7 clearly depict multiphase gas, where various metal-line species are present in varying levels suggesting that the components have very different ionization states. The presence of these multiple components in most of the sightlines indicates that the absorption is associated with pockets of gas that maybe cooler than the rest of the media (and possibly more dense if they are in pressure equilibrium). Therefore, we believe that our data is primarily tracing a complex multiphase media, which cannot be described by a single ionization process. In Table 7, we present the probable ionization process for each group, based upon the observed spectra.

For ionization modeling, the primary interest was to determine if any of the absorption lines from the COS-IGrM sample are consistent with photoionization, collisional ionization, or inconsistent with either process. For CIE modeling, the ratio of Ly α to O VI absorption at 50% solar was examined over a range of temperatures. If the observed column density ratio was consistent with CIE predictions, then it was noted that the absorption features were consistent with CIE. Since CIE predicts broad, shallow O VI without the presence of lower ionization state transitions, only those sightlines that had Ly α and O VI were examined for consistency with CIE models.

The photoionization modeling was inherently less certain due to unresolved, blended components and a lack of multiple metal line species in the majority of sightlines. We used CLOUDY (Ferland et al., 2013) with a Haart-Madau background and a total hydrogen density grid ($\log[n(\text{H})]$ from [-5,-2] particles cm^{-3}) in 0.5 dex increments. The total neutral column density was fixed to the observed Ly α column density. If a point in the grid existed where the column density ratio each metal species was consistent

Table 7. Results of ionization modeling for sightlines with identified absorption features.

| Group | Ionization Model |
|------------|--|
| J0841+1406 | Consistent with CIE at $\sim 10^{5.4}$ K or at $\sim 10^{5.7}$ K |
| J1017+4702 | C II/Si III ratio consistent with photoionization between $10^{-3} < n(h) < 10^{-2.5} \text{ cm}^{-3}$; Higher velocity components inconsistent with photoionization |
| J1020+1003 | Insufficient data for modeling |
| J1126+1204 | Insufficient data for modeling |
| J1127+2654 | Inconsistent with photoionization (1) |
| J1216+0712 | Consistent with CIE at $\sim 10^{5.2-5.3}$ K |
| J1301+2819 | Lowest velocity component of Ly α and O VI consistent with CIE at $\sim 10^{5.3}$ K or at $\sim 10^{5.9-6}$ K; The N V/O VI ratio for the higher velocity components ($v \sim -100 \text{ km s}^{-1}$) is consistent with photoionization between $10^{-4} < n(h) < 10^{-3.5} \text{ cm}^{-3}$. |
| J1339+5355 | Insufficient data for modeling |
| J1343+2538 | Consistent with CIE at $\sim 10^{5.3-5.4}$ K or $\sim 10^{5.9}$ K |
| J1348+4303 | C II/Si III ratio consistent with photoionization between $10^{-2.5} < n(h) < 10^{-2} \text{ cm}^{-3}$ |
| J1424+4214 | Low velocity component ($v \sim -100 \text{ km s}^{-1}$) inconsistent with photoionization, but is consistent with CIE at $\sim 10^{5.2-5.3}$ K; Higher velocity component ($v \sim -55 \text{ km s}^{-1}$) C II/Si III ratio consistent with photoionization between $10^{-5} < n(h) < 10^{-4.5} \text{ cm}^{-3}$ or $10^{-3} < n(h) < 10^{-2.5} \text{ cm}^{-3}$ (2). |
| J1428+3225 | Inconsistent with photoionization |

NOTE— (1) Since individual O VI components may be blended, we cannot definitively rule out photoionization based upon Si III components. (2) There may be an unresolved, blended component of C II, which increases the uncertainty in the density required for photoionization to be confirmed.

within the same density grid point, then we stated that the absorption components were consistent with photoionization.

Some sightlines show absorbers that match the ratios and strengths predicted by CIE (Gnat & Sternberg, 2007) for a hot $\approx 10^{5.5}$ K medium. For example, the sightline J1343+2538 (Figure 44) passing through a group at an impact parameter of 346 kpc ($\equiv 0.9 R_{vir}$), shows broad Ly α ($b_{Ly\alpha} = 47 \text{ km s}^{-1}$) along with O VI suggestive of hot media (Richter et al., 2006). The ratio of O VI to Ly α column density of 0.65 dex is consistent with temperatures of $10^{5.3-5.4}$ K or $10^{5.9}$ K for $0.5-1 [Z/H]_{\odot}$ with temperature inverse proportional to the metallicity for the same column density ratio. The choice of this metallicity range is based on measurement from X-ray studies for groups of galaxies that typically find the average metallicities of the X-ray bright IGrM to be $0.4-0.6 [Z/H]_{\odot}$ (Helsdon & Ponman, 2000a). We do not have strong

metallicity constrains for non-X-ray bright groups, so we adopt the metallicities seen in X-ray studies.

Another example of collisional ionized gas are seen in the sightline towards group J1301+2819 (Figure 42). In addition to tracing hot gas, this sightline shows a mix of multiple ionization states at slightly different velocities possibly tracing a multi-phase medium. The Ly α feature shows three components - two strong components with associated Ly β and one weak component with $\log N(\text{HI})=13.05$. The strong components are seen in both N V and O VI (the components are blended in O VI), whereas the weakest component is most prominent in O VI. This indicates that the different components trace different ionization states. For weakest component the ratios of O VI and Ly α are in agreement with collision ionization equilibrium model. The ratio of column densities, $\log N(\text{OVI}) - \log N(\text{HI}) = 0.60$, corresponds to gas at $10^{5.3}$ K or $10^{5.9-6}$ K at 50% solar metallicity. At lower metallicities, the observed ratio of column densities between O VI and Ly α would indicate a slightly higher temperature.

On the other hand, the stronger components are quite puzzling. If photoionization was responsible for the observed ionization states, there should be other low-ionization transitions detected besides H I such as Si II, C II and Si III. Despite these transitions not being present at detectable levels in the spectra, the N V to O VI ratio is consistent with photoionization (Table 7). Therefore, we are unable to conclusively state the process behind the observed column densities, it is most likely a mixture of multiple ionization processes.

A similar case of multiphase media is seen in J1424+4214 (Figure 46), which shows two distinct ionization states with a velocity separation of about 45 kms^{-1} : a less ionized system at $\sim -55 \text{ kms}^{-1}$ and a highly ionized state at $\sim -100 \text{ kms}^{-1}$. One

component is seen in lower ionization transitions like Ly α , C II, and Si III, while the second components is seen in higher ionization transitions like N V, O VI, as well as Si III that show a weak feature suggesting Si III is not the dominant ionization state of silicon. The ratio of these lines indicate that the two components are at very different ionization states, thus suggesting that the IGrM is multiphase and cannot be described by a single ionization state. While the ionization processes for each of the two components cannot definitively be determined based upon the data at hand, the component centered at $\sim -100 \text{ kms}^{-1}$ is consistent with CIE at $\sim 10^{5.2-5.3} \text{ K}$, while the component at $\sim -55 \text{ kms}^{-1}$ is consistent with photoionization based upon the C II to Si III line ratio.

Another sightline of interest is towards the group J1127+2654 (Figure 40). This sightline exhibits a saturated Ly α profile with column density, $\log N(\text{HI}) > 18.3$, which makes it a Lyman-limit system (LLS, Lanzetta et al., 1995, and references therein). The absorber complex shows multiple components commonly associated with extended disk (Lehner et al., 2009), inner CGM (Werk et al., 2014; Armillotta et al., 2017; Fielding et al., 2020), and/or tidal structures (Frye et al., 2019). This QSO passes within $\sim 119 \text{ kpc}$ from a known group member; however, higher resolution spectroscopy and a rotation curve is necessary to confirm the connection between this LLS and the member galaxy. Similarly, due to the blending of O VI components in this QSO spectra, we cannot rule out photoionization as the primary ionization mechanism for these absorption lines.

Lastly, the sightline towards J1017+4702 (Figure 37) shows that Ly α is saturated at the same position as C II, Si III, and broad, shallow O VI. Photoionization alone cannot produce broad, shallow O VI and CIE does not predict the existence of saturated Ly α and broad O VI at a single temperature. Since this is an IGrM sightline, the

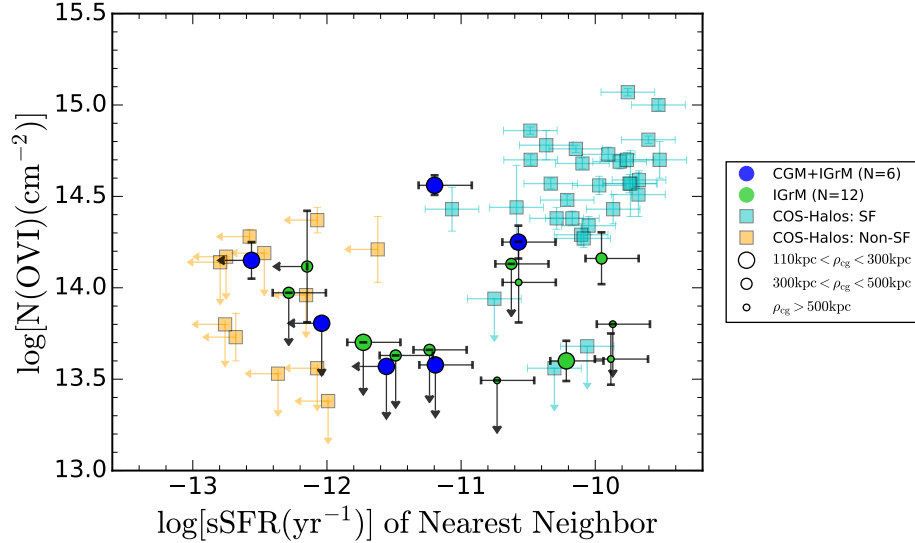


Figure 30. O VI column density as a function of the specific star formation rate of the nearest member galaxy to the QSO sightline. The blue (CGM + IGrM) and green (IGrM) points show the COS-IGrM sample and the size of the points correspond to the impact parameter from the closest, spectroscopically confirmed member galaxy. The cyan and orange data points show the results from the COS-Halos survey (Tumlinson et al., 2011), which robustly observed an increased amount of O VI in the CGM of star forming galaxies.

broad O VI may be tracing a hotter component; however, the lower transitions show evidence of cooler gas at the same velocity. Photoionization modeling with CLOUDY (Ferland et al., 2013) showed that the lower velocity components of C II and Si III are consistent with photoionization, while the higher velocity components are inconsistent with photoionization. Overall, it is clear that the ionization states of these groups are complex and the ionization processes behind the multiphase gas cannot always be explained by either photoionization or CIE. Future studies with better modeling, higher resolution observations, and broader wavelength coverage can help shed insight into these ionization processes.

4.4.6 Origin of O VI Absorbers

We differentiate between CGM and IGrM absorption in galaxy groups by comparing our O VI detections to those detected in the COS-Halos survey (Tumlinson et al., 2011). The COS-Halos survey discovered that a strong correlation between O VI in the CGM and the star formation rate of galaxies existed. In order to compare the our data with the COS-Halos sample, we determined the galaxy closest to the QSO sightline and then matched the galaxy to the star formation rate from the MPA-JHU DR7⁹ galaxy catalog (Brinchmann et al., 2004).

Figure 30 shows our data along with those from the COS-Halos survey. The CGM+IGrM sightlines, shown as deep blue circles, have a clear host galaxy as the sightline passes within the viral radius (assuming an isolated halo) of a member galaxy. The pure IGrM sightlines do not pass through the CGM of the nearest galaxy (shown in green circles). Therefore, they are not applicable for comparison with the COS-Halos sample; nevertheless, we show them on the plot for comparison with the CGM+IGrM sub-sample. It is worth noting that even the blue points that do probe the CGM pass through the outer CGM ($\rho > 110$ kpc) and not the inner CGM like COS-Halos sample.

Overall, we do not see a trend of higher O VI levels as a function of the specific star formation rate (sSFR) or the star formation rate of the nearest galaxy. This is not surprising considering the impact parameters. However, it does suggest that the origin of our O VI absorbers are probably not related to the star formation activity of individual galaxies and therefore, we are most likely not tracing the CGM gas physics as seen in the COS-Halos survey, but instead, a more group-related phenomena.

⁹<https://wwwmpa.mpa-garching.mpg.de/SDSS/DR7/>

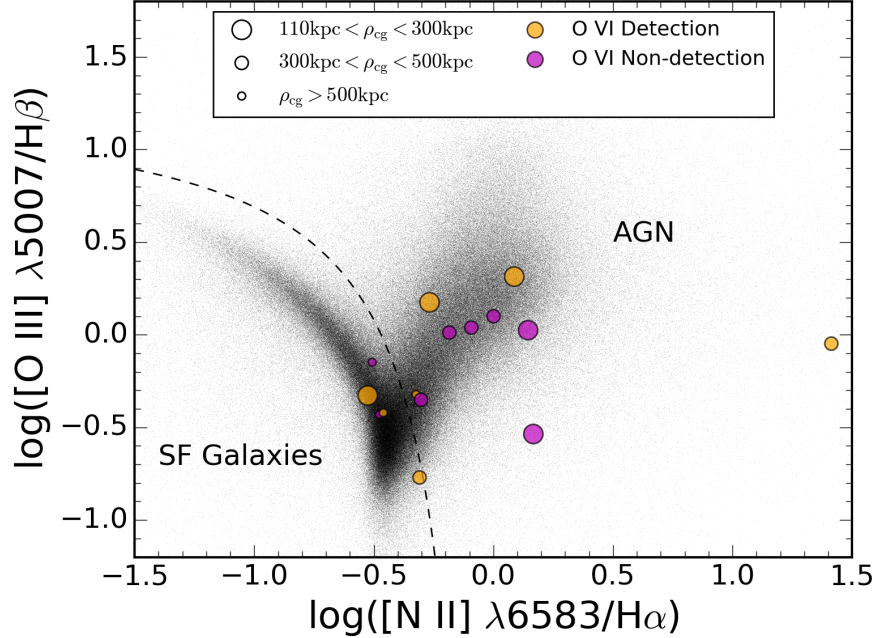


Figure 31. BPT diagram showing the locations of the COS-IGrM sample where reliable flux measurements from the MPA-JHU DR7 catalog were present. The division between phase space pertaining to either star forming or AGN galaxies is marked by the dashed line (Kauffmann et al., 2003). The colored circles represent sightlines with O VI detections vs. non-detections and the size of the circles represents the projected impact parameter to the closest galaxy to the sightline.

While we can confidently rule out the CGM of L_* galaxies as the source of O VI absorbers, there could potentially be smaller galaxies that may be present closer to the sightline. A much deeper redshift survey of galaxies in the vicinity of the QSO sightlines would enable us to quantify the presence of low-mass galaxies. Nevertheless, sub- L_* galaxies are not expected to have significant metal reservoirs beyond their inner CGM ($\rho > 0.5 R_{vir}$) (Bordoloi et al., 2014). Hence, it is not likely that the CGM of sub- L_* galaxies could dominate the O VI detected in our sample. On the other hand, material spread out by tidal interactions can have a large cross-section on the sky and may survive as faint diffuse partially neutral gas in the IGrM for hundreds of millions of years (Borthakur et al., 2010b, 2015b).

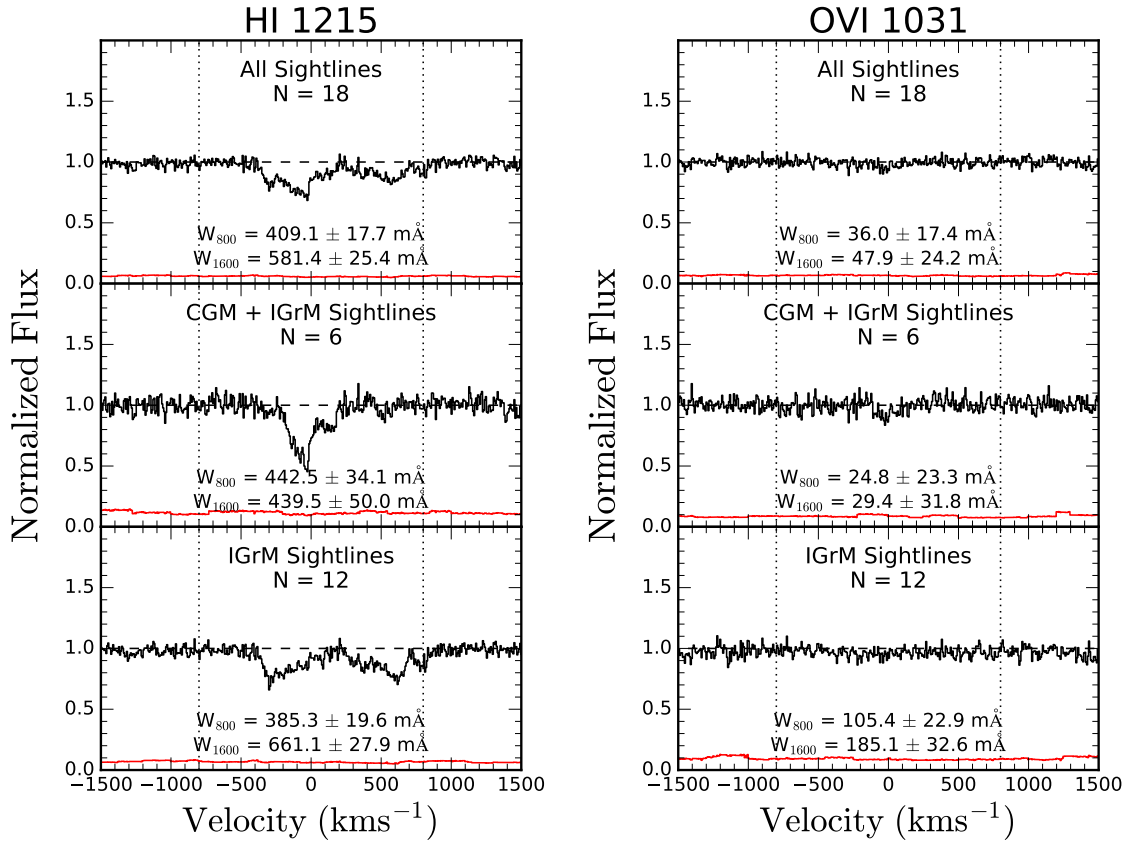


Figure 32. Stacked spectra for Ly α (left) and O VI (right) for each of the 18 sightlines in the COS-IGrM sample (top). The sightlines were also divided into the IGrM and CGM sightlines and stacks of each were created (middle and bottom respectively). The stacks are centered on the center of mass velocity of the group and all intervening absorption features were removed.

Our sample shows a larger fraction of green valley galaxies than typically observed in the Universe. Jian et al. (2020) finds that on average, 20% of galaxies populate the green valley and the majority of those are field galaxies and not those found in more dense environments. Observing $\sim 33\%$ of the closest galaxies to the QSO sightline in our sample to be in the green valley reinforces the idea that galaxy group environments may act as important sites where the process of quenching is active (Wetzel et al.,

2012, 2013). The role of the IGrM or the CGM in turning these galaxies green is still unclear.

Another possibility for the origin of O VI in the IGrM could be due to AGN activity. In order to address this, used the emission line ratios from the MPA-JHU¹⁰ DR7 catalog to construct a Baldwin, Phillips & Terlevich (BPT) diagram (Baldwin et al., 1981) so that star forming galaxies could be separated from AGN using the demarcation as defined by Kauffmann et al. (2003). The locations of the COS-IGrM sample compared to the SDSS DR7 sample from the MPA-JHU catalog are shown in Figure 31 as colored circles. 15 out of the 18 groups in our sample had emission line measurements for the closest galaxy to the QSO sightline and therefore, could be included in the BPT diagram. The color of the circle represents O VI detections (orange) vs. non-detections (magenta). The size of the symbol represents the impact parameter of the sightline, where larger sizes indicate small impact parameter. We do not find any systematic over-density of O VI detection or non-detection in sightlines with or without AGN. Therefore, we conclude that AGN activity is not the primarily contributor of O VI in the IGrM.

4.4.7 Stacked Spectra

In order to look for fainter gas associated with the IGrM, we stacked sightlines centered around the group systemic velocity for Ly α and O VI. For each species, stacks were created using all 18 sightlines as well as subsets of CGM + IGrM or IGrM only sightlines. These stacks are shown in Figure 32 along with the number of sightlines going into each subset. The equivalent widths were measured for velocities within

¹⁰https://www.sdss.org/dr14/spectro/galaxy_mpa_jhu/

$\pm 400 \text{ km s}^{-1}$ and $\pm 800 \text{ km s}^{-1}$ from the group's systematic redshift. These values are listed as W_{800} and W_{1600} respectively.

The Ly α stacks show net absorption centered around zero velocity for the CGM + IGrM subset, and absorption corresponding to higher velocity offsets in the IGrM stack. When we stack the full COS-IGrM sample, we observe a combination of the two subsets meaning that the IGrM in our sample is traced by two distinct regions: gas at the systematic velocity of the group as well as gas that is at larger velocities than the group's systemic velocity. This could perhaps be a result of warmer gas condensing in the outskirts and falling back towards the center of the group.

The O VI stacks show weak net absorption throughout all the sightlines. However, there is absorption in the IGrM sightlines. Both the CGM + IGrM stack and the pure IGrM stack show that the majority of the absorption is within of the central 800 km s^{-1} of the group. The covering fraction of the IGrM stacks is more uniform than the CGM stacks as there is net absorption throughout the $\pm 800 \text{ km s}^{-1}$. Non-detection of O VI in the full stack indicates that there is not a volume filling phase of the IGrM, but instead, an O VI traced IGrM is a more transient phenomena.

4.5 Discussion

From the COS-IGrM survey, we have observed no significant trends between the column density of Ly α or O VI and the physical parameters of the group such as virial radius, impact parameter, and halo mass. This may be an indication that we are not observing a hot, volume filling IGrM; instead we are detecting cooler pockets of gas that are perhaps in pressure confinement within the IGrM. This would line up more closely with what was concluded in Stocke et al. (2017); Pointon et al. (2017)

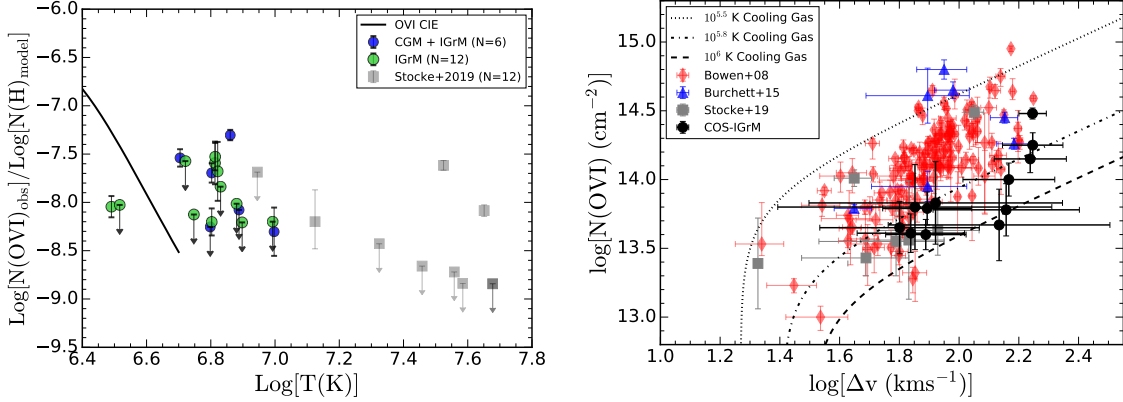


Figure 33. (Left:) Observed O VI column densities normalized by the QSO path length through the group as a function of group virial temperature ($N(\text{HI})_{\text{model}}$). The blue and green data points are from the COS-IGrM sample, while the gray squares show the results from Stocke et al. (2019). The solid, black line represents theoretical predictions based on collisional ionization equilibrium models from Gnat & Sternberg (2007) assuming 50% solar metallicity, assuming a total hydrogen density of 10^{-3} cm^{-3} (Right:) O VI column density as a function of the detected O VI line width (Δv). The dotted, dot-dashed, and dashed lines show radiative cooling models from Bordoloi et al. (2017) at $10^{5.5} \text{ K}$, $10^{5.8} \text{ K}$, and 10^6 K , respectively.

and Stocke et al. (2019) for more massive groups. If this is indeed correct, X-ray spectroscopy of O VII and O VIII would be required to observe the hotter component of the IGrM, even for lower mass groups ($10^{12.8} - 10^{13.7} M_{\odot}$).

This idea is further reinforced by looking at the virial temperatures of the groups compared to the predicted O VI column densities from collisional ionization equilibrium models (Gnat & Sternberg, 2007). Figure 33 (left) shows the predicted and observed column densities of O VI normalized by the total hydrogen column density through the group as a function of virial temperature (denoted by $N(\text{HI})_{\text{model}}$). The column density of hydrogen was estimated by using the IGrM gas density of $n = 10^{-3} \text{ cm}^{-3}$, and multiplying it by the total path length through each group in our sample, which is approximated by a sphere of radius, $2R_{\text{vir}}$. The gas density was selected as a conservative estimate based upon electron density profiles from X-ray data of galaxy

groups (Sun et al., 2003; Khosroshahi et al., 2004) and from density measurements of the IGrM from double bent radio jets (Freeland & Wilcots, 2011). From this figure, it is evident that we are primarily observing cooler gas than what would be at the group’s virial temperature based upon the amount of O VI observed, which provides more support to our previous statements.

To investigate the theory that the observed O VI is due to cooler gas than the hotter IGrM, we looked at the relationship between the O VI column density and the O VI line width for our sample and other samples from various environments (right panel of Figure 33). Heckman et al. (2002) demonstrated that O VI absorption lines in various environments such as the Milky Way, high velocity clouds, Magellanic Clouds, starburst galaxies, and the intergalactic medium all can be described by radiatively cooling gas through the relationship between column density and the Doppler ‘ b ’ parameter. Bordoloi et al. (2017) revisited these models to show that the line width, $\Delta v = 3b_D/\sqrt{2}$, is a more appropriate tracer of the flow velocity than the Doppler ‘ b ’ parameter in describing the radiatively cooling O VI. We show data from Bowen et al. (2008), Burchett et al. (2015), and Stocke et al. (2019) along with the COS-IGrM survey O VI detections¹¹ to show that the trends observed from O VI in the Milky Way and the IGM also largely agree with O VI detected in the IGrM, respectively. On average, the COS-IGrM data can be described by radiatively cooling gas between $10^{5.8}$ K, and 10^6 K. This may be indicating that the O VI detected in our sample originates from gas falling towards member galaxies and cools radiatively as it passes through the CGM of a group member or passes through cooler pockets within the hotter IGrM.

¹¹Since the line width is related to the Doppler ‘ b ’ parameter and therefore a Voigt profile fit, there is no physical upper limit for non-detections.

The cooling models described in Bordoloi et al. (2017) predict that N v column densities should be about an order of magnitude lower than those predicted for O vi. This prediction is consistent with our three N v detections as well as our upper limits in this sample based upon the $10^{5.27}$ K cooling curves in Bordoloi et al. (2017). Since many of the O vi detections are relatively close to the detection limit, the lack of N v detections is not unexpected due to this prediction.

Lastly, we can make an estimate as to the total amount of oxygen in these galaxy groups. Following equation 1 in Tumlinson et al. (2011), we can calculate the minimum mass of oxygen in galaxy group halos by:

$$M_O = 5\pi \langle R_{vir} \rangle^2 \langle N_{OVI} \rangle m_O f_{hit} \left(\frac{0.2}{f_{OVI}} \right) \quad (4.4)$$

where f_{OVI} is the fraction of oxygen that is in O vi based upon CIE models Gnat & Sternberg (2007). Using both the mean and median values of the O vi column densities and group virial radii, we can determine the minimum amount of oxygen mass in our galaxy groups. This can be compared to the amount of oxygen in the member galaxies by assuming $M_O \sim 0.065 M_*$ (Peeples et al., 2014; Tumlinson et al., 2017). This difference (gray shaded region) is shown in Figure 34 for both the mean (dashed lines) and median (solid lines) values of the stellar masses of group members. Based upon the virial temperature of these galaxy groups in Figure 33, the corresponding fraction of oxygen in O vi is $< 10^{-4}$. Therefore, we can estimate that over the narrow temperature range corresponding to f_{OVI} of $10^{-4} - 10^{-5}$ ($10^{6.55} - 10^{6.75}$ K), there is upwards of $10^{11.6} M_\odot$ of oxygen in the IGrM.

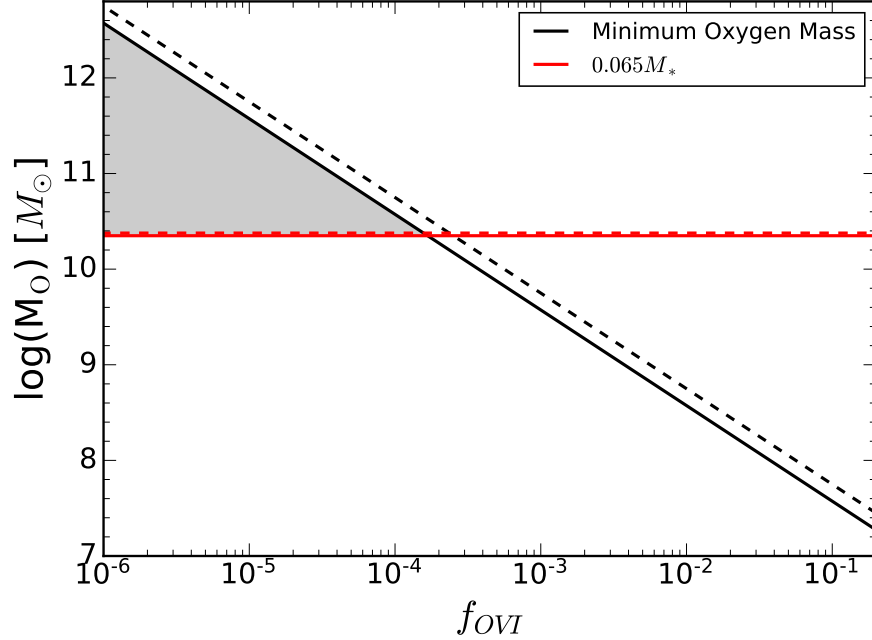


Figure 34. The minimum mass of oxygen as calculated by Equation 4.4 compared to the mass of oxygen in the member galaxies. The solid lines show the masses determined by median values while the dashed lines show the masses determined through the mean of the stellar mass, virial radii, and O VI column densities. The gray shaded region shows the mass of oxygen that can be attributed to the IGrM at various values of f_{OVI} , the fraction of oxygen that is in O VI.

4.5.1 Future Outlook

In order to accurately and completely characterize the IGrM, higher ionization species should be targeted in future studies. From the COS-IGrM survey, it is clear that O VI is not an ideal tracer of the IGrM. Since O VI is only observed in 8 out of our 18 groups, the predominant, volume filling component of the IGrM should exist at a hotter temperature for galaxy groups at halo masses between $12. M_{\odot} < \log[M_{halo}] < 14.7 M_{\odot}$. We can rule out a pervasive media of the IGrM at cooler temperatures due to the weak low and medium ionization potential lines observed in our data. Therefore,

to observe the dominant phase of the IGrM, future studies should look to O VII, O VIII, Ne VIII and Mg X, which are stronger transitions at temperatures of $10^{6.5} - 10^{7.5}$ K.

Once the pervasive phase of the IGrM is observed, it can be combined with other studies to fully characterize the IGrM of galaxy groups. Simulations by Davé et al. (2002); Le Brun et al. (2017); Farahi et al. (2018) have made substantial progress in determining consistent scaling relations for lower mass halos that are consistent with observational programs such as those by Sun et al. (2003); Eckmiller et al. (2011); Babyk et al. (2018); Lovisari et al. (2020). Additionally, the thermal SZ effect is being utilized in order to determine the baryonic content of lower mass galaxy clusters and groups (Vikram et al., 2017; Henden et al., 2019; Pratt & Bregman, 2020, and references therein). By the combination of these results, these hot halos can be fully characterized.

4.6 Conclusions

We present the results of the COS-IGrM survey, where 18 QSO sightlines passing through galaxy groups ($0.2R_{vir} \leq \rho \leq 1.6R_{vir}$) were studied in an effort to characterize the IGrM. Our conclusions are as follows:

1. We detect Ly α absorption in 12 of the 18 galaxy groups, with 4 of those groups also having corresponding Ly β absorption. However, we detect no statistically significant trend between Ly α column density and halo mass or QSO impact parameter.
2. 8 of the 18 groups show the presence of O VI thus the covering fraction of O VI is $44 \pm 5\%$. The lack of O VI absorption in over 50% of our sample indicates that the volume filling IGrM at (or near) the virial temperature of galaxy groups

is not primarily traced by O VI. We also find no correlation between column density of O VI and halo mass or QSO impact parameter.

3. C II, Si II, Si III, and N V absorption was detected in 5, 1, 5, and 2 groups, respectively. These lead to covering fractions of $28\pm 5\%$, $6\pm 5\%$, $28\pm 5\%$, and $11\pm 5\%$ for C II, Si II, Si III, and N V, respectively. These data suggest that the low-ionization transitions are primarily due to photoionization or other non-equilibrium processes.
4. We find evidence that the IGrM is multiphase and has a complex structure. While higher resolution spectra and coverage of more intermediate ionization transitions are necessary for complete ionization modeling, we find five instances where CIE explains the observed spectra and four instances where photoionization is consistent with the transitions present.
5. We find that 9 out of 70 absorbers ($13\pm 1\%$) have sufficient velocities, relative to the group, to escape the group’s gravitational potential. Therefore, we conclude that galaxy groups are primarily “closed boxes” for galaxy evolution at low redshifts ($0.1 \leq z \leq 0.2$).
6. We show that the O VI absorbers can be described by radiatively cooling gas between $10^{5.8}$ K, and 10^6 K. This might indicate that the O VI detected in our sample originates from pockets of gas cooling within the hotter component of the IGrM.
7. We do not find evidence of AGN activity having an impact on whether or not O VI is detected within a group or not. Similarly, we do not observe the star formation of the nearest spectroscopically confirmed neighbor to be a driver for O VI.
8. We observe some O VI absorption in our stacked data. This shows evidence of

O VI traced IGrM throughout our sample. Despite O VI not being the dominant form of oxygen at the virial temperature of these galaxy groups, we see evidence that we are observing gas cooler than the hot, volume filling component of the IGrM that could be observed in X-rays via O VII, O VIII, Na XII, or extreme-UV lines such as Ne VIII.

Since the O VI detections are determined to be primarily tracers of cooler pockets of gas and not the IGrM at the virial temperature of the group, full accounting for the amount of baryonic matter in these groups cannot be accurately measured with the data in hand. In order to complete the baryon census for galaxy groups, future studies should try and observe higher ionization states such as O VII and O VIII, which will trace gas closer to the virial temperature of galaxy groups.

CONCLUSION AND FUTURE OUTLOOK

In order to fill in the missing puzzle pieces to fully understand how galaxies grow and evolve, it is necessary to characterize the environment, CGM, and IGrM. In this dissertation, a combination of ground based and space based observations were discussed to paint a picture of the role of group environments on galaxy evolution. Despite not making any groundbreaking new claims about this process, this dissertation helps to lay the ground work for future studies that might be able to further our understanding.

In Chapter 2, the capabilities of large, ground based telescopes were utilized to create large mosaics with $\gtrsim 28$ hrs of total exposure time. Typically, every individual exposure would be used to create the deepest image possible, with the hopes of seeing the faintest galaxies or stars possible. However, as demonstrated, this might not be the best way to make use of all the data. By sorting each of the individual exposures by seeing (point source FWHM), optimal resolution and optimal depth mosaics can be created following the prescriptions detailed in this dissertation. The optimal resolution image allows for fine structure to be observed and studied, especially when paired with high resolution, space based imaging such as *HST* or *JWST*. Conversely, the optimal depth mosaic allows for low surface brightness regions such as galaxy outskirts, tidal tails, and potentially IGrL to be observed.

In Chapter 3, the optimal depth mosaic creation method was used to study the IGrM through emission by searching for signatures of IGrL. Prior to this point, individual case studies of IGrL have been observed through a handful of “best case”

scenarios where groups were compact, rich, and close to the Milky Way. As the compactness and richness of a group becomes higher, the probability of interactions such as mergers and/or tidal interactions increases leading to stars escaping an individual galaxy and populating the IGrM. As these stars build up and populate the IGrM, faint light can be observed. However, most groups don't fit these criteria. Therefore, by selecting groups without prior selection criteria for compactness or richness, a search for IGrL can help provide insight as to whether IGrL is due to gravitationally stripped stars or if star formation is taking place in situ.

Starting with a U-band optimal depth mosaic of the COSMOS field and a catalog of known galaxy groups, IGrL was searched for by making cutouts of each group and stacking them together to increase the IGrL signal while reducing the background noise. By using U-band imaging, the star formation theory could be tested as young stars would produce higher amount of U-band light compared to older populations of stars that would have been formed longer ago within a galaxy and then removed via interactions prior to settling towards the center of the group to form IGrL. Regardless of the stacking technique, no signatures of IGrL were found with the U-band stacks. However, robust upper limits were measured, which places the maximum amount of IGrL present in context with studies from the literature (Figure 20).

The IGrL upper limits suggest that the build up of IGrL is more likely to be a result of stars stripped through galaxy interactions and other gravitational interactions as groups become more evolved, instead of star formation that is occurring outside of galaxies. These limits, combined with an increased number of IGrL detections at longer wavelengths, suggest that IGrL is dominated by older stellar populations and not young stars or active star formation. Therefore, in order to conduct a similar

search for IGrL without bias towards compact and rich groups, the next step would be to perform a similar analysis with deep, r -band imaging.

Lastly, in Chapter 4, the IGrM was studied through a more traditional technique where galaxy groups were paired with a background QSO. Using a UV spectrograph such as COS aboard *HST*, absorption lines stemming from gas gravitationally bound to the group could be observed and fit with Voigt profiles to determine the physical parameters such as column density, velocity centroid, and doppler b value. This technique is sensitive to diffuse gas that does not have a sufficient density or temperature to emit light. However, the limitation is that a single line of sight is assumed to be representative of the entire IGrM. This is clearly not a strong assumption, but it is the best that can be done currently with the low probability of a bright enough QSO being located behind a galaxy group within an optimal redshift range for *HST*/COS observations.

From the COS-IGrM survey of 18 groups, 12/18 sightlines were observed to have Ly α detections, 8/18 groups had O VI detections, and cooler transitions such as C II, Si II, Si III, and N V were observed in a maximum of 5/18 groups. The absence of abundant O VI detections suggests that O VI is not a tracer of a volume filling component of the IGrM. While collisional ionization modeling suggests that O VI should be the dominant ionization state at the predicted temperature of the IGrM, these sightlines suggest otherwise. Furthermore, absorption lines tracing gas at cooler temperatures are observed less frequently. These data paint a picture of a volume filling component of the IGrM that is hotter than previously thought and could be traced by higher ionization states of oxygen such as O VII and O VIII.

This dissertation attempts to highlight the importance of group environments on galaxy evolution and provide insight for how future studies can increase knowledge of

these processes. Ground based observations serve as an important tool for measuring diffuse light that isn't always seen with *HST*, while space based observatories remain paramount for UV observations of nearby galaxies. As future 30m class telescopes become operational, the ability for future IGrL studies, especially in the *r*-band, may prove to be easier to achieve. Since the majority of galaxies exist in group environments, understanding the connection between IGrL, the IGrM, and individual galaxies stands as one of the prominent areas to shape our understanding of galaxy evolution.

REFERENCES

- Adams, D., Mehta, V., Dickinson, H., et al. 2022, *ApJ*, , 931, 16, doi: 10.3847/1538-4357/ac6512
- Aguerri, J. A. L., Castro-Rodríguez, N., Napolitano, N., Arnaboldi, M., & Gerhard, O. 2006, *A&A*, , 457, 771, doi: 10.1051/0004-6361:20065783
- Ahoranta, J., Nevalainen, J., Wijers, N., et al. 2020, *A&A*, , 634, A106, doi: 10.1051/0004-6361/201935846
- Ahumada, R., Prieto, C. A., Almeida, A., et al. 2020, *ApJS*, , 249, 3, doi: 10.3847/1538-4365/ab929e
- Andrews, S. K., Driver, S. P., Davies, L. J. M., Lagos, C. d. P., & Robotham, A. S. G. 2018, *MNRAS*, , 474, 898, doi: 10.1093/mnras/stx2843
- Armillotta, L., Fraternali, F., Werk, J. K., Prochaska, J. X., & Marinacci, F. 2017, *MNRAS*, , 470, 114, doi: 10.1093/mnras/stx1239
- Ashcraft, T. A., Windhorst, R. A., Jansen, R. A., et al. 2018, *PASP*, , 130, 064102, doi: 10.1088/1538-3873/aab542
- Ashcraft, T. A., McCabe, T., Redshaw, C., et al. 2023, *PASP*, , 135, 024101, doi: 10.1088/1538-3873/aca1e0
- Babyk, I. V., McNamara, B. R., Nulsen, P. E. J., et al. 2018, *ApJ*, , 857, 32, doi: 10.3847/1538-4357/aab3c9
- Baldwin, J. A., Phillips, M. M., & Terlevich, R. 1981, *PASP*, , 93, 5, doi: 10.1086/130766
- Barnes, J. 1985, *MNRAS*, , 215, 517, doi: 10.1093/mnras/215.3.517
- Barnes, J. E. 1992, *ApJ*, , 393, 484, doi: 10.1086/171522
- Beckwith, S. V. W., Stiavelli, M., Koekemoer, A. M., et al. 2006, *AJ*, , 132, 1729, doi: 10.1086/507302
- Bekki, K. 2009, *MNRAS*, , 399, 2221, doi: 10.1111/j.1365-2966.2009.15431.x
- Bertin, E., & Arnouts, S. 1996, *A&AS*, , 117, 393, doi: 10.1051/aas:1996164
- Bertin, G., & Amorisco, N. C. 2010, *A&A*, , 512, A17, doi: 10.1051/0004-6361/200913611

- Bertin, G., Ciotti, L., & Del Principe, M. 2002, *A&A*, , 386, 149, doi: 10.1051/0004-6361:20020248
- Bianchi, L., Efremova, B., Herald, J., et al. 2011, *MNRAS*, , 411, 2770, doi: 10.1111/j.1365-2966.2010.17890.x
- Bielby, R., Crighton, N. H. M., Fumagalli, M., et al. 2017, *MNRAS*, , 468, 1373, doi: 10.1093/mnras/stx528
- Blanton, M. R., Schlegel, D. J., Strauss, M. A., et al. 2005, *AJ*, , 129, 2562, doi: 10.1086/429803
- Blanton, M. R., Bershad, M. A., Abolfathi, B., et al. 2017, *AJ*, , 154, 28, doi: 10.3847/1538-3881/aa7567
- Bordoloi, R., Wagner, A. Y., Heckman, T. M., & Norman, C. A. 2017, *ApJ*, , 848, 122, doi: 10.3847/1538-4357/aa8e9c
- Bordoloi, R., Tumlinson, J., Werk, J. K., et al. 2014, *ApJ*, , 796, 136, doi: 10.1088/0004-637X/796/2/136
- Borthakur, S., Momjian, E., Heckman, T. M., et al. 2019a, *ApJ*, , 871, 239, doi: 10.3847/1538-4357/aaf566
- . 2019b, *ApJ*, , 871, 239, doi: 10.3847/1538-4357/aaf566
- Borthakur, S., Yun, M. S., & Verdes-Montenegro, L. 2010a, *ApJ*, , 710, 385, doi: 10.1088/0004-637X/710/1/385
- . 2010b, *ApJ*, , 710, 385, doi: 10.1088/0004-637X/710/1/385
- Borthakur, S., Yun, M. S., Verdes-Montenegro, L., et al. 2015a, *ApJ*, , 812, 78, doi: 10.1088/0004-637X/812/1/78
- . 2015b, *ApJ*, , 812, 78, doi: 10.1088/0004-637X/812/1/78
- Borthakur, S., Heckman, T., Tumlinson, J., et al. 2016, *ApJ*, , 833, 259, doi: 10.3847/1538-4357/833/2/259
- Bowen, D. V., Jenkins, E. B., Tripp, T. M., et al. 2008, *ApJS*, , 176, 59, doi: 10.1086/524773
- Bregman, J. N., Anderson, M. E., Miller, M. J., et al. 2018, *ApJ*, , 862, 3, doi: 10.3847/1538-4357/aacafe
- Bregman, J. N., & Lloyd-Davies, E. J. 2007, *ApJ*, , 669, 990, doi: 10.1086/521321

- Brinchmann, J., Charlot, S., White, S. D. M., et al. 2004, *MNRAS*, , 351, 1151, doi: 10.1111/j.1365-2966.2004.07881.x
- Bundy, K., Ellis, R. S., & Conselice, C. J. 2005, *ApJ*, , 625, 621, doi: 10.1086/429549
- Burchett, J. N., Tripp, T. M., Prochaska, J. X., et al. 2015, *ApJ*, , 815, 91, doi: 10.1088/0004-637X/815/2/91
- Burkey, J. M., Keel, W. C., Windhorst, R. A., & Franklin, B. E. 1994, *ApJL*, , 429, L13, doi: 10.1086/187402
- Carleton, T., Windhorst, R. A., O'Brien, R., et al. 2022, *AJ*, , 164, 170, doi: 10.3847/1538-3881/ac8d02
- Cattapan, A., Spavone, M., Iodice, E., et al. 2019, *The Astrophysical Journal*, 874, 130, doi: 10.3847/1538-4357/ab0b44
- Cen, R., & Ostriker, J. P. 1999, *ApJ*, , 514, 1, doi: 10.1086/306949
- Churchill, C. W., Kacprzak, G. G., Steidel, C. C., et al. 2012, *ApJ*, , 760, 68, doi: 10.1088/0004-637X/760/1/68
- Cluver, M., Verdes-Montenegro, L. L., & Hess, K. M. 2016, in *MeerKAT Science: On the Pathway to the SKA*, 22, doi: 10.22323/1.277.0022
- Coccatto, L., Gerhard, O., & Arnaboldi, M. 2010, *MNRAS*, , 407, L26, doi: 10.1111/j.1745-3933.2010.00897.x
- Coenda, V., Muriel, H., & Martínez, H. J. 2012, *A&A*, , 543, A119, doi: 10.1051/0004-6361/201118318
- Collins, J. A., Shull, J. M., & Giroux, M. L. 2009, *ApJ*, , 705, 962, doi: 10.1088/0004-637X/705/1/962
- Conselice, C. J. 2014, *ARA&A*, , 52, 291, doi: 10.1146/annurev-astro-081913-040037
- Crossett, J. P., Pimbblet, K. A., Jones, D. H., Brown, M. J. I., & Stott, J. P. 2017, *MNRAS*, , 464, 480, doi: 10.1093/mnras/stw2228
- Cui, W., Murante, G., Monaco, P., et al. 2014, *MNRAS*, , 437, 816, doi: 10.1093/mnras/stt1940
- Da Rocha, C., & Mendes de Oliveira, C. 2005, *MNRAS*, , 364, 1069, doi: 10.1111/j.1365-2966.2005.09641.x
- Da Rocha, C., Ziegler, B. L., & Mendes de Oliveira, C. 2008, *MNRAS*, , 388, 1433, doi: 10.1111/j.1365-2966.2008.13500.x

- Darg, D. W., Kaviraj, S., Lintott, C. J., et al. 2010, MNRAS, , 401, 1043, doi: 10.1111/j.1365-2966.2009.15686.x
- Davé, R., Katz, N., & Weinberg, D. H. 2002, ApJ, , 579, 23, doi: 10.1086/342706
- Davé, R., Cen, R., Ostriker, J. P., et al. 2001, ApJ, , 552, 473, doi: 10.1086/320548
- Davis, D. S., Keel, W. C., Mulchaey, J. S., & Henning, P. A. 1997, AJ, , 114, 613, doi: 10.1086/118497
- Davis, M., Guhathakurta, P., Konidaris, N. P., et al. 2007, ApJL, , 660, L1, doi: 10.1086/517931
- De Lucia, G., Springel, V., White, S. D. M., Croton, D., & Kauffmann, G. 2006, MNRAS, , 366, 499, doi: 10.1111/j.1365-2966.2005.09879.x
- Driver, S. P., & Robotham, A. S. G. 2010, MNRAS, , 407, 2131, doi: 10.1111/j.1365-2966.2010.17028.x
- Driver, S. P., Norberg, P., Baldry, I. K., et al. 2009, Astronomy and Geophysics, 50, 5.12, doi: 10.1111/j.1468-4004.2009.50512.x
- Driver, S. P., Hill, D. T., Kelvin, L. S., et al. 2011, MNRAS, , 413, 971, doi: 10.1111/j.1365-2966.2010.18188.x
- Driver, S. P., Andrews, S. K., Davies, L. J., et al. 2016, ApJ, , 827, 108, doi: 10.3847/0004-637X/827/2/108
- Duncan, K., Conselice, C. J., Mundy, C., et al. 2019, ApJ, , 876, 110, doi: 10.3847/1538-4357/ab148a
- Džudžar, R., Kilborn, V., Meurer, G., et al. 2019, MNRAS, , 483, 5409, doi: 10.1093/mnras/sty3500
- Eckert, D., Gaspari, M., Gastaldello, F., Le Brun, A. M. C., & O’Sullivan, E. 2021, Universe, 7, 142, doi: 10.3390/universe7050142
- Eckmiller, H. J., Hudson, D. S., & Reiprich, T. H. 2011, A&A, , 535, A105, doi: 10.1051/0004-6361/201116734
- Elmegreen, B. G., Elmegreen, D. M., Fernandez, M. X., & Lemonias, J. J. 2009a, ApJ, , 692, 12, doi: 10.1088/0004-637X/692/1/12
- Elmegreen, B. G., Galliano, E., & Alloin, D. 2009b, ApJ, , 703, 1297, doi: 10.1088/0004-637X/703/2/1297
- Elmegreen, D. M., Elmegreen, B. G., Ferguson, T., & Mullan, B. 2007, ApJ, , 663, 734, doi: 10.1086/518715

- Elmegreen, D. M., Elmegreen, B. G., Whitmore, B. C., et al. 2021, *ApJ*, , 908, 121, doi: 10.3847/1538-4357/abd541
- Farahi, A., Evrard, A. E., McCarthy, I., Barnes, D. J., & Kay, S. T. 2018, *MNRAS*, , 478, 2618, doi: 10.1093/mnras/sty1179
- Feigelson, E. D., & Nelson, P. I. 1985, *ApJ*, , 293, 192, doi: 10.1086/163225
- Ferland, G. J., Porter, R. L., van Hoof, P. A. M., et al. 2013, *Rev. Mexicana Astron. Astrofis.*, , 49, 137. <https://arxiv.org/abs/1302.4485>
- Fielding, D. B., Tonnesen, S., DeFelippis, D., et al. 2020, *ApJ*, , 903, 32, doi: 10.3847/1538-4357/abbc6d
- Finkelstein, S. L., Bagley, M. B., Arrabal Haro, P., et al. 2022, arXiv e-prints, arXiv:2207.12474. <https://arxiv.org/abs/2207.12474>
- Fisher, D. B., Glazebrook, K., Bolatto, A., et al. 2014, *ApJL*, , 790, L30, doi: 10.1088/2041-8205/790/2/L30
- Fossati, M., Fumagalli, M., Lofthouse, E. K., et al. 2019, *MNRAS*, , 490, 1451, doi: 10.1093/mnras/stz2693
- Freeland, E., & Wilcots, E. 2011, *ApJ*, , 738, 145, doi: 10.1088/0004-637X/738/2/145
- Frye, B. L., Bowen, D. V., Tripp, T. M., et al. 2019, *ApJ*, , 872, 129, doi: 10.3847/1538-4357/ab0083
- Fukugita, M., & Peebles, P. J. E. 2006, *ApJ*, , 639, 590, doi: 10.1086/499556
- Gaspari, M., Tombesi, F., & Cappi, M. 2020, *Nature Astronomy*, 4, 10, doi: 10.1038/s41550-019-0970-1
- Gauthier, J.-R. 2013, *MNRAS*, , 432, 1444, doi: 10.1093/mnras/stt565
- Giallongo, E., Ragazzoni, R., Grazian, A., et al. 2008, *A&A*, , 482, 349, doi: 10.1051/0004-6361:20078402
- Giavalisco, M., Ferguson, H. C., Koekemoer, A. M., et al. 2004, *ApJL*, , 600, L93, doi: 10.1086/379232
- Gim, H., Borthakur, A., Heckman, T., & Padave, M. 2021, *MNRAS*,
- Gitti, M., Brighenti, F., & McNamara, B. R. 2012, *Advances in Astronomy*, 2012, 950641, doi: 10.1155/2012/950641
- Gnat, O., & Sternberg, A. 2007, *ApJS*, , 168, 213, doi: 10.1086/509786

- Grazian, A., Menci, N., Giallongo, E., et al. 2009, *A&A*, , 505, 1041, doi: 10.1051/0004-6361/200912118
- Greco, J. P., Hill, J. C., Spergel, D. N., & Battaglia, N. 2015, *ApJ*, , 808, 151, doi: 10.1088/0004-637X/808/2/151
- Green, J. C., Froning, C. S., Osterman, S., et al. 2012, *ApJ*, , 744, 60, doi: 10.1088/0004-637X/744/1/60
- Grogin, N. A., Kocevski, D. D., Faber, S. M., et al. 2011, *ApJS*, , 197, 35, doi: 10.1088/0067-0049/197/2/35
- Hauser, M. G., Arendt, R. G., Kelsall, T., et al. 1998, *ApJ*, , 508, 25, doi: 10.1086/306379
- Heckman, T. M., & Best, P. N. 2014, *ARA&A*, , 52, 589, doi: 10.1146/annurev-astro-081913-035722
- Heckman, T. M., Norman, C. A., Strickland, D. K., & Sembach, K. R. 2002, *ApJ*, , 577, 691, doi: 10.1086/342232
- Helsdon, S. F., & Ponman, T. J. 2000a, *MNRAS*, , 315, 356, doi: 10.1046/j.1365-8711.2000.03396.x
- . 2000b, *MNRAS*, , 315, 356, doi: 10.1046/j.1365-8711.2000.03396.x
- Henden, N. A., Puchwein, E., & Sijacki, D. 2019, *MNRAS*, , 489, 2439, doi: 10.1093/mnras/stz2301
- Hernquist, L. 1989, *Nature*, , 340, 687, doi: 10.1038/340687a0
- Hickson, P. 1982, *ApJ*, , 255, 382, doi: 10.1086/159838
- Hickson, P., Mendes de Oliveira, C., Huchra, J. P., & Palumbo, G. G. 1992, *ApJ*, , 399, 353, doi: 10.1086/171932
- Hickson, P., Richstone, D. O., & Turner, E. L. 1977, *ApJ*, , 213, 323, doi: 10.1086/155158
- Isobe, T., & Feigelson, E. D. 1990, in *Bulletin of the American Astronomical Society*, Vol. 22, 917–918
- Isobe, T., Feigelson, E. D., & Nelson, P. I. 1986, *ApJ*, , 306, 490, doi: 10.1086/164359
- Jian, H.-Y., Lin, L., Koyama, Y., et al. 2020, *ApJ*, , 894, 125, doi: 10.3847/1538-4357/ab86a8
- Jiménez-Teja, Y., & Dupke, R. 2016, *ApJ*, , 820, 49, doi: 10.3847/0004-637X/820/1/49

- Kacprzak, G. G., Nielsen, N. M., Nateghi, H., et al. 2021, MNRAS, , 500, 2289, doi: 10.1093/mnras/staa3461
- Karachentsev, I. D., Karachentseva, V. E., Huchtmeier, W. K., & Makarov, D. I. 2004, AJ, , 127, 2031, doi: 10.1086/382905
- Kauffmann, G., Heckman, T. M., Tremonti, C., et al. 2003, MNRAS, , 346, 1055, doi: 10.1111/j.1365-2966.2003.07154.x
- Kereš, D., Katz, N., Weinberg, D. H., & Davé, R. 2005, MNRAS, , 363, 2, doi: 10.1111/j.1365-2966.2005.09451.x
- Khosroshahi, H. G., Jones, L. R., & Ponman, T. J. 2004, MNRAS, , 349, 1240, doi: 10.1111/j.1365-2966.2004.07575.x
- Knobel, C., Lilly, S. J., Iovino, A., et al. 2012, ApJ, , 753, 121, doi: 10.1088/0004-637X/753/2/121
- Koekemoer, A. M., Aussel, H., Calzetti, D., et al. 2007, ApJS, , 172, 196, doi: 10.1086/520086
- Koekemoer, A. M., Faber, S. M., Ferguson, H. C., et al. 2011, ApJS, , 197, 36, doi: 10.1088/0067-0049/197/2/36
- Kolcu, T., Crossett, J. P., Bellhouse, C., & McGee, S. 2022, MNRAS, , 515, 5877, doi: 10.1093/mnras/stac2177
- Korngut, P. M., Kim, M. G., Arai, T., et al. 2022, ApJ, , 926, 133, doi: 10.3847/1538-4357/ac44ff
- Lanzetta, K. M., Wolfe, A. M., & Turnshek, D. A. 1995, ApJ, , 440, 435, doi: 10.1086/175286
- Lauer, T. R., Postman, M., Weaver, H. A., et al. 2021, ApJ, , 906, 77, doi: 10.3847/1538-4357/abc881
- Lauer, T. R., Postman, M., Spencer, J. R., et al. 2022, ApJL, , 927, L8, doi: 10.3847/2041-8213/ac573d
- Le Brun, A. M. C., McCarthy, I. G., & Melin, J.-B. 2015, MNRAS, , 451, 3868, doi: 10.1093/mnras/stv1172
- Le Brun, A. M. C., McCarthy, I. G., Schaye, J., & Ponman, T. J. 2017, MNRAS, , 466, 4442, doi: 10.1093/mnras/stw3361
- Lehner, N., Howk, J. C., Thom, C., et al. 2012, MNRAS, , 424, 2896, doi: 10.1111/j.1365-2966.2012.21428.x

- Lehner, N., Howk, J. C., & Wakker, B. P. 2015, *ApJ*, , 804, 79, doi: 10.1088/0004-637X/804/2/79
- Lehner, N., Prochaska, J. X., Kobulnicky, H. A., et al. 2009, *ApJ*, , 694, 734, doi: 10.1088/0004-637X/694/2/734
- Lotz, J. M., Jonsson, P., Cox, T. J., et al. 2011, *ApJ*, , 742, 103, doi: 10.1088/0004-637X/742/2/103
- Lotz, J. M., Davis, M., Faber, S. M., et al. 2008, *ApJ*, , 672, 177, doi: 10.1086/523659
- Lovisari, L., Schellenberger, G., Sereno, M., et al. 2020, *ApJ*, , 892, 102, doi: 10.3847/1538-4357/ab7997
- Martínez-Lombilla, C., Brough, S., Montes, M., et al. 2023, *MNRAS*, , 518, 1195, doi: 10.1093/mnras/stac3119
- Matsumoto, T., Tsumura, K., Matsuoka, Y., & Pyo, J. 2018, *AJ*, , 156, 86, doi: 10.3847/1538-3881/aad0f0
- Matsumoto, T., Matsuura, S., Murakami, H., et al. 2005, *ApJ*, , 626, 31, doi: 10.1086/429383
- Matsumoto, T., Seo, H. J., Jeong, W. S., et al. 2011, *ApJ*, , 742, 124, doi: 10.1088/0004-637X/742/2/124
- McCabe, T., Borthakur, S., Heckman, T., et al. 2021, *ApJ*, , 923, 189, doi: 10.3847/1538-4357/ac283c
- McCabe, T., Redshaw, C., Otteson, L., et al. 2023, *PASP*, , 135, 064101, doi: 10.1088/1538-3873/acdf83
- McGee, S. L., Balogh, M. L., Bower, R. G., Font, A. S., & McCarthy, I. G. 2009, *MNRAS*, , 400, 937, doi: 10.1111/j.1365-2966.2009.15507.x
- McNamara, B. R., & Nulsen, P. E. J. 2007, *ARA&A*, , 45, 117, doi: 10.1146/annurev.astro.45.051806.110625
- McQuinn, M., & Werk, J. K. 2018, *ApJ*, , 852, 33, doi: 10.3847/1538-4357/aa9d3f
- McVittie, G. C., & Wyatt, S. P. 1959, *ApJ*, , 130, 1, doi: 10.1086/146688
- Metcalf, N., Shanks, T., Campos, A., McCracken, H. J., & Fong, R. 2001, *MNRAS*, , 323, 795, doi: 10.1046/j.1365-8711.2001.04168.x
- Mihos, J. C. 2004, in *Clusters of Galaxies: Probes of Cosmological Structure and Galaxy Evolution*, ed. J. S. Mulchaey, A. Dressler, & A. Oemler, 277

- Mohamed, Y. H., & Reshetnikov, V. P. 2011, *Astrophysics*, 54, 155, doi: 10.1007/s10511-011-9168-7
- Montes, M. 2022, *Nature Astronomy*, 6, 308, doi: 10.1038/s41550-022-01616-z
- Mulchaey, J. S. 2000, *ARA&A*, , 38, 289, doi: 10.1146/annurev.astro.38.1.289
- Mulchaey, J. S., Davis, D. S., Mushotzky, R. F., & Burstein, D. 1996a, *ApJ*, , 456, 80, doi: 10.1086/176629
- Mulchaey, J. S., Mushotzky, R. F., Burstein, D., & Davis, D. S. 1996b, *ApJL*, , 456, L5, doi: 10.1086/309861
- Murante, G., Giovalli, M., Gerhard, O., et al. 2007, *MNRAS*, , 377, 2, doi: 10.1111/j.1365-2966.2007.11568.x
- Murante, G., Arnaboldi, M., Gerhard, O., et al. 2004, *ApJL*, , 607, L83, doi: 10.1086/421348
- Narayanan, A., Savage, B. D., Mishra, P. K., et al. 2018, *MNRAS*, , 475, 3529, doi: 10.1093/mnras/sty042
- Nestor, D. B., Johnson, B. D., Wild, V., et al. 2011, *MNRAS*, , 412, 1559, doi: 10.1111/j.1365-2966.2010.17865.x
- Nielsen, N. M., Kacprzak, G. G., Pointon, S. K., Churchill, C. W., & Murphy, M. T. 2018, *ApJ*, , 869, 153, doi: 10.3847/1538-4357/aaedbd
- Nishiura, S., Murayama, T., Shimada, M., et al. 2000, *AJ*, , 120, 2355, doi: 10.1086/316799
- Oke, J. B., & Gunn, J. E. 1983, *ApJ*, , 266, 713, doi: 10.1086/160817
- Oppenheimer, B. D., & Davé, R. 2009, *MNRAS*, , 395, 1875, doi: 10.1111/j.1365-2966.2009.14676.x
- Oppenheimer, B. D., Davé, R., Katz, N., Kollmeier, J. A., & Weinberg, D. H. 2012, *MNRAS*, , 420, 829, doi: 10.1111/j.1365-2966.2011.20096.x
- Otteson, L., McCabe, T., Ashcraft, T. A., et al. 2021, *Research Notes of the American Astronomical Society*, 5, 190, doi: 10.3847/2515-5172/ac1db6
- Overzier, R. A., Heckman, T. M., Tremonti, C., et al. 2009, *ApJ*, , 706, 203, doi: 10.1088/0004-637X/706/1/203
- Pachat, S., Narayanan, A., Muzahid, S., et al. 2016, *MNRAS*, , 458, 733, doi: 10.1093/mnras/stw194

- Peeples, M. S., Werk, J. K., Tumlinson, J., et al. 2014, *ApJ*, , 786, 54, doi: 10.1088/0004-637X/786/1/54
- Péroux, C., Zwaan, M. A., Klitsch, A., et al. 2019, *MNRAS*, , 485, 1595, doi: 10.1093/mnras/stz202
- Persic, M., & Salucci, P. 1992, *MNRAS*, , 258, 14P, doi: 10.1093/mnras/258.1.14P
- Pisano, D. J., Barnes, D. G., Staveley-Smith, L., et al. 2011, *ApJS*, , 197, 28, doi: 10.1088/0067-0049/197/2/28
- Planck Collaboration, Aghanim, N., Akrami, Y., et al. 2020, *A&A*, , 641, A6, doi: 10.1051/0004-6361/201833910
- Pointon, S. K., Nielsen, N. M., Kacprzak, G. G., et al. 2017, *ApJ*, , 844, 23, doi: 10.3847/1538-4357/aa7743
- Poliakov, D., Mosenkov, A. V., Brosch, N., Koriski, S., & Rich, R. M. 2021, *MNRAS*, , 503, 6059, doi: 10.1093/mnras/stab853
- Pratt, C. T., & Bregman, J. N. 2020, *ApJ*, , 890, 156, doi: 10.3847/1538-4357/ab6e6c
- Puget, J. L., Abergel, A., Bernard, J. P., et al. 1996, *A&A*, , 308, L5
- Purcell, C. W., Bullock, J. S., & Zentner, A. R. 2007, *ApJ*, , 666, 20, doi: 10.1086/519787
- Raj, M. A., Iodice, E., Napolitano, N. R., et al. 2020, *A&A*, , 640, A137, doi: 10.1051/0004-6361/202038043
- Rauch, M. 1998, *ARA&A*, , 36, 267, doi: 10.1146/annurev.astro.36.1.267
- Redshaw, C., McCabe, T., Otteson, L., et al. 2022, *Research Notes of the American Astronomical Society*, 6, 63, doi: 10.3847/2515-5172/ac6189
- Richter, P., Savage, B. D., Sembach, K. R., & Tripp, T. M. 2006, *A&A*, , 445, 827, doi: 10.1051/0004-6361:20053636
- Richter, P., Wakker, B. P., Fechner, C., et al. 2016, *A&A*, , 590, A68, doi: 10.1051/0004-6361/201527038
- Rix, H.-W., Barden, M., Beckwith, S. V. W., et al. 2004, *ApJS*, , 152, 163, doi: 10.1086/420885
- Robson, D., & Davé, R. 2020, *MNRAS*, , 498, 3061, doi: 10.1093/mnras/staa2394
- Rosenwasser, B., Muzahid, S., Charlton, J. C., et al. 2018, *MNRAS*, , 476, 2258, doi: 10.1093/mnras/sty211

- Roychowdhury, S., Meyer, M. J., Rhee, J., et al. 2022, *ApJ*, , 927, 20, doi: 10.3847/1538-4357/ac49ea
- Rudick, C. S., Mihos, J. C., Frey, L. H., & McBride, C. K. 2009, *ApJ*, , 699, 1518, doi: 10.1088/0004-637X/699/2/1518
- Rudick, C. S., Mihos, J. C., & McBride, C. 2006, *ApJ*, , 648, 936, doi: 10.1086/506176
- Salpeter, E. E. 1955, *ApJ*, , 121, 161, doi: 10.1086/145971
- Savage, B. D., Kim, T. S., Keeney, B., et al. 2012, *ApJ*, , 753, 80, doi: 10.1088/0004-637X/753/1/80
- Savage, B. D., Kim, T. S., Wakker, B. P., et al. 2014, *ApJS*, , 212, 8, doi: 10.1088/0067-0049/212/1/8
- Savage, B. D., Narayanan, A., Wakker, B. P., et al. 2010, *ApJ*, , 719, 1526, doi: 10.1088/0004-637X/719/2/1526
- Sawicki, M., Arnouts, S., Huang, J., et al. 2019, *MNRAS*, , 489, 5202, doi: 10.1093/mnras/stz2522
- Scannapieco, E., Ferrara, A., & Madau, P. 2002, *ApJ*, , 574, 590, doi: 10.1086/341114
- Schawinski, K., Urry, C. M., Simmons, B. D., et al. 2014, *MNRAS*, , 440, 889, doi: 10.1093/mnras/stu327
- Scoville, N., Aussel, H., Brusa, M., et al. 2007, *ApJS*, , 172, 1, doi: 10.1086/516585
- Sembach, K. R., & Savage, B. D. 1992, *ApJS*, , 83, 147, doi: 10.1086/191734
- Sembach, K. R., Tripp, T. M., Savage, B. D., & Richter, P. 2004, *ApJS*, , 155, 351, doi: 10.1086/425037
- Shull, J. M., Jones, J. R., Danforth, C. W., & Collins, J. A. 2009, *ApJ*, , 699, 754, doi: 10.1088/0004-637X/699/1/754
- Shull, J. M., Smith, B. D., & Danforth, C. W. 2012, *ApJ*, , 759, 23, doi: 10.1088/0004-637X/759/1/23
- Spavone, M., Iodice, E., Capaccioli, M., et al. 2018, *ApJ*, , 864, 149, doi: 10.3847/1538-4357/aad6e9
- Spergel, D. N., Bean, R., Doré, O., et al. 2007, *ApJS*, , 170, 377, doi: 10.1086/513700
- Springel, V., White, S. D. M., Jenkins, A., et al. 2005, *Nature*, , 435, 629, doi: 10.1038/nature03597

- Stoche, J. T., Keeney, B. A., Danforth, C. W., et al. 2017, *ApJ*, , 838, 37, doi: 10.3847/1538-4357/aa64e2
- . 2019, *ApJS*, , 240, 15, doi: 10.3847/1538-4365/aaf73d
- Stoche, J. T., Penton, S. V., Danforth, C. W., et al. 2006, *ApJ*, , 641, 217, doi: 10.1086/500386
- Stoche, J. T., Keeney, B. A., Danforth, C. W., et al. 2014, *ApJ*, , 791, 128, doi: 10.1088/0004-637X/791/2/128
- Straughn, A. N., Cohen, S. H., Ryan, R. E., et al. 2006, *ApJ*, , 639, 724, doi: 10.1086/499576
- Straughn, A. N., Voyer, E. N., Eufrazio, R. T., et al. 2015, *ApJ*, , 814, 97, doi: 10.1088/0004-637X/814/2/97
- Sun, M., Forman, W., Vikhlinin, A., et al. 2003, *ApJ*, , 598, 250, doi: 10.1086/378887
- Tago, E., Saar, E., Tempel, E., et al. 2010, *A&A*, , 514, A102, doi: 10.1051/0004-6361/200913687
- Tanimura, H., Hinshaw, G., McCarthy, I. G., et al. 2020, *MNRAS*, , 491, 2318, doi: 10.1093/mnras/stz3130
- Taylor, V. A., Jansen, R. A., & Windhorst, R. A. 2004, *PASP*, , 116, 762, doi: 10.1086/422929
- Tegmark, M., Silk, J., & Evrard, A. 1993, *ApJ*, , 417, 54, doi: 10.1086/173290
- Toomre, A., & Toomre, J. 1972, *ApJ*, , 178, 623, doi: 10.1086/151823
- Tripp, T. M., & Savage, B. D. 2000, *ApJ*, , 542, 42, doi: 10.1086/309506
- Tripp, T. M., Savage, B. D., & Jenkins, E. B. 2000, *ApJL*, , 534, L1, doi: 10.1086/312644
- Tripp, T. M., Sembach, K. R., Bowen, D. V., et al. 2008, *ApJS*, , 177, 39, doi: 10.1086/587486
- Tripp, T. M., Meiring, J. D., Prochaska, J. X., et al. 2011, *Science*, 334, 952, doi: 10.1126/science.1209850
- Tully, R. B. 1987, *ApJ*, , 321, 280, doi: 10.1086/165629
- Tumlinson, J., Peebles, M. S., & Werk, J. K. 2017, *ARA&A*, , 55, 389, doi: 10.1146/annurev-astro-091916-055240

- Tumlinson, J., Thom, C., Werk, J. K., et al. 2011, *Science*, 334, 948, doi: 10.1126/science.1209840
- . 2013, *ApJ*, , 777, 59, doi: 10.1088/0004-637X/777/1/59
- van de Voort, F., Quataert, E., Hopkins, P. F., et al. 2016, *MNRAS*, , 463, 4533, doi: 10.1093/mnras/stw2322
- Veilleux, S., Cecil, G., & Bland-Hawthorn, J. 2005, *ARA&A*, , 43, 769, doi: 10.1146/annurev.astro.43.072103.150610
- Verdes-Montenegro, L., Yun, M. S., Williams, B. A., et al. 2001, *A&A*, , 377, 812, doi: 10.1051/0004-6361:20011127
- Vikram, V., Lidz, A., & Jain, B. 2017, *MNRAS*, , 467, 2315, doi: 10.1093/mnras/stw3311
- Vogt, F. P. A., Dopita, M. A., Borthakur, S., et al. 2015, *MNRAS*, , 450, 2593, doi: 10.1093/mnras/stv749
- Voit, G. M. 2019, *ApJ*, , 880, 139, doi: 10.3847/1538-4357/ab2bfd
- Watkins, A. E., Mihos, J. C., Harding, P., & Feldmeier, J. J. 2014, *ApJ*, , 791, 38, doi: 10.1088/0004-637X/791/1/38
- Wen, Z. Z., & Zheng, X. Z. 2016, *ApJ*, , 832, 90, doi: 10.3847/0004-637X/832/1/90
- Werk, J. K., Prochaska, J. X., Thom, C., et al. 2012, *ApJS*, , 198, 3, doi: 10.1088/0067-0049/198/1/3
- Werk, J. K., Prochaska, J. X., Tumlinson, J., et al. 2014, *ApJ*, , 792, 8, doi: 10.1088/0004-637X/792/1/8
- Werk, J. K., Prochaska, J. X., Cantalupo, S., et al. 2016, *ApJ*, , 833, 54, doi: 10.3847/1538-4357/833/1/54
- Wetzel, A. R., Tinker, J. L., & Conroy, C. 2012, *MNRAS*, , 424, 232, doi: 10.1111/j.1365-2966.2012.21188.x
- Wetzel, A. R., Tinker, J. L., Conroy, C., & van den Bosch, F. C. 2013, *MNRAS*, , 432, 336, doi: 10.1093/mnras/stt469
- White, P. M., Bothun, G., Guerrero, M. A., West, M. J., & Barkhouse, W. A. 2003, *ApJ*, , 585, 739, doi: 10.1086/346075
- White, S. D. M., & Frenk, C. S. 1991, *ApJ*, , 379, 52, doi: 10.1086/170483
- White, S. D. M., & Rees, M. J. 1978, *MNRAS*, , 183, 341, doi: 10.1093/mnras/183.3.341

- Williams, B. F., Ciardullo, R., Durrell, P. R., et al. 2007, *ApJ*, , 656, 756, doi: 10.1086/510149
- Willman, B., Governato, F., Wadsley, J., & Quinn, T. 2004, *MNRAS*, , 355, 159, doi: 10.1111/j.1365-2966.2004.08312.x
- Windhorst, R. A., Cohen, S. H., Hathi, N. P., et al. 2011, *ApJS*, , 193, 27, doi: 10.1088/0067-0049/193/2/27
- Windhorst, R. A., Timmes, F. X., Wyithe, J. S. B., et al. 2018, *ApJS*, , 234, 41, doi: 10.3847/1538-4365/aaa760
- Windhorst, R. A., Carleton, T., O'Brien, R., et al. 2022a, *AJ*, , 164, 141, doi: 10.3847/1538-3881/ac82af
- Windhorst, R. A., Cohen, S. H., Jansen, R. A., et al. 2022b, arXiv e-prints, arXiv:2209.04119. <https://arxiv.org/abs/2209.04119>
- . 2023, *AJ*, , 165, 13, doi: 10.3847/1538-3881/aca163
- Yang, X., Mo, H. J., van den Bosch, F. C., et al. 2007, *ApJ*, , 671, 153, doi: 10.1086/522027
- Yoon, J. H., & Putman, M. E. 2013, *ApJL*, , 772, L29, doi: 10.1088/2041-8205/772/2/L29
- Zabludoff, A. I., & Mulchaey, J. S. 1998, *ApJL*, , 498, L5, doi: 10.1086/311312

APPENDIX A
EXTRA COS-IGRM FIGURES

A.1 Group Environments

The remaining group environments are shown below in Figure 35. These environments were constructed from the New York University Value-Added Galaxy Catalog (NYU-VAGC; Blanton et al. (2005)) based on SDSS Data Release 2. These environments were used to distinguish between QSO sightlines that pass through only the IGrM from those passing through the CGM and the IGrM.

A.2 QSO Spectra with Voigt Profile Fits

The full sample of QSO spectra with Voigt Profile fits are presented below in Figures 36 - 47.

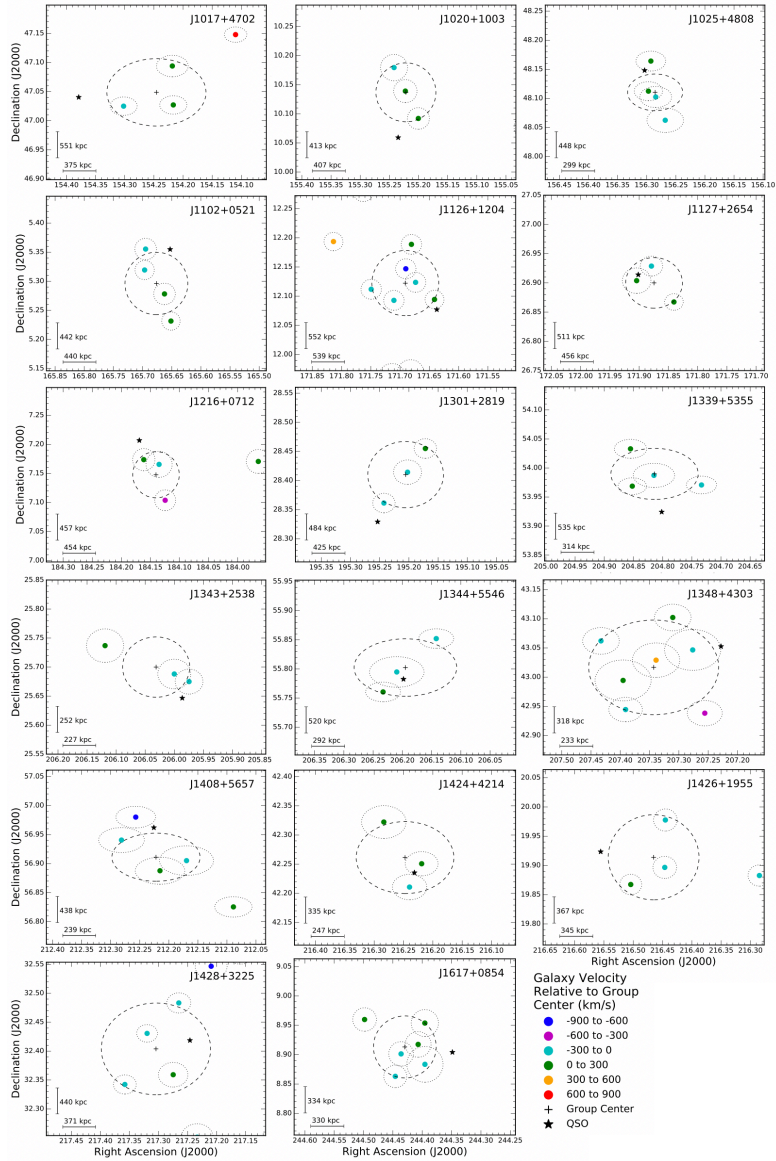


Figure 35. Environment plots for the remaining groups in the COS-IGrM sample that showed absorption lines within $\pm 800 \text{ km s}^{-1}$ of the group center. The color of the points represent the velocity of the member galaxies relative to the center of the group. The thick, dashed line represents the virial radius of the group, the thin, dotted lines represent the virial radii of the group members, the QSO sightline is represented by the star, and the group center is marked by the plus sign.

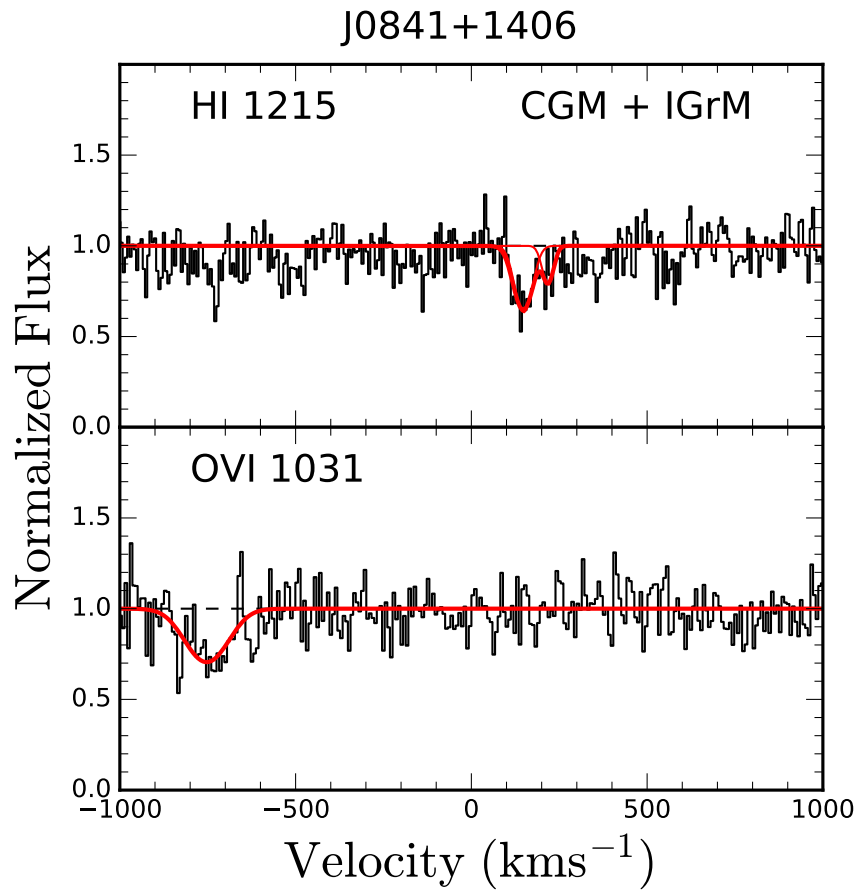


Figure 36. The observed spectra of sightline J0841+1406 showing H I and O VI detections. The Voigt profile fits are shown in red.

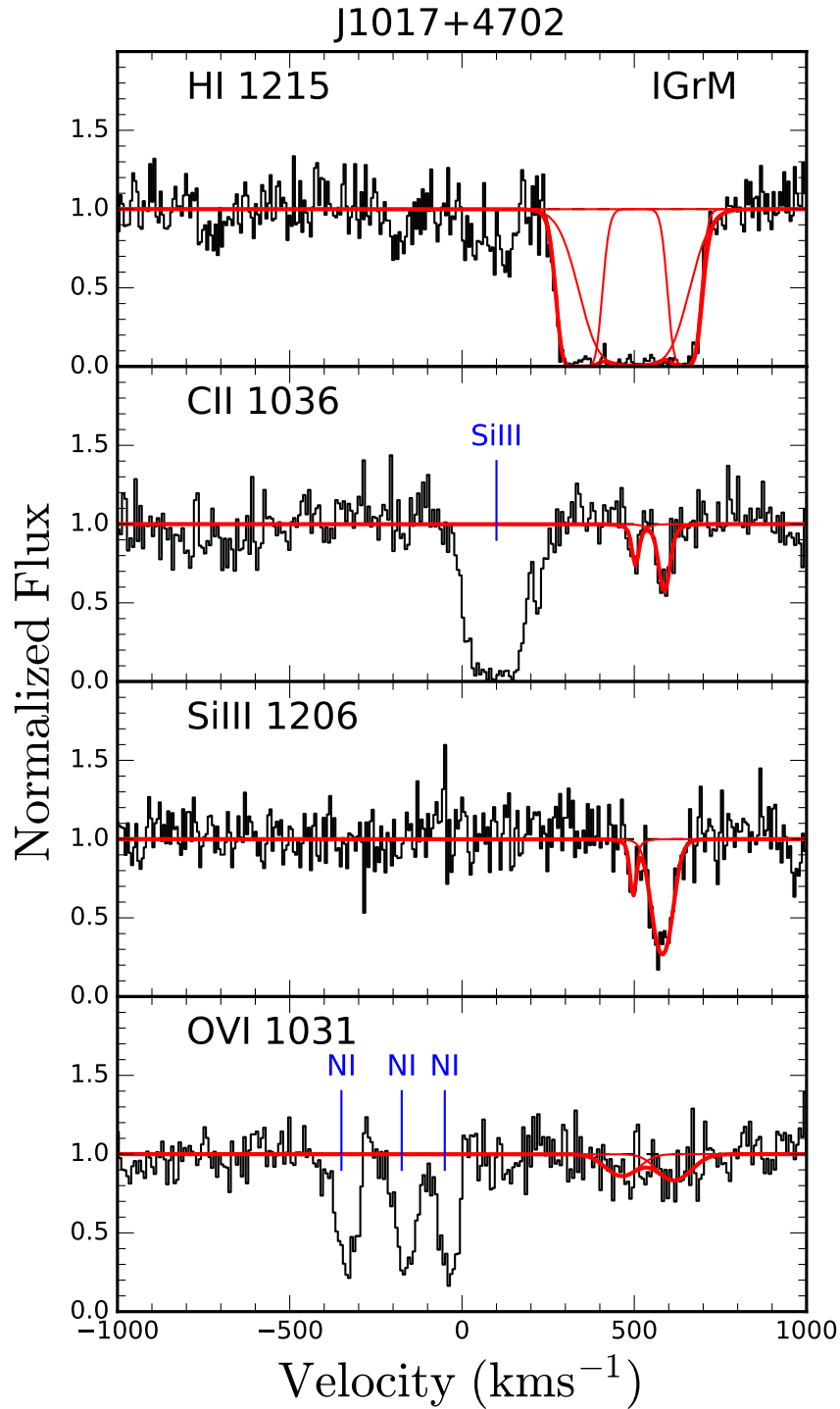


Figure 37. The observed spectra of sightline J1017+4702 showing H I, C II, Si III, and O VI detections. The Voigt profile fits are shown in red and intervening Milky Way absorption lines are marked in blue.

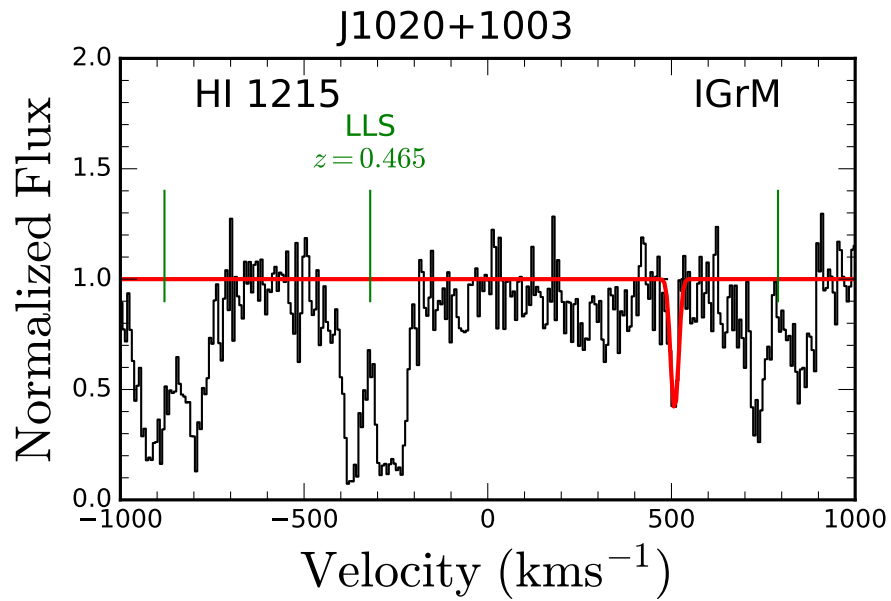


Figure 38. The observed spectra of sightline J1020+1003 showing HI absorption. The Voigt profile fit is shown in red and an intervening partial Lyman limit system line is labeled in green.

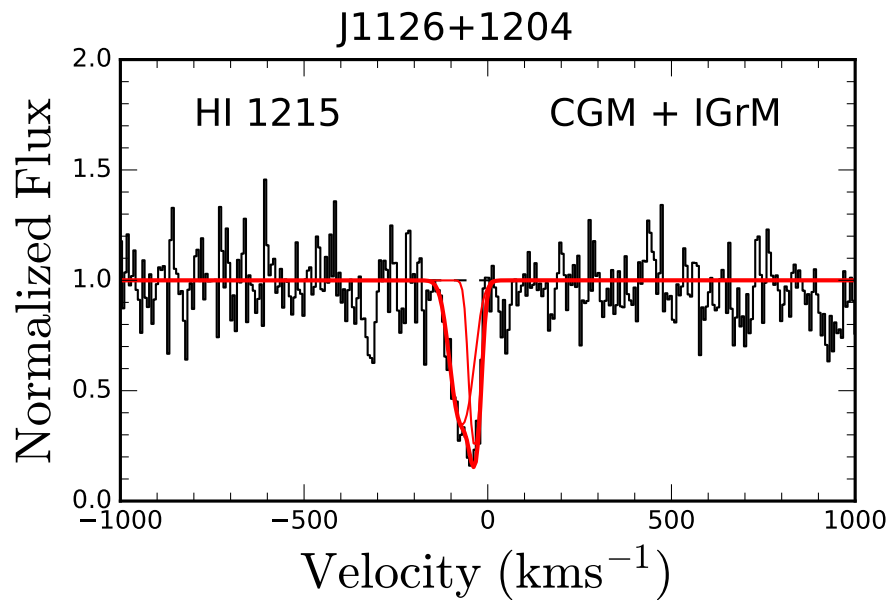


Figure 39. The observed spectra of sightline J1126+1204 showing HI absorption. The Voigt profile fits for each component are shown in red.

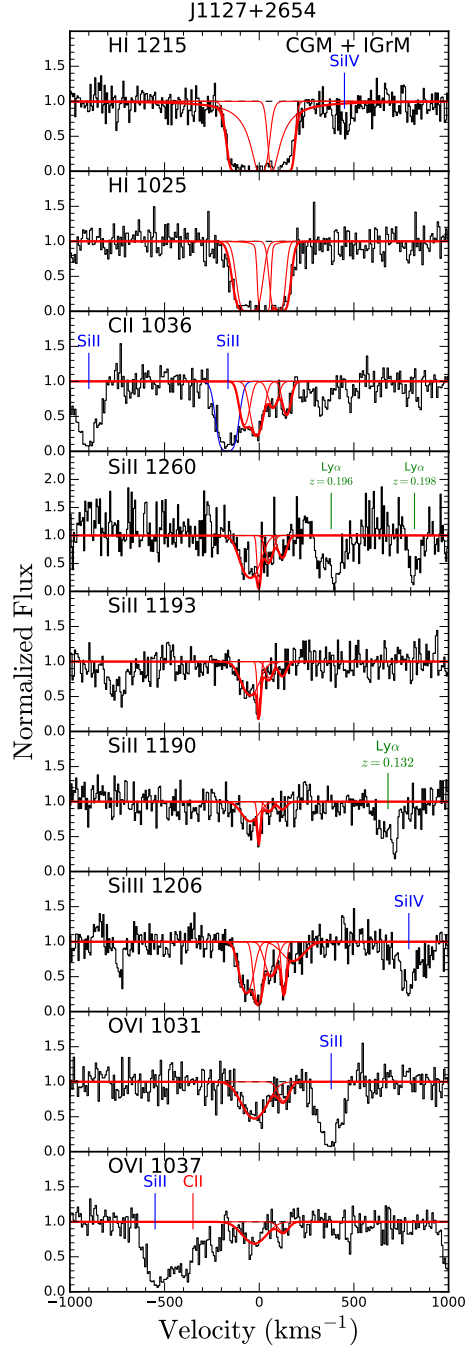


Figure 40. The observed spectra of sightline J1127+2654 showing H I, C II, Si II, Si III, and O VI absorption. The Voigt profile fits for each component are shown in red, Milky Way lines are labeled in blue, and intervening Ly α lines are labeled in green. The C II absorption feature was blended with Milky Way Si II λ 1193. The Milky Way Si II lines were modeled and the λ 1193 was removed from the spectra, which allows us to model the C II absorption. We place a lower limit on the C II absorption since some flux might be lost during the removal of the Milky Way Si II λ 1193 absorption feature.

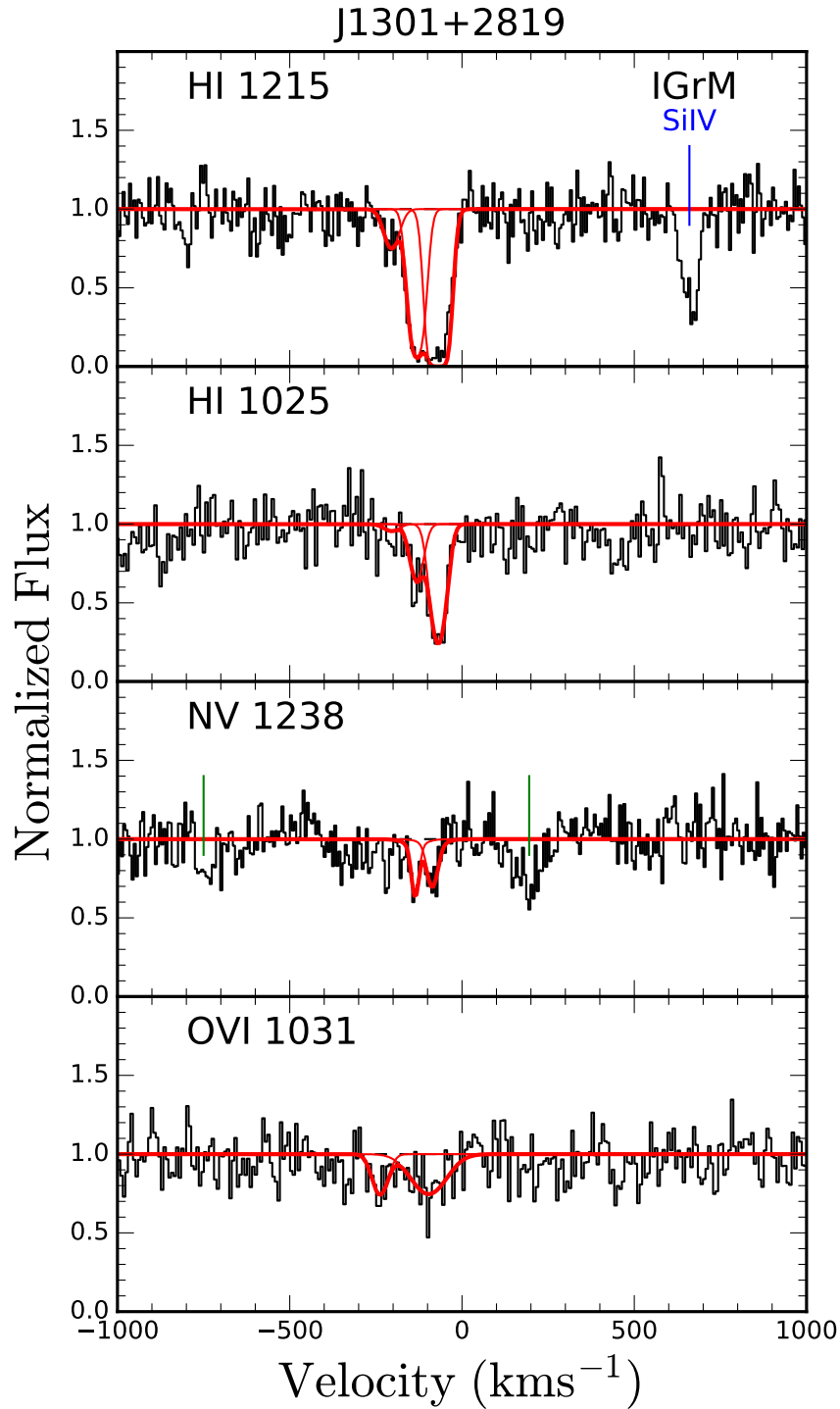


Figure 42. The observed spectra of sightline J1301+2819 showing H I, N v, and O VI absorption. The Voigt profile fits for each component are shown in red and Milky Way absorption is marked in blue. Two intervening lines could not be identified due to a lack of wavelength coverage and are shown in green.

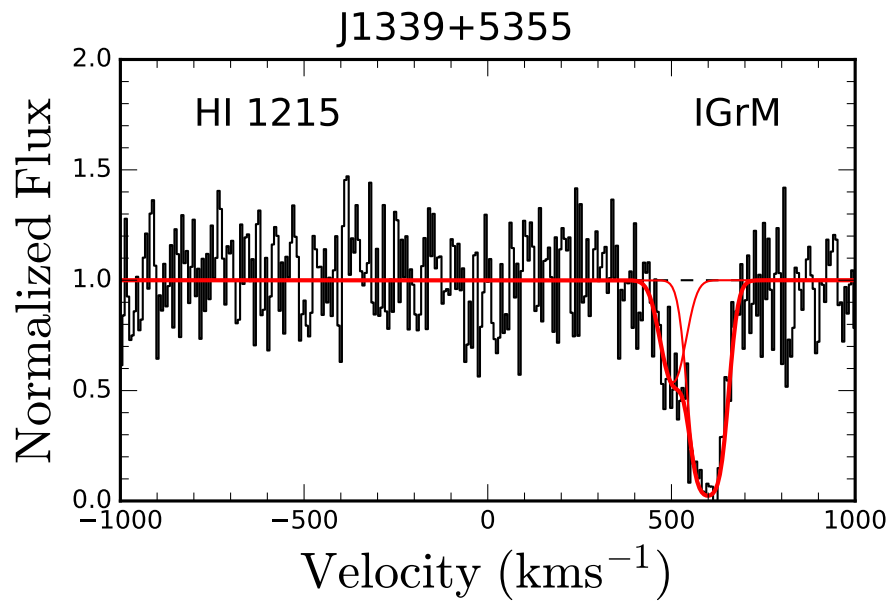


Figure 43. The observed spectra of sightline J1339+5355 showing HI absorption. The Voigt profile fits for each component are shown in red.

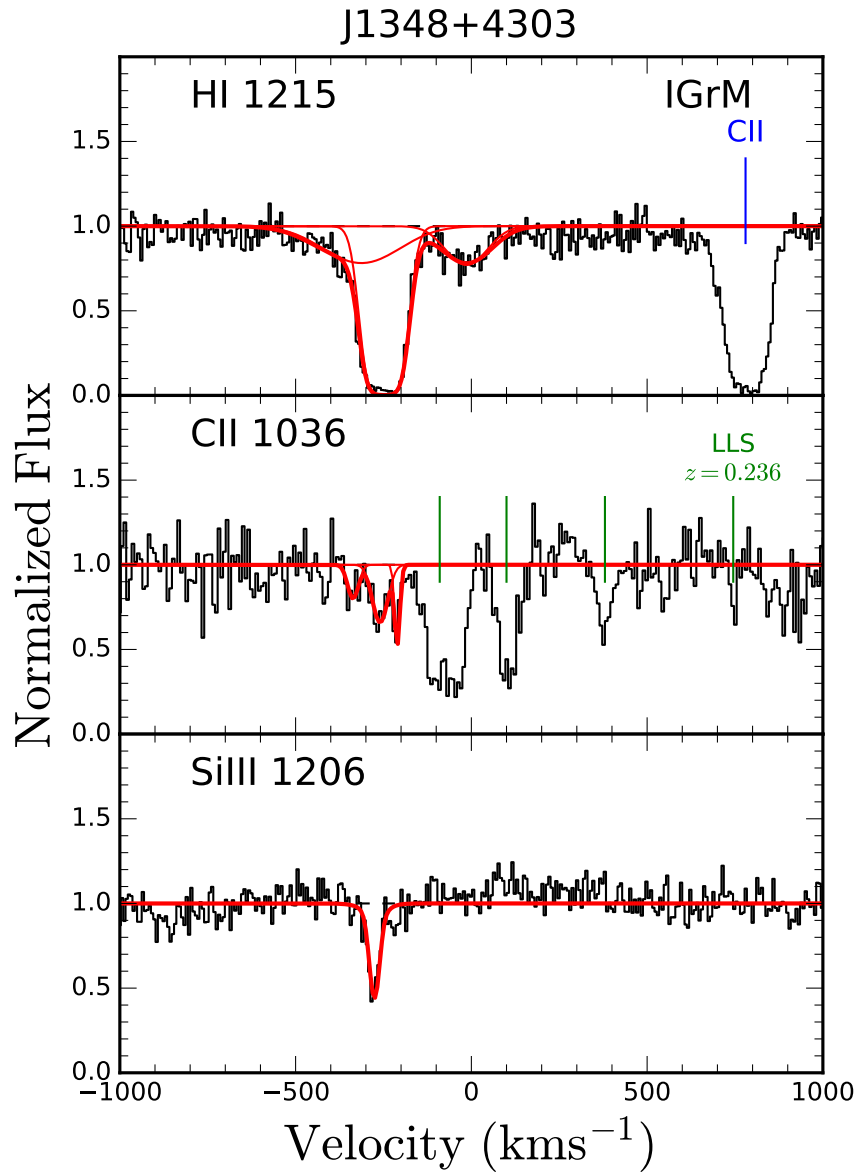


Figure 45. The observed spectra of sightline J1348+4303 showing H I, C II, and Si III absorption. The Voigt profile fits for each component are shown in red, Milky Way lines are labeled in blue, and intervening absorption lines are marked in green (and labeled if their identity is known).

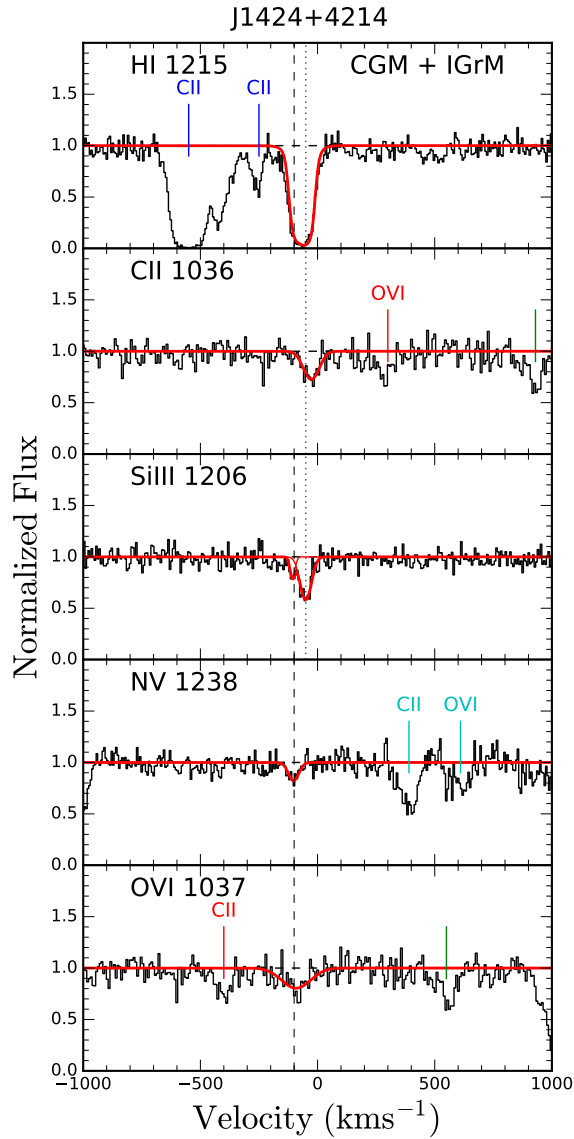


Figure 46. The observed spectra of sightline J1424+4214 showing H I, C II, N V, Si III, and O VI absorption. The Voigt profile fits for each component are shown in red, Milky Way lines are labeled in blue, intervening absorption lines are marked in green, and QSO absorption lines are labeled in cyan. There is no O VI 1031 detection as it is contaminated by an intervening absorber. Two components were fit to the Ly α profile; however, this dramatically increased the uncertainty in each of the two components. Therefore, to avoid over-fitting, we used a single Voigt profile.

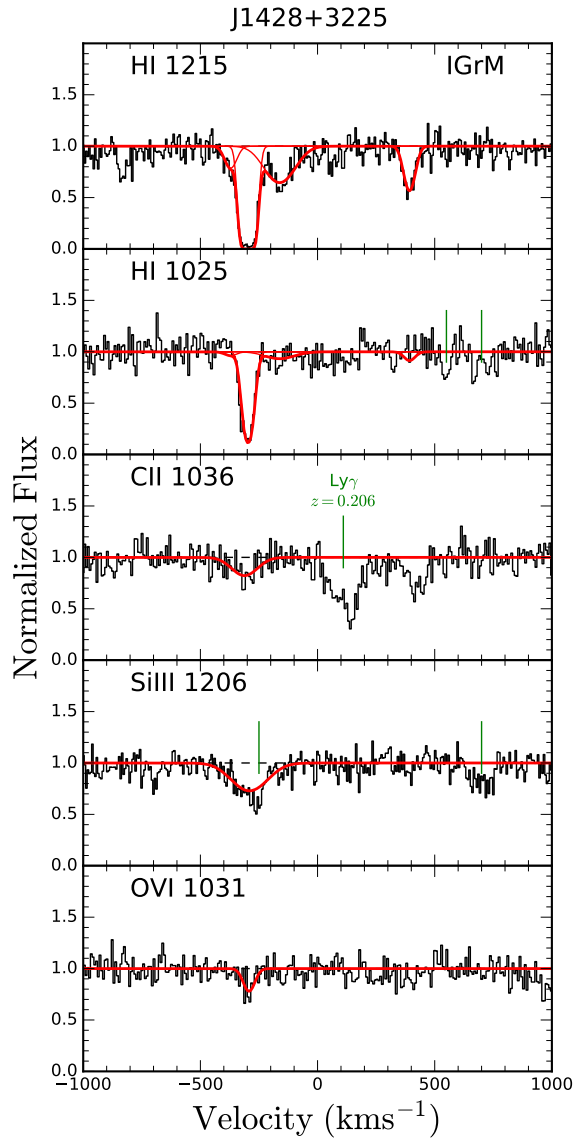


Figure 47. The observed spectra of sightline J1428+3225 showing H I, C II, Si III, and O VI absorption. The Voigt profile fits for each component are shown in red and intervening absorption lines are marked in green. The intervening component of the Si III profile is marked in green. Since there are not any other lines associated with this absorption feature, we marked it as intervening.